Evolution, Disruption, and Composition of Galactic Outflows Around Starburst Galaxies

by

J'Neil Irene Cottle Blough-Swingen

A Dissertation Presented in Partial Fulfillment
of the Requirements for the Degree
Doctor of Philosophy

Approved April 2021 by the
Graduate Supervisory Committee:

Evan Scannapieco, Chair
Chris Groppi
Patrick Young
Sanchayeeta Borthakur
Phillip Mauskopf

ARIZONA STATE UNIVERSITY

May 2021

ABSTRACT

The interaction between galaxies and the surrounding gas plays a key role in galaxy formation and evolution. Feedback processes driven by star formation and active galactic nuclei facilitate the exchange of mass and energy between the galaxy and the circumgalactic medium through inflowing and outflowing gas. These outflows have a significant impact on the star formation rate and metallicity of the galaxy. Observations of outflows have provided evidence that these outflows are multi-phase in nature, identifying both low energy ions such as Mg II and C III and high energy ions such as O VI. The underlying physics maintaining the two phases as well as the ionization mechanism for these phases remains unclear. In order to better understand galactic outflows, hydrodynamic simulations are used to study the evolution of wind-cloud interactions. In this work, I carried out a suite of magnetohydrodynamic (MHD) simulations to characterize the influence of magnetic fields on the evolution and lifetime of cold clouds. I found magnetic fields either provided little improvement to cloud stability over other influences such as radiative cooling or accelerated cloud disruption by pushing cloud material in the direction orthogonal to the wind and magnetic fields. To investigate the ionization mechanism of the material within outflows I first considered estimating the column densities of various ions within wind-cold simulations with the post-processing tool Trident. Under the assumption of ionization equilibrium, the simulations did not reproduce the observed absorption profiles demonstrating the need for a more detailed treatment of the ionization processes. I then performed a new set of simulations with the non-equilibrium chemistry solver, MAIHEM. The column densities produced in the non-equilibrium model alter the evolution of the cloud and highlight the increased ionization along the boundary of the cloud.

DEDICATION

To my husband, Alex,

and to my parents, Craig and Kristin.

—

In loving memory of my father-in-law, Lynn.

ACKNOWLEDGMENTS

This dissertation would not have been possible without the guidance, support, and encouragement from so many people over the past five years. Many thanks to my advisor Dr. Evan Scannapieco, whose upbeat and positive approach to mentorship set the tone for my entire graduate career. Thank you for treating me as a capable student and researcher from day one, ensuring that I was in charge of the direction of my work. Along those lines, thank you for your patience and support as I searched for projects most applicable to my future goals. I have always felt that my goals and best interests have been considered, prioritized, and honored. Additional thanks to my committee, Dr. Chris Groppi, Dr. Patrick Young, Dr. Phil Mauskopf, and Dr. Sanchayeeta Borthakur, your support has enabled me to expand my knowledge and become a well-rounded scientist through both projects and outreach. I would also like to thank my collaborators at the Hamburg Observatory, Dr. Marcus Brüggen and Dr. Wladimir Banda-Barragán, for their thoughtful feedback and insight into running MHD simulations.

I am thankful for all of the wonderful connections I have made while at ASU. To my office mates, Ed Buie and Nivedita Mahesh, I could not have picked a better pair of people to work alongside. Ed, thank you for our chats about so many things; from research to traveling and anything in between. To Nive, thank you for enriching my life and getting me involved in so many opportunities to build and give back to my community. Much thanks to Lucia Perez for always being a great source of both encouragement and commiseration. To all of my fellow graduate students, thank you for building a community full of support.

To my friends outside of ASU, thank you for always reminding me of the bigger picture and implicitly understanding that it will get done when it's done. Danielle, thank you for being my most enthusiastic cheerleader.

Most importantly, I would like to give sincere thanks to my family. To my parents, thank you for indulging my early interest in astronomy and continually supporting my goals as I looked towards the stars. Mom, thank you for your interest and patience every week as I tried to explain my work over lunch. Dad, thank you for being so clearly proud of me, every step of the way. To my sister Grace, thank you for making computer science look fun and like something I should try - I would not have gotten far without it! To my husband, Alex, thank you for your constant support and encouragement. I could not have completed this degree without the supportive space you create for me. Thank you for valuing my goals as much as your own and always knowing when I need a good laugh.

TABLE OF CONTENTS

CHAPTER Page

CHAPTER Page

LIST OF TABLES

LIST OF FIGURES

Figure Page

Chapter 1

INTRODUCTION

When astronomers Harlow Shapley and Heber Curtis were first debating the existence of galaxies in 1920, galaxies outside our own were colloquially called 'island universes' invoking images of distant collections of stars isolated from any other influences, free to evolve on their own. The idea of isolated galaxies has long since been discarded as it's been found that the evolution of galaxies is largely impacted by the cycle of gas flowing into and out of the galaxy (Veilleux *et al.*, 2005). The outflowing gas, called galactic winds, is largely responsible for transporting metals out of the galaxy to the surrounding gas, the circumgalactic and intergalactic mediums. This enrichment of gas impacts the evolution of the galaxy as gas is recycled through accretion and star-formation (Somerville and Primack, 1999).

There is still much to learn about the feedback processes by which galaxies interact with their surroundings. Outflowing winds are difficult to observe due to their high temperatures and diffuse nature, resulting in clear observations of only nearby galaxies. This limits our ability to understand the chemical makeup of the gas enriching the circumgalactic medium. Observations of more distant galactic winds are restricted to the absorption of light by entrained material within the winds. This cooler, more dense material makes up clouds that are transported out of the galaxy. These clouds can be seeds for star-formation (Werk *et al.*, 2013), therefore it is of great interest to understand how this is material disrupted by the winds and the extent to which it is accelerated away from the galactic disk.

The limitations on the ability to directly observe galactic winds have demonstrated the need to consider these interactions theoretically. Hydrodynamic simulations pro-

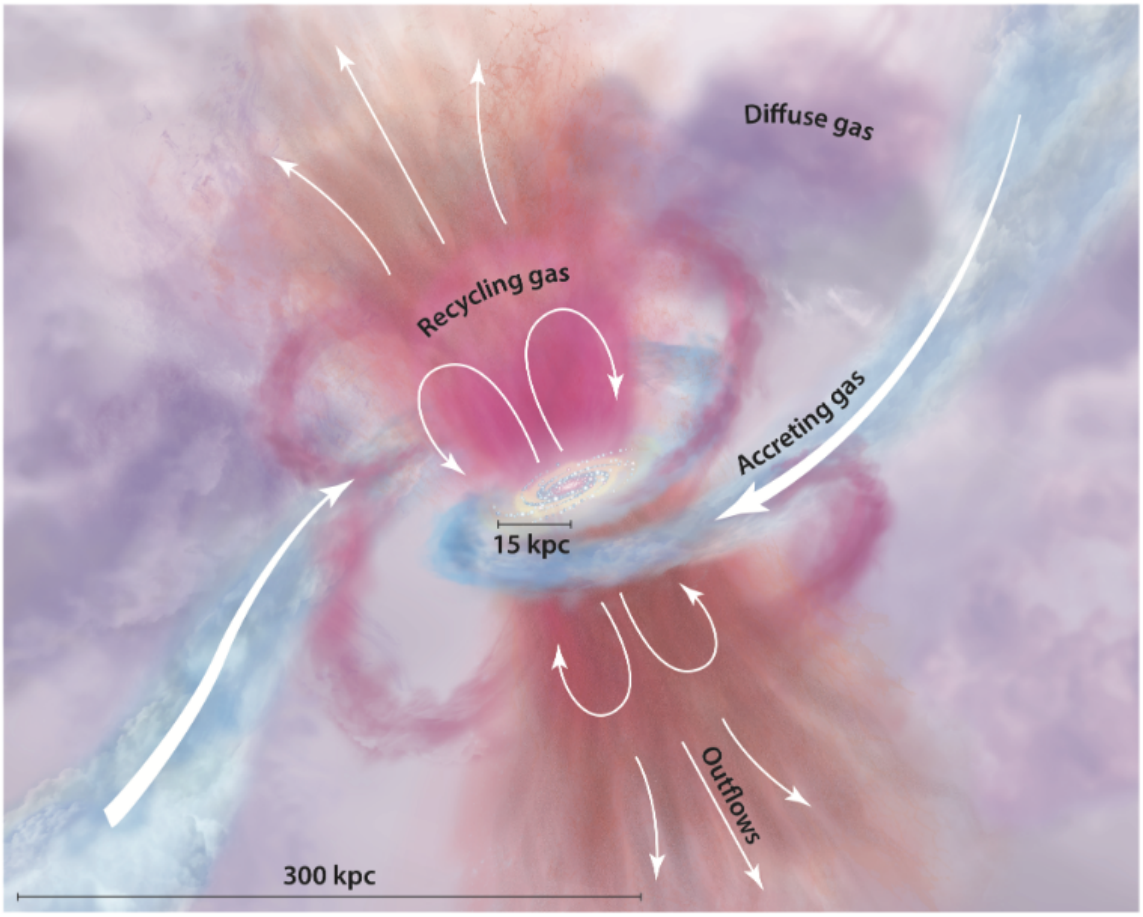

Figure 1.1: An illustration of the feedback processes within and outside of a galaxy. Accretion from the IGM is shown in blue, outflowing and recycling gas in orange and pink, and diffuse halo gas in purple. Image credit: Tumlinson *et al.* (2017)

vide an ideal sandbox for investigating the influence of specific physical processes on both the disruption and evolution of clouds embedded in winds. This work strives to build on the understanding of galactic outflows with such simulations as well as apply ionization models to connect simulations to observations

1.1 Galactic Outflows and the Circumgalactic Medium

1.1.1 Observations of Winds and the CGM

In 1963, Lynds and Sandage (1963) presented observations of an explosion emanating from the center of M82. From observations of the outflowing gas, they determined that the explosion occurred roughly 1.5 million years ago, requiring 2.4×10^{55} ergs of energy to push 5.6×10^6 M_{sun} of mass outflowing from the disk. The explosion of gas is mostly confined along the minor axis of the galaxy with clear filaments outlining magnetic field lines pulled from the disk by the expanding gas. Even so early on, these observations demonstrated the strong influence outflows have on the circumgalactic medium.

Now, over 50 years later, M82 has been studied extensively in all wavelengths. Being one of the closest starbursting galaxies makes it a great subject for studies of both extended emission in X-ray and spectroscopic observations. Optical spectroscopic data of M82 supports the superwind model; where high-velocity gas pushed by star formation and stellar winds shock heat and accelerate the circumgalactic medium (Heckman *et al.*, 1990). X-ray emission observations have provided insight into the distribution of hot plasma created by supernova explosions (Griffiths *et al.*, 2000) while absorption studies of M82 have demonstrated likely mixing between the wind and the surrounding gas as well as non-thermal emission (Lopez *et al.*, 2020).

Closer to home, X-ray observations of the Milky Way galaxy have provided insight into how our own galaxy interacts with its environment. In-depth studies of Sagittarius A* have given evidence for a bipolar outflow originating from the location of Sgr A*. Models of the mass accretion of Sgr A* have indicated that the accretion rate must be small to be consistent with the observations of polarized emission. The accretion rate may be lowered by the outflow of gas from the galactic center (Agol,

Figure 1.2: Top: Figure 9 from Lynds and Sandage (1963) showing the composite image of M82 highlighting the hot outflowing gas. Bottom: A composite image of M82 from 2017 constructed by combining infrared and visible light images. Image credit: NASA, ESA and the Hubble Heritage Team (STScI/AURA); Acknowledgment: J. Gallagher (University of Wisconsin), M. Mountain (STScI) and P. Puxley (National Science Foundation)

2000). This is further supported by observations of Sgr A* showing bipolar lobes of bright emission (Baganoff *et al.*, 2003).

In infrared wavelengths, Bland-Hawthorn and Cohen (2003) mapped the distribution of the hot plasma within the galactic plane. They also noted a bipolar structure centered at the Galactic Center likely tracing a wind powered by the central starburst. This infrared emission is consistent with X-ray emission originating from the same location. Since faint emission would be difficult to detect for extra-galactic sources, the authors note that the multi-wavelength detection of this wind in our own galaxy is compelling evidence that the phenomenon of large-scale winds may be far more common than had been previously observed.

Indeed, outflows can be detected within a majority of starburst galaxies, with detection most strongly dependent on the orientation of the galaxy (Rubin *et al.*, 2014). However, the distance and orientation of these galaxies hinder our ability to study their interactions as extensively as our own galaxy.

X-ray emission observations, like those of our own galaxy mentioned above, trace the hot outflowing gas that makes up the galactic winds. However, for distant galaxies, this emission is too faint to observe with certainty. Fortunately, several observations have demonstrated that two or more phases can be found coexisting within the outflowing gas (e.g. Bolatto *et al.*, 2013; Arav *et al.*, 2013; Barger *et al.*, 2016), providing signatures of outflows in a different, much more easily observed, range of wavelengths. The multiphase nature of galactic winds is crucial for our ability to study galaxies further away. In fact, most observations of outflowing material are made of the absorption of background light by cool entrained gas within the winds.

The types of gas within the circumgalactic medium can be determined by studying spectra with absorption line profiles created by cool gas along the line of sight of a bright background source. The COS-Halos survey with the Cosmic Origin Spec-

trograph (COS) aims to understand the physical conditions of the circumgalactic medium by studying these spectra. Early studies with the survey (Werk *et al.*, 2013) determined that the amount of metals, any atom heavier than helium, declines with distance from the galaxy. These metals are found within the cool gas in the CGM, and highlight a wide range of gas densities. These studies have also emphasized the impact outflows have on their environment by enriching the circumgalactic medium. Borthakur *et al.* (2013) find that C IV is preferentially detected within the halos around starbursting galaxies. The detection of this highly ionized material is likely due to the effects of outflows driven by starbursts, extending to as far out as 200 kpc from the galactic disk.

These types of absorption line studies can be found in two orientations. Most commonly, the background source is a quasar (QSO). These spectra present transverse measurements of the circumgalactic medium and can be used to study the ionization with respect to the distance from the host galaxy. The second orientation, known as down the barrel, makes use of the host galaxy as the background source, looking along the direction of the outflow. A combination of these two orientations can be used together to model the outflow properties. Kacprzak *et al.* (2014) make use of a unique set of observations where the CGM of a single galaxy is observable from both orientations. They find the outflowing velocities of each orientation are consistent with each other; with a range for down the barrel velocities of 45-255 km/s and a range of outflowing transverse velocities of 40-80 km/s. Together these measurements suggest that the two observations originate from the same outflowing material. Surveys of absorbers from both directions can also give insight into the general properties of outflows as shown in Ng *et al.* (2019). In that work, the authors find that after normalizing out an observed mass dependence, the kinematics of edge-on, or transverse, absorbers suggest bipolar outflowing gas while face-on, or down the barrel, absorbers

suggest decelerating outflowing gas. These two conclusions are consistent with the picture of accelerated gas expanding outward from the galactic disk.

1.1.2 What Drives Galactic Winds?

As evidence of these hot winds has grown, it has been a natural question to determine what is driving them. One likely candidate is Active Galactic Nuclei (AGN). Hopkins *et al.* (2014) outline two types of AGN; radiative mode and jet mode. Radiative mode AGN are associated with dense cold gas clouds in the circum-nuclear region, and high levels of star formation triggered by the injection of energy by the AGN. Jet mode AGN are much more focused into collimated outflows of energy and found mostly in massive bulges and elliptical galaxies. Both of these modes can cause feedback in the form of outflowing material.

The need for AGN feedback has been further investigated through the use of cosmological simulations. Schaye *et al.* (2015) performed cosmological simulations known as the EAGLE simulations which follow the evolution of galaxies and their environments. In particular, these simulations were able to account for the feedback due to AGN which caused winds to develop "naturally" as the galaxies evolved. In another set of simulations, Kaviraj *et al.* (2017) noted that AGN feedback is necessary to reproduce observed stellar mass functions and star formation histories, demonstrating the impact of AGN on galactic evolution.

Galactic winds may also be driven by supernovae. Early observations of dwarf galaxies found a connection between metal-poor galaxies and supernova-driven winds (Dekel and Silk, 1986). Other observations of starbursting galaxies (i.e. Heckman, 2004; Veilleux *et al.*, 2005), note that stellar winds and supernovae account for the necessary mass and energy to produce observed winds and often entrain interstellar material, carrying it outwards.

This driving mechanism is also supported with simulations such as in Scannapieco and Broadhurst (2001a) and Mori *et al.* (2002), which show that outflows strip material from low mass galaxies which can then be carried by supernova driven winds, effectively enriching the intergalactic material. Furthering this idea, Murray *et al.* (2011) finds that when radiation pressure is accounted for, the gas entrained by the winds can be accelerated even further beyond the galactic disk.

AGN and supernova are both compelling mechanisms for accelerating hot material beyond the center of a galaxy. In general, it is likely that most multiphase winds are a combination of the two, supporting the necessary energy requirements and the need for coexisting phases to be accelerated together.

1.1.3 Effects of Outflows

The acceleration and transportation of mass by galactic outflows can have a lasting impact on galaxy evolution. The COS-Halos survey has identified higher velocity offsets in the CGM of starburst galaxies than control galaxies (Heckman *et al.*, 2017a). These starburst galaxies are more often found to have supernova-driven winds, demonstrating the effect of outflows extends beyond the disk of the galaxy.

As this mass is transported out of the galaxy, it is carrying metals that enrich the surrounding medium. In fact, Simcoe *et al.* (2004) investigated the metallicity of the IGM with time, finding high amounts of metals around galaxies prior to $z \sim 2.4$. These metals were likely recycled by outflows transporting enriched gas from the galaxy's disk to the IGM. This mass loss is even greater within low mass galaxies. Larson (1974) demonstrated low mass galaxies have high amounts of mass loss as supernova-driven winds can more easily carry mass away from the disk. The transportation of metals is furthered as winds push the interstellar medium out of the galaxy (Heckman *et al.*, 1993; Strickland and Heckman, 2007). The presence of metals enables gas clouds

to cool and condense into the seeds for star formation. With lower amounts of metals, star formation is harder to achieve. Together these two effects can effectively remove metals from the disk of the host galaxy, quenching star formation (Tremonti *et al.*, 2004; Genel *et al.*, 2014).

1.2 Simulating Outflows

As evidence of the multiphase nature and ionization structure of the outflowing gas has grown, questions about the dominant physics have remained. How effectively does the wind accelerate the cloud? Is the cloud quickly destroyed by hydrodynamic instabilities? What is the dominant ionization mechanism? What is the dominant physics aiding the existence of multiple phases? These questions are better answered analytically and with numerical simulations, inspiring a collection of wind-cloud studies investigating the evolution and destruction of shocked clouds within outflows.

1.2.1 Early Theoretical Models

The starting point for modeling outflowing gas is the analytical solution for a wind from a starburst galaxy by Chevalier and Clegg (1985). In this solution, they demonstrated that if supernova energy is converted to thermal energy, a strong wind is driven out of the galaxy's nucleus. They then derive an analytic solution for the variation of thermal pressure and ram pressure with radius. This model is consistent with X-ray emission from M82 if the emission is interpreted as originating from shocked clouds as the wind sweeps outward.

As Chevalier and Clegg defined the base analytical solution for outflowing gas, the simulations in Klein *et al.* (1994) have been treated as the base for numerical solutions of the wind-cloud interaction. In that work, the authors consider the wind-cloud interaction in the context of interstellar clouds heated and destroyed by a

propagating shock. In order to characterize the interaction in a general timescale applicable to all wind and cloud parameters, they defined a characteristic timescale for the interaction called the cloud crushing time. This time describes the time it takes for the shock to propagate through the radius of the cloud as is defined as

$$t_{\rm cc} = \frac{\chi^{1/2} r_c}{v_{\rm amb}}, \tag{1.1}$$

where χ is the ratio of cloud density to wind density, r_c is the radius of the cloud, and $v_{\rm amb}$ is the velocity of the wind. Considering a range of density ratios, wind velocities, and resolutions these two-dimensional simulations highlighted the destruction and fragmentation of clouds by hydrodynamic instabilities. The Kelvin-Helmholtz instabilities, driven by the shear at the boundary of two gas layers moving in opposite directions, strip away the cloud material from the sides. The Rayleigh-Taylor instabilities, driven by gas of two different densities accelerating towards each other, cause the fragmentation of the cloud from the front (Chandrasekhar, 1961). Ultimately, these simulations demonstrated the inability of a cloud to exist within in a wind long enough to reproduce the distinct phases observed around starbursting galaxies. The stability, and therefore lifetime, of clouds, must be aided by other physical influences such as radiative cooling or magnetic fields

1.2.2 Wind-Cloud Simulations

Shortly after the work of Klein *et al.* (1994), the influence of magnetic fields on wind-cloud interactions was first investigated numerically by Mac Low *et al.* (1994). These two-dimensional simulations demonstrated that the presence of uniform magnetic fields threaded through the cloud helped stabilize the cloud against Kelvin-Helmholtz instabilities. The increased stability and dampened fragmentation allow the cloud to survive longer than in the case without magnetic fields. It was also

found that the wind-cloud interaction amplifies the magnetic field in a flux rope in the tail of the cloud. An amplified magnetic field leads to an increase in X-ray and synchrotron emission.

Further investigation of wind-cloud interactions with magnetic fields was conducted by Fragile *et al.* (2005), with two-dimensional simulations that also included radiative cooling, which can enable the cloud to condense into smaller, more dense cores. In these simulations, the magnetic fields confined to the ambient wind material were found to suppress instabilities at the cloud boundary in agreement with Mac Low *et al.* (1994) and similar studies (Gregori *et al.*, 2000; Shin *et al.*, 2008). The effects of radiative cooling are compounded in magnetized wind cases as the fields aid compression of cloud fragments, enabling them to cool further. However, fields internal to the cloud inhibit this effect as magnetic field lines resist compression.

As the numerical treatment of magnetic fields requires high resolution and therefore is computationally expensive, it was not until recently that the investigation of magnetic fields extended to simulations in three dimensions. The expanded domain allows for the exploration of different magnetic field orientations and the three-dimensional structure of the cloud as it is torn apart. McCourt *et al.* (2015) consider clouds threaded by tangled magnetic fields, finding that the magnetic fields substantially increase cloud lifetimes and allow for more clumping of cloud material. The drag force created by the cloud sweeping upfield lines as the wind propagates past the cloud also leads to accelerations of clouds that are consistent with non-Keplerian orbits observed of clouds near the center of the Milky Way. The three-dimensional structure of the magnetic field is investigated in Banda-Barragán *et al.* (2016), considering the evolution of fields both aligned and perpendicular to the flow of the wind. In the case of aligned fields, the fields create flux ropes, similar to those described in Mac Low *et al.* (1994) along the tail of the cloud. These ropes are pressure confined

and create a thin filament of cloud gas that survives past the destruction of the original cloud. Perpendicular fields form current sheets which cause filamentation of the tail of the cloud.

The combination of radiative cooling and thermal conduction has been shown to extend cloud lifetimes over the hydrodynamic case by suppressing instabilities (Mellema *et al.*, 2002; Fragile *et al.*, 2004; Cooper *et al.*, 2009). For high wind Mach numbers, Orlando *et al.* (2005) find that radiative losses enable the cloud to fragment into cold, dense filaments while thermal conduction causes the cloud to evaporate in a few cloud crushing times. In Scannapieco and Brüggen (2015), the effect of radiative cooling was considered further for a range of wind Mach numbers from subsonic to supersonic. These simulations demonstrated that the filamentary tails created in supersonic flows are further condensed with radiative cooling, enabling the clouds to be accelerated from the driving region to a greater extent than their purely hydrodynamic counterparts. When including the effects of thermal conduction in Brüggen and Scannapieco (2016), the clouds are found to evaporate away, consistent with earlier work. However, thermal conduction also aids the compression of the clouds to create denser cloudlets than achieved with radiative cooling alone. Still, these small cores are unable to be accelerated to the point they would reach the outer edges of the driving region before being destroyed by hydrodynamical instabilities.

When considering wind-cloud interactions, it is unrealistic to expect turbulence to be negligible. In order to investigate how turbulence affects the evolution of clouds embedded in winds, there are have been several suites of simulations focused on understand these effects. Two-dimensional simulations in Pittard *et al.* (2009) demonstrated the ability of turbulence to destroy clouds quickly. While considering two separate turbulent models, Banda-Barragán *et al.* (2019) found that in general turbulence is supportive of the survival of very dense gas remaining within the wind, but

does not enable gas to be entrained in the wind. In work aiming to determine the most influential physical effect on the wind-cloud interaction, Li *et al.* (2020) compared the effects of magnetic fields and turbulence in addition to radiative cooling and thermal conduction. They conclude that radiative cooling and conduction have a greater impact than turbulence and magnetic fields, noting that the majority of clouds can be characterized by the effects of conduction or cooling. Either clouds have too low of densities and are evaporated quickly by conduction, or they live much longer than the cooling time, enabling the cloud to accrete swept up gas and grow.

1.2.3 Connecting to Observations

The connection between these simulations and the observational data of galactic outflows hinges on our ability to approximate the distribution of ionized gas and the ionization mechanism. For much of the CGM, the majority of the ionization is thought to come from the metagalactic UV background, the integrated UV flux from QSOs, and massive, hot stars. The spectrum of this background has been synthesized (Haardt and Madau, 1996, 2012) and used within radiative transfer codes (Ferland *et al.*, 2017) to approximate the ionization structure of cosmic gas in collisional and photoionization equilibrium. However, in the case of wind-cloud interactions, the assumption of equilibrium may not be accurate. As the wind passes by the cloud, it shocks the gas and the effects of heating need to be accounted for.

There are tools to estimate the distribution of observable ionization states as a post-processing step to hydrodynamic simulations, such as Trident (Hummels *et al.*, 2017). Trident determines the ionization fraction of simulated gas by accounting for the gas temperature, density, and redshift under the assumption it is in photoionization equilibrium with a background source. There have also been simulations that have modeled non-equilibrium chemistry within the simulation in order to capture

the ionization structure created by the evolving interaction. Kwak *et al.* (2011) have tracked high ionization energy ions in high-velocity clouds in order to describe the clouds observed orbiting the Milky Way. However, without including a photoionizing background, these simulations are difficult to apply to extra-galactic outflows. In large-scale simulations, Oppenheimer *et al.* (2018) tracked the ionization states of the CGM finding levels of low ionization energy ions consistent with COS-Halos observations. While this work is useful in understanding the CGM as a whole, it was restricted to large-scale interactions rather than a close look into the interaction between a single cloud and wind. Even with these attempts, the characterization of the ionization of the shocked and disrupted gas within galactic outflows remains difficult to achieve.

1.3 Structure of Thesis

Chapter 2 of this work presents the results of magnetohydrodynamic (MHD) wind-cloud simulations within the parameter space relevant to galactic outflows. As magnetic fields can have a significant impact on the stability of embedded clouds, these simulations characterize the global evolution of the cloud's mass loss and downwind velocity as well as consider the morphology of the evolved cloud due to the interactions between the wind and magnetic fields. The MHD simulations consider the interplay between the known stabilizing influence of radiative cooling and magnetic fields both aligned and transverse to the direction of the wind flow. In Chapter 3, I present results from an ionization equilibrium approach to estimating the column densities of commonly observed ions within simulations of galactic winds. The distribution of column densities produced within the simulations is connected to observed absorption profiles to characterize the likely ionization mechanisms for cold material in the circumgalactic medium. Chapter 4 presents a more detailed look at the ionization of

galactic winds with the use of hydrodynamic simulations including a non-equilibrium chemistry solver, MAIHEM. The new, non-equilibrium column density distributions are compared to equilibrium estimations and connected to observations. In Chapter 5, I summarize these results and how they further characterize the disruption and ionization of galactic winds.

Chapter 2

THE LAUNCHING OF COLD CLOUDS BY GALAXY OUTFLOWS III: THE INFLUENCE OF MAGNETIC FIELDS

This chapter is reproduced from the version published in 2020 in The Astrophysical Journal, Volume 892, Page 59, with permission from the co-authors.

2.1 Introduction

Understanding the evolution and disruption of wind-swept clouds is essential to understanding the circumgalactic medium (CGM), as winds driven by star formation and supernovae accelerate dense clouds past the limits of the galactic plane. These outflowing winds have long been considered theoretically (e.g. Chevalier and Clegg, 1985; Mac Low and Ferrara, 1999; Murray *et al.*, 2005; Scannapieco and Brüggen, 2010; Sur *et al.*, 2016; Scannapieco, 2017), and observations have provided evidence for both their multiphase nature (e.g. Veilleux *et al.*, 2005; Sturm *et al.*, 2011; Meiring *et al.*, 2013; Bolatto *et al.*, 2013; Kacprzak *et al.*, 2014; Rubin *et al.*, 2014) and their impact on galactic evolution and star formation (e.g. Tremonti *et al.*, 2004; Oppenheimer *et al.*, 2010; Davé *et al.*, 2011; Lu *et al.*, 2015; Agertz and Kravtsov, 2015). However, the details of the interaction between the winds and entrained clouds have been difficult to investigate without the use of numerical studies.

In the purely hydrodynamical regime, Klein *et al.* (1994) showed that such clouds are accelerated over time-scales $\approx 3-4$ times longer than the cloud-crushing time (hereafter, t_{cc}), which is defined as the time taken by an internal shock to travel across one cloud radius. However, further studies (e.g. Poludnenko *et al.*, 2002; Pittard *et al.*, 2009; Fragile *et al.*, 2005; Banda-Barragán *et al.*, 2019) indicated that shocks

and dynamical instabilities quickly destroy the clouds on timescales that are too short for the clouds to reach the speeds and distances at which they are observed in galactic outflows.

Studies focusing on the influence of other effects, such as radiative cooling (e.g. Schiano *et al.*, 1995; Cooper *et al.*, 2009; Schneider and Robertson, 2017; McCourt *et al.*, 2018; Gronke and Oh, 2018; Sparre *et al.*, 2019; Scannapieco and Brüggen, 2015, hereafter Paper I) and thermal conduction, have also been carried out (e.g. Orlando *et al.*, 2005; Brüggen and Scannapieco, 2016, hereafter Paper II). In the cooling case, cloud disruption is delayed by the suppression of shock heating, which is the dominant disruption mechanism in cases in which the exterior flow is supersonic. In the case of thermal conduction, cloud disruption is delayed by the presence of an evaporative layer, which compresses the cloud and protects it from shredding by the exterior flow. However, in both scenarios, the clouds eventually fragment into smaller cores (McCourt *et al.*, 2018; Sparre *et al.*, 2019) or condense into filaments, and the cloud cross-sections are too small to be accelerated by ram pressure to the extent observed.

The influence of magnetic fields on the wind-cloud interaction introduces a mechanism to balance the acceleration and destruction of the clouds. In early two-dimensional magnetohydrodynamical (MHD) studies (e.g. Mac Low *et al.*, 1994; Jones *et al.*, 1996; Miniati *et al.*, 1999) it was shown that uniform magnetic fields transverse to the flow are likely able to create a magnetic 'bumper' at the front of the cloud and potentially reduce the effect of the instabilities that destroy the cloud. On the other hand, in the case of fields aligned with the flow, the wind was found to have a similar disruptive effect on the cloud as in the hydrodynamic case.

Continued studies in, both, 2D (Orlando *et al.*, 2008; Pittard *et al.*, 2009, 2010) and 3D (Gregori *et al.*, 2000; Shin *et al.*, 2008; Pittard and Parkin, 2016; Grønnow

et al., 2017), have considered both aligned and transverse field orientations, as well as explored the impact of varying the wind Mach number (van Loo *et al.*, 2007), magnetic field strength (McCourt *et al.*, 2015) and turbulence (Banda-Barragán *et al.*, 2018; Li *et al.*, 2020). A few have also investigated the effect of oblique fields (e.g. Banda-Barragán *et al.*, 2016; Grønnow *et al.*, 2018). These studies have found that Kelvin-Helmholtz instabilities are reduced in the presence of strong magnetic fields. Aligned magnetic fields have the capability to form a high magnetic pressure flux rope, while transverse fields are stretched along the front of the cloud, resulting in a magnetic pressure that is comparable to the ram pressure from the wind. Self-contained and turbulent magnetic fields have been found to suppress the disruption of the clouds and result in smaller fragments comoving with the wind (Li *et al.*, 2013; McCourt *et al.*, 2015; Banda-Barragán *et al.*, 2018).

It is clear that magnetic fields play an important role in the evolution of the entrained clouds, though most studies have been limited to the early stages of the interaction. As clouds are accelerated through the wind, simulation domains have been too small to follow them for long enough to fully understand the evolution of the wind-cloud interaction. In addition, many MHD studies have focused on models without radiative cooling, such that the combined effects of radiative cooling and magnetic fields have not been well constrained. In the few studies that have considered both (i.e. Johansson and Ziegler, 2013; McCourt *et al.*, 2015; Gronke and Oh, 2019), the parameter space of cooling timescales and field orientations has not been fully investigated.

Here we consider both the effects simultaneously, making comparisons across two magnetic field orientations and highlighting the impact of orientation on cooling efficiency. We consider the dependence of the cloud evolution on spatial resolution as well as the stability of MHD clouds as compared to the non-magnetized case. Ra-

Table 2.1: Absolute Values of Wind and Cloud Parameters

Variable	Value
$R_{\rm cloud}$	100 pc
$\rho_{\rm cloud}$	10^{24} g cm^{-3}
$\rho_{\rm wind}$	10^{27} g cm^{-3}
$T_{\rm hot}$	10^{7} K
$T_{\rm cloud}$	10^{4} K
$v_{\rm hot}$	1700 km/s
$t_{\rm cc}$	1.8 Myr
$N_{\rm cool}$	$10^{17.5}$ cm^{-2}
$t_{\rm cool}$	1.84 yr

diative cooling is treated the same throughout all simulations. We track the clouds for several cloud-crushing times with the use of a frame-changing routine in order to study the long-term evolution (Paper I, Paper II).

The structure of this paper is as follows. In Section 2.2 we discuss the simulations and the physics relevant to cloud evolution and the parameter space. In Section 2.3 we discuss the results of the simulations emphasizing on the effects of magnetic fields, radiative cooling, and numerical resolution. We conclude in Section 2.4 with a discussion and summary.

2.2 Simulations

We performed a suite of MHD simulations of wind-cloud interactions including radiative cooling, using the code FLASH (version 4.0.1 Fryxell *et al.*, 2000; Dubey *et al.*, 2008). These simulations were done in three dimensions and made use of the HLL3R Riemann scheme (Waagan *et al.*, 2011), which provides a stable solution in problems that involve strongly magnetized flows and high Mach numbers, with

improved efficiency over the standard solvers within FLASH. Divergence cleaning is implemented with the existing scheme within FLASH; a parabolic cleaning method (Marder, 1987).

The simulations assumed an initial cloud radius of 100 parsecs, a cloud temperature of 10^4 K, a mass density of $\rho = 10^{-24}$ g cm^{-3} and a mean particle mass of $\mu = 0.6$. Initially, the cloud was positioned at (0,0,0) within the domain covering -800×800 parsec in x and z and -666×1333 parsec in y, which was the direction of the hot, outflowing material. The interaction at the y-boundary was defined by a condition where the incoming material is added to the grid and given the same values of density, velocity ($v_{\rm hot}$), sound speed ($c_{\rm s,hot}$) and magnetic pressure as the initial wind conditions. For all other boundaries, the FLASH "diode" condition was used, which assumes the gradient normal to the edge of the domain to be zero for all variables except pressure and only allows material to flow out of the grid.

In order to resolve instabilities along the boundary of the cloud without drastically increasing the computation time, the simulations make use of FLASH's adaptive mesh refinement (AMR) capabilities (Berger and Colella, 1989). As in our previous studies, cells were refined according to the magnitude of the second derivative of density and temperature of the gas, but we also adopted a set of additional refinement and de-refinement criteria, chosen to minimize the computational cost of the simulation while at the same time maintaining the most accurate results possible in the spatial regions that are the most important to the evolution of the cold cloud (see Paper 1 for details). In the high-resolution case, five levels of refinement are used, with the cloud gas maintaining the highest level through the simulation. In this case, the lowest level of refinement produces 4 cells per initial cloud radius while the highest level of refinement provides 64 cells per cloud radius. For the low-resolution simulations, only four levels of refinement are used with 4 cells per cloud radius at the lowest level and

32 cells per cloud radius at the highest level.

In order to follow the disruption of the clouds over long timescales, it was necessary for the simulations to shift frames as the cloud is accelerated by the wind. This was implemented with the use of an automated frame-change routine originally discussed in Paper I. Similarly, we also use a scalar to track cloud material, $C_{\rm cloud}$. Initially, this scalar is set to 0 within the wind and 1 in the cloud. As the gases mix, the scalar reflects the fraction of material within each cell that originated within the cloud.

2.2.1 Physics of Cloud Evolution

There are two key timescales relevant to the evolution of a cloud embedded within a magnetized hot wind. The first, the cloud-crushing time, effectively describes the amount of time it would take the initial internal shock to travel halfway through the cloud. It is given by

$$t_{\rm cc} = \frac{R_c \chi_0^{1/2}}{v_{\rm hot}}, \tag{2.1}$$

which, for a consistent cloud radius, is dependent only on the velocity of the wind, $v_{\rm hot}$, and the density ratio between the cloud and the wind, χ_0 (e.g. Klein *et al.*, 1994).

In addition, the cooling time, which determines the time for the cloud to radiate away its thermal energy is given by

$$t_{\rm cool} = \frac{(3/2) n_c k_B T}{\Lambda(T) n_{e,c} n_{i,c}}, \tag{2.2}$$

where T is the temperature and $\Lambda(T)$ is the equilibrium cooling function at T with n_c, $n_{e,c}$ and $n_{i,c}$ being the total, electron and ion number densities within the cloud. The cooling rate is taken from the tables constructed by Wiersma *et al.* (2009) with

the assumption that the material is always solar metallicity. If the ratio of $t_{\rm cool}/t_{\rm cc} = N_{\rm cool}/(n_{i,c}r_c)$ with $N_{\rm cool} \equiv 3k_BTv_{\rm hot}n_c(2\Lambda\chi^{1/2}n_{e,c})^{-1}$ is below one, then cooling will have a significant influence on the evolution of the cloud as it will have a chance to cool prior to being disrupted by the shock. For these simulations $t_{\rm cool}/t_{\rm cc} \approx 1 \times 10^{-6}$ implying very efficient cooling through the evolution of the clouds.

While the absolute value of the cloud crushing time changes with the radius of the cloud, the ratio $t_{\rm cool}/t_{\rm cc}$ and therefore the evolution of the cloud, is only dependent on $N_{\rm cool}$ and $M_{\rm hot}$. When considered in units of the cloud crushing time, the evolution of the cloud is not dependent on the size of the cloud for a given $N_{\rm cool}$ and $M_{\rm hot}$. A smaller or denser cloud will evolve in a longer amount of absolute time but will reflect the same evolution in units of the cloud-crushing timescale as a larger cloud with the same $N_{\rm cool}$ and $M_{\rm hot}$. Absolute values for these particular clouds are listed in Table 2.1.

An important relation for magnetic fields is the plasma β, the ratio of the thermal and magnetic pressures

$$\beta = \frac{P_{\rm th}}{P_{\rm mag}} = \frac{(\rho/\mu m_p)k_BT}{B^2/(2\mu_0)}, \tag{2.3}$$

with ρ the density, μ again the mean particle mass, T the temperature, B the magnetic field strength and the constants being proton mass (m_p), the Boltzmann constant (k_B) and magnetic permeability of free space (μ_0). This is one of the parameters used to describe the magnetic fields within the simulations.

The ideal system of MHD equations with radiative cooling solved by FLASH in conservation form, with I_3 denoting the 3×3 identity matrix, is,

$$\rho_t + \nabla \cdot (\rho \boldsymbol{u}) = 0, \tag{2.4}$$

$$(\rho \boldsymbol{u})_t + \nabla \cdot \left[\rho \boldsymbol{u} \times \boldsymbol{u} + \left(p + \frac{1}{2}|\boldsymbol{B}|^2\right) I_3 - \boldsymbol{B} \times \boldsymbol{B}\right] = 0, \tag{2.5}$$

$$E_t + \nabla \cdot \left[\left(E + p + \frac{1}{2}|\boldsymbol{B}|^2\right)\boldsymbol{u} - (\boldsymbol{B} \cdot \boldsymbol{u})\,\boldsymbol{B}\right] + \dot{E}_{\rm cool} = 0, \tag{2.6}$$

$$\boldsymbol{B}_t + \nabla \cdot (\boldsymbol{B} \times \boldsymbol{u} - \boldsymbol{u} \times \boldsymbol{B}) = 0, \tag{2.7}$$

$$\nabla \cdot \boldsymbol{B} = 0, \tag{2.8}$$

with ρ the density, $\boldsymbol{u}$ the velocity, $p = k_B T \rho/(\mu m_p)$ the pressure and $E = p/(\gamma - 1) + \frac{1}{2}\rho|\boldsymbol{u}|^2 + \frac{1}{2}|\boldsymbol{B}|^2$ the total energy density. The solver presented in Waagan *et al.* (2011) makes use of a second-order scheme with an entropy-stable approximate Riemann solver. This solver uses primitive variables with relaxation solvers which helps reproduce material contact discontinuities. It has been found to have increased efficiency and stability especially for high Mach number flows and low plasma β. Both of these are directly applicable to this study.

Our simulations also account for radiative cooling. In the optically-thin limit, the additional change in energy due to cooling, the radiated energy per unit mass $\dot{E}_{\rm cool}$, is given by

$$\dot{E}_{\rm cool} = (1 - Y)\left(1 - \frac{Y}{2}\right)\frac{\rho\Lambda}{(\mu m_p)^2}, \tag{2.9}$$

where ρ is the density, $Y = 0.24$ is the helium mass fraction, $\mu = 0.6$ is the mean atomic mass, m_p is the proton mass and Λ is the cooling rate as a function of temperature and metallicity. Heating by a photoionizing background was not included in the calculations, and sub-cycling was implemented (Gray and Scannapieco, 2010) along with a cooling floor at $T = 10^4$K.

2.2.2 Parameters

The wind is described by three parameters, $M_{\rm hot}$, $v_{\rm hot}$ and $T_{\rm hot}$. The Mach number of the inflowing material, $M_{\rm hot}$, reflects the conditions at a particular radius from the outflowing region while the velocity of this hot medium, $v_{\rm hot}$, captures both the energy and mass input from the wind (Chevalier and Clegg, 1985). The temperature of the wind is denoted by $T_{\rm hot}$ while the cloud is always at an initial temperature of 10^4

K, the minimum temperature attainable with atomic cooling. For a cloud at this initial temperature, the Jeans length is $\lambda_J \approx 2$ kpc, much larger than the size of the clouds considered. This implies that the clouds must be confined by pressure in order to be in equilibrium at the start of the simulation and means that self-gravity (not included) is not important for this particular setup. Due to this, the ratio of the cloud density to the wind density, χ_0, is equal to the ratio of the temperatures of the wind and cloud.

The magnetic fields are determined by two parameters, plasma beta, β, the ratio of thermal to magnetic pressure, and the angle with respect to the wind velocity. Since the wind and cloud are originally in pressure equilibrium, the initial plasma β holds for all phases. We adopt $\beta = 10$; corresponding to a field strength of 1.86 μG for most runs with an additional two runs with an initial $\beta = 1$ (5.88 μG). These values reflect the lower limits of magnetic fields seen in observations of galactic outflows (Adebahr *et al.*, 2017). The Alfvenic Mach number for these simulations is ~ 91 and ~ 28 for $\beta = 10$ and $\beta = 1$ respectively.

We then consider two different orientations for the field: aligned and transverse. The aligned case implies an angle of 0° between the field lines and the wind velocity with the only component of the field being in the y-direction. The transverse case describes field lines perpendicular to the wind velocity with the only component of the field being in the x-direction. Initially, the z-component of the field is always taken to be zero.

A table of parameters is shown in Table 2.2 outlining the name of the simulation, magnetic field direction, resolution, and the inclusion of radiative cooling. We focus on the primary case with a Mach number of 3.5 with wind parameters of $T_{\rm hot} = 10^7$ K, $v_{\rm hot} = 1700$ km/s, and $\chi_0 = 1000$. We also consider the complementary, non-MHD run discussed in Paper I. The speed of the hot phase of the Milky Way's wind has

Table 2.2: Simulation parameters

Name	B-field Angle	β	Resolution (cells/r_{cloud})	Cooling
H-rad-lr	-		32	✓
H-rad-hr	-		64	✓
H-nonrad-hr	-		64	
A-rad-lr	Aligned	10	32	✓
A-nonrad-lr	Aligned	10	32	
A-rad-hr	Aligned	10	64	✓
A-nonrad-hr	Aligned	10	64	
A-B1-rad-hr	Aligned	1	64	✓
T-rad-lr	Transverse	10	32	✓
T-nonrad-lr	Transverse	10	32	
T-rad-hr	Transverse	10	64	✓
T-nonrad-hr	Transverse	10	64	
T-B1-rad-hr	Transverse	1	64	✓

been estimated to be upwards of 1000 km/s (Carretti *et al.*, 2013; McClure-Griffiths *et al.*, 2013), while these are the upper estimates, this study is relevant to the hot phase in galactic winds as well as applicable to the general study of the interaction of magnetized clouds and hot winds.

2.3 Results

We carried out 10 simulations, which span the parameters in Table 2.2. These include 8 MHD runs and 2 pure-hydro runs that use the standard directionally split Piecewise-Parabolic Method (Colella and Woodward, 1984) and complement the run

carried out in Paper I. In that paper, we showed that in the radiative non-MHD case the evolution of the cloud converges at a resolution of $R_{\rm cloud}/64$. In order to test convergence, while keeping computational costs manageable, the MHD cases are run on a base grid of $64 \times 80 \times 64$ with three and four additional levels of refinement for the low and high resolution runs, respectively. At the most refined level this corresponds to resolutions of $R_{\rm cloud}/32$ and $R_{\rm cloud}/64$. The domain extends over a physical volume of -800 to 800 parsec in x and z and -666 to 1333 parsec in y, the direction of the hot outflowing material.

2.3.1 Impact of Radiative Cooling

In the most basic wind-cloud scenario, a non-magnetized wind without cooling, the cloud is destroyed by the reflected shock that is produced as the initial shock wraps around the cloud, at about 2 $t_{\rm cc}$ (e.g. Klein *et al.*, 1994). This shock travels upstream and works to tear apart the cloud, leading to catastrophic mass loss.

Shown in Figures 2.1 and 2.2, are comparisons between the runs without cooling and radiative runs for the hydrodynamic and MHD simulations. Two times are shown, 2 $t_{\rm cc}$ (Figure 2.1) and 4 $t_{\rm cc}$ (Figure 2.2), with the runs without cooling on the top and the radiative runs on the bottom. Similarly, projections through the y-axis are shown in Figures 2.3 and 2.4. It is clear that, regardless of the orientation of the magnetic fields, radiative cooling enhances the amount of dense gas in the cloud core. These dense cores are more stable against instabilities and survive for longer times than their counterparts without cooling. In fact, for the $M_{\rm hot} = 3.5$ case modeled here, the radiative clouds take almost twice as long as the non-cooling clouds to reach the point at which 50% of the cloud mass is left. The specifics of the impact on mass loss are discussed in Section 2.3.5.

Radiative cooling allows the clouds to compress into dense cloudlets and remain

intact roughly twice as long as clouds without cooling. This is true in all cases; the hydrodynamic runs, as well as the MHD runs, with both magnetic field orientations. With magnetic fields impacting the clouds' ability to compress, it is clear that they will also have an impact on cooling efficiency. This connection has been discussed before (Fragile *et al.*, 2005) emphasizing that the transverse fields will enhance cloud compression and increase the cooling efficiency, while aligned fields will have the opposite effect by inhibiting compression. While we do see increased compression in the transverse field cases, this does not necessarily translate to dense structures that survive over longer timescales than the other runs. A direct comparison to Fragile *et al.* (2005) is difficult to make as their simulations were in two dimensions and make use of a different cooling floor. However, our results are in qualitative agreement with their conclusions that radiative cooling extends cloud lifetimes while magnetic fields can either enhance or resist compression depending on the field orientation.

2.3.2 Influence of Aligned Fields

The disruption and morphology of the cloud differ significantly between runs H-rad-hr and A-rad-hr, which are shown in the bottom left and center panels, respectively, of Figures 2.1 and 2.2. The cloud in A-rad-hr (center) is compared to H-rad-hr (left) showing slices of the cloud density and β at 2 $t_{\rm cc}$ (Figure 2.1) and 4 $t_{\rm cc}$ (Figure 2.1). The cloud within the magnetized wind is compressed at early times much like H-rad-hr, however, the tail downwind of the cloud appears smoother in the MHD case. This is expected as strong magnetic fields aligned to the flow have been shown to inhibit the growth of Kelvin-Helmholtz instabilities (Chandrasekhar, 1981; Banda-Barragán *et al.*, 2016). In general, this creates a tail of cloud material flowing behind the cloud that is much less turbulent than the tail in H-rad-hr.

These elongated tails in A-rad-hr are also regions where the magnetic pressure is

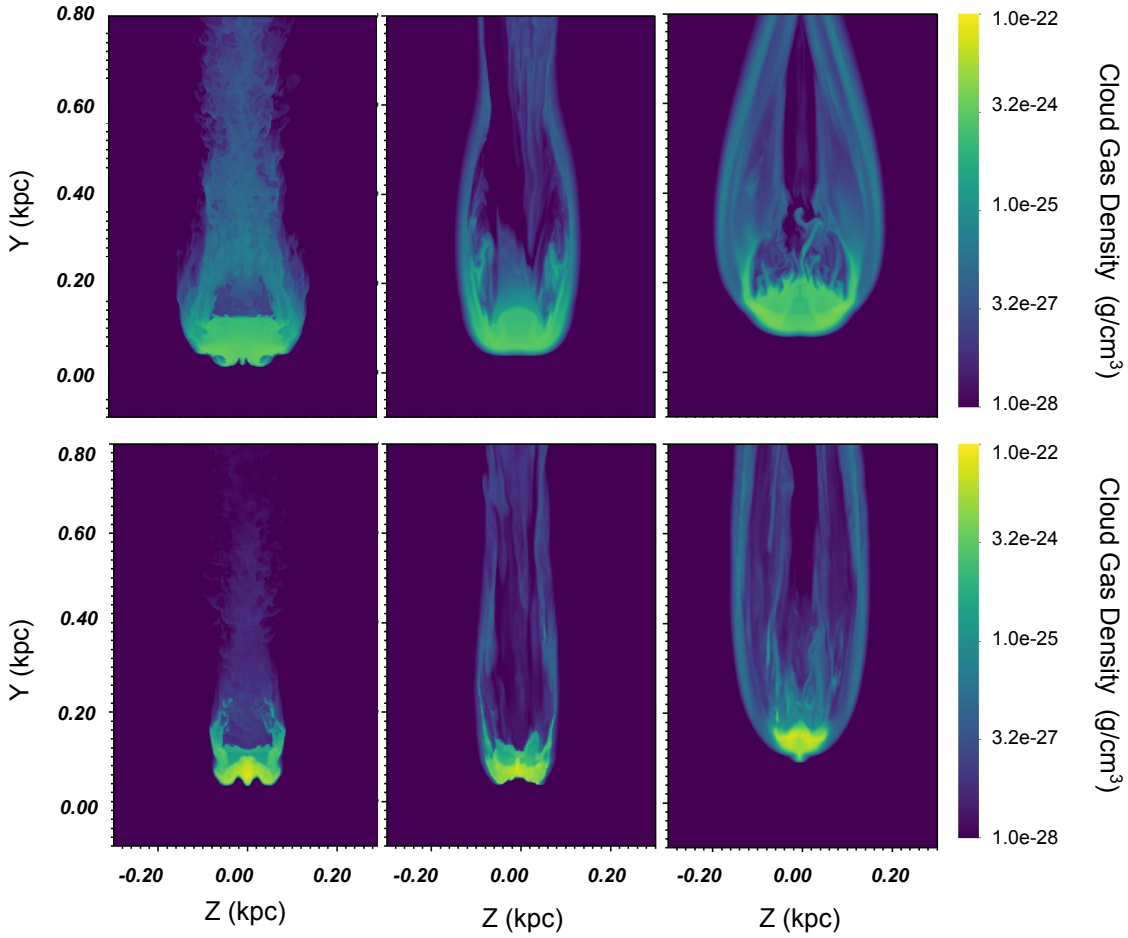

Figure 2.1: Slices along the x-axis of the cloud density comparing the non radiative runs (top) with radiative runs (bottom) at 2 t_{cc}. The hydrodynamic runs are shown on the left, aligned fields in the middle, and transverse fields on the right. All densities are given in g/cm^{-3} and all lengths are given in kpc. These are zoomed-in images of the more extended computational domains.

comparable to the thermal pressure ($\beta \sim 1$) as shown in the left panels in Figure 2.5. These tails are similar to the "flux rope" first described by Mac Low *et al.* (1994). In that study, field lines are pulled by the shock. As the wind passes the back of the cloud, surrounding gas fills in the space left by the higher velocity post-shock gas. This filling-in effect works to compress the field lines, resulting in an amplification of the magnetic field. Here we see the same amplification, with a similar structure to the ropes observed in Shin *et al.* (2008).

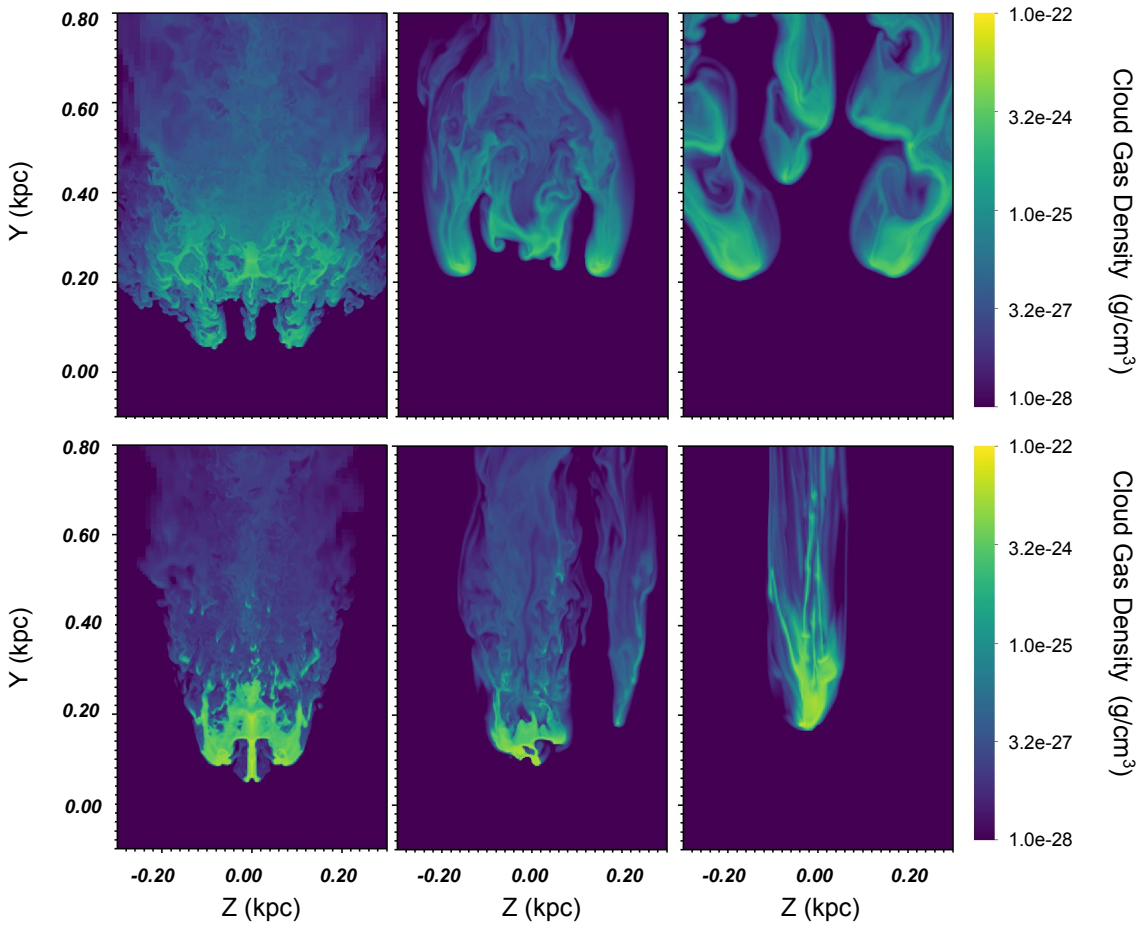

Figure 2.2: Same as Figure 2.1 but at 4 $t_{\rm cc}$.

These regions of amplified magnetic field also lead to notable differences in the evolution at later times. While H-rad-hr results in a few dense cloudlets that are slowly peeled away, the cloud in A-rad-hr is much more expanded and breaks up abruptly shortly after 5 $t_{\rm cc}$ with most of the cloud material evolving into lower-density wisps of gas. This is primarily driven by the magnetic pressure increasing faster than the thermal pressure with compression within the tail of the cloud. Thermal pressure is inversely proportional to volume, $P_{\rm th} \propto R^{-3}$, while magnetic pressure scales with radius as, $P_{\rm mag} \propto R^{-4}$. This results in magnetic pressure in the MHD run opposing the compression to a greater extent than thermal pressure in the hydro case. This is most important for the material between the flux ropes. While the amplified ropes

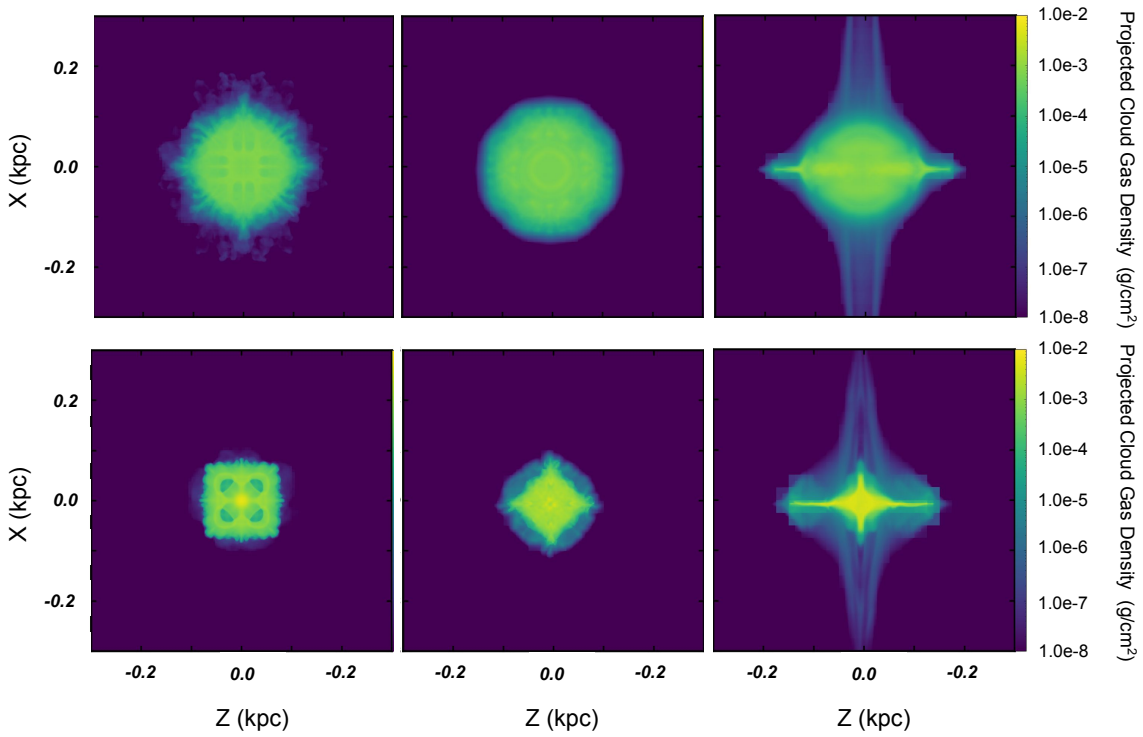

Figure 2.3: Projections along the y axis of the cloud density comparing the non-radiative runs (top) with the radiative runs (bottom) at 2 t_{cc}. The hydrodynamic runs are shown on the left, aligned fields in the middle, and transverse fields on the right. All column densities are given in g/cm^{-2} and all lengths are given in kpc. These are zoomed-in images of the more extended computational domains.

are created by the compression of converging flows, the intermediate material between these flux ropes is kept from condensing, resulting in more wispy fragments. These fragments and filaments are comparable to the structures seen in other studies (e.g. Fragile *et al.*, 2005; Shin *et al.*, 2008). It is also worth noting the filament to the right, and the apparent asymmetry in the aligned field case at 4 t_{cc} in Figure 2 is likely caused by the amplification of tiny numerical differences, due to the growth of instabilities.

The inclusion of radiative cooling has the same effect on clouds embedded in aligned fields as it does in the hydrodynamic case. The cloud condenses into a dense core which then takes more time to be pulled apart by instabilities. The aligned fields

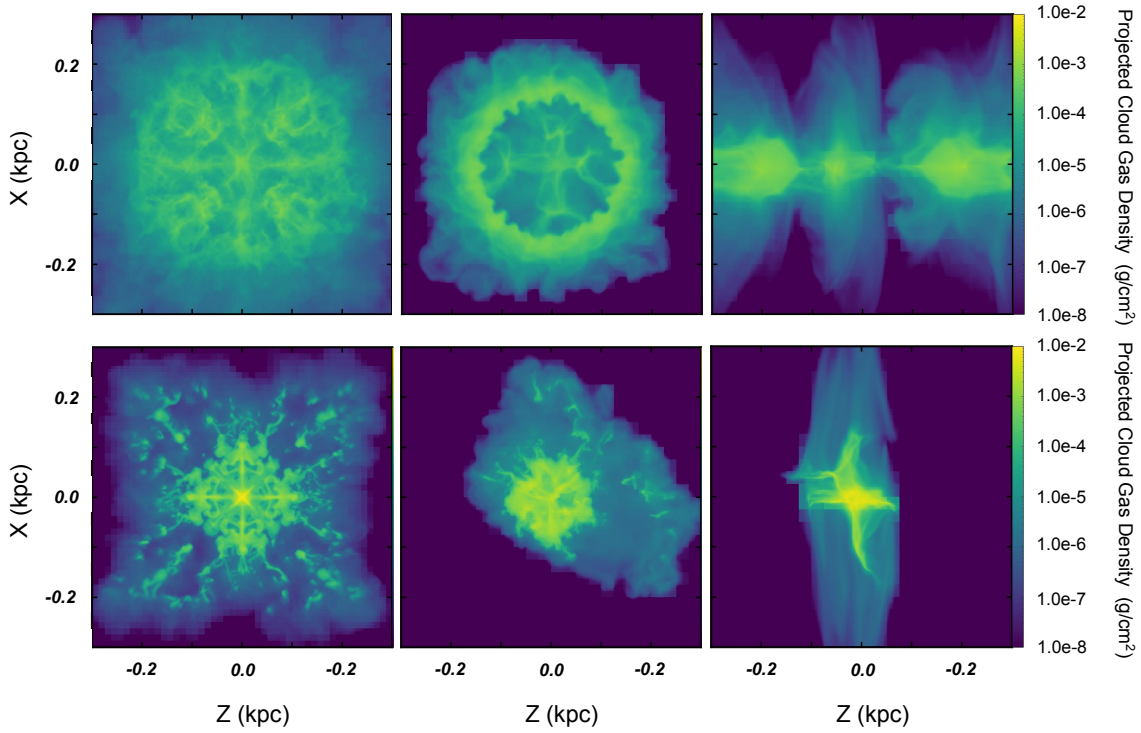

Figure 2.4: Same as Figure 2.3 but at 4 t_{cc}.

may also aid in condensation as discussed in Gronke and Oh (2018). However, our domains do not extend far enough downwind to make a direct comparison. Gronke and Oh (2018) find condensation at lengths $\approx 40r_c$ to $\approx 250r_c$ downwind of the cloud while our domain only extends to $\approx 13r_c$.

2.3.3 Influence of Transverse Fields

We next consider the wind-cloud interaction in the case with transverse fields. Without magnetic fields, the reflected shock works to tear apart the cloud. However, in the case of a transverse field, this reflected shock is not created. Slices of the cloud density for A-rad-hr (bottom center) and T-rad-hr (bottom right) are shown in Figures 2.1 and 2.2. The transverse fields produce a smooth, laminar flow with reduced effects of Kelvin-Helmholtz (KH) instabilities due to the reorienting of the

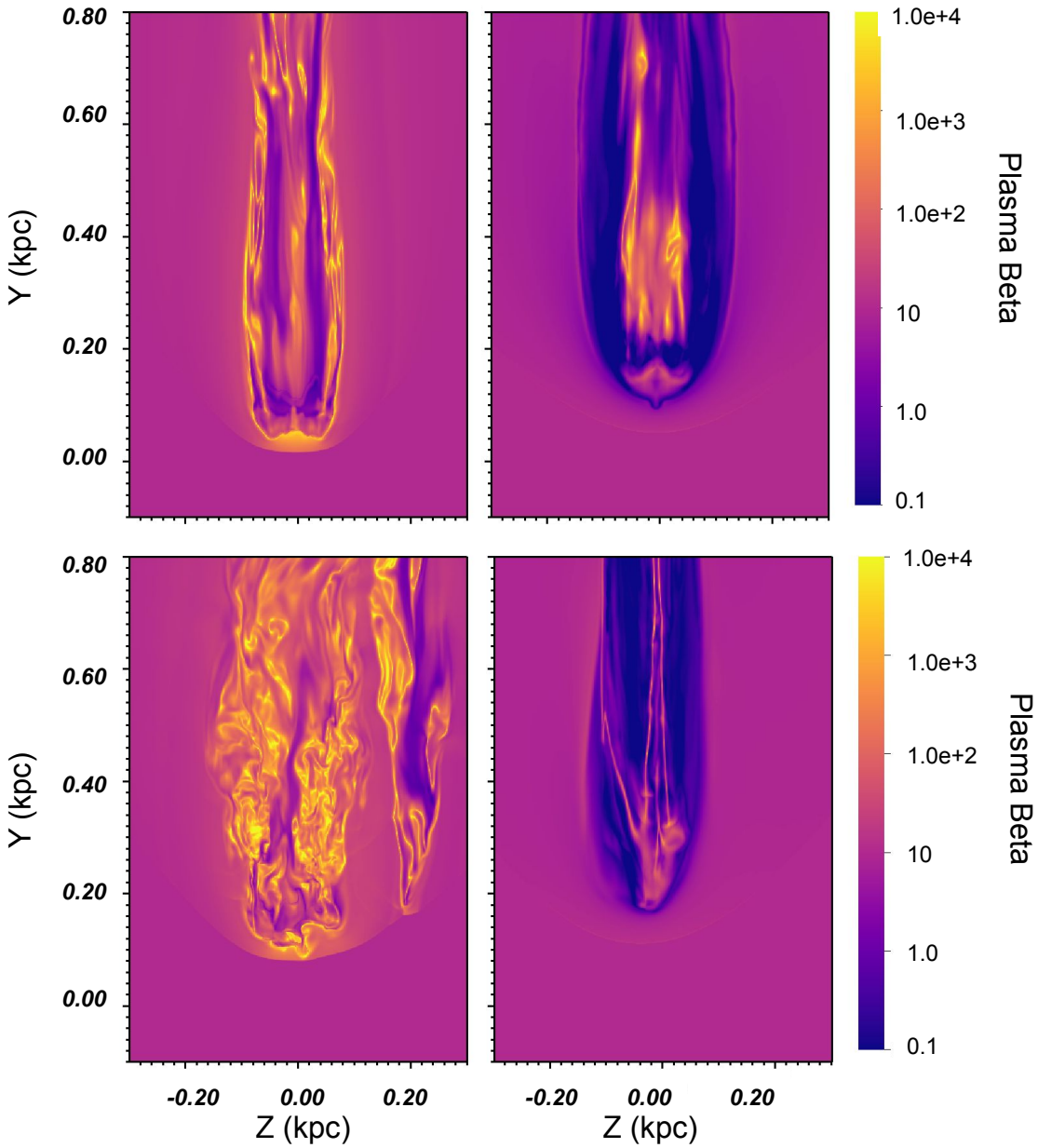

Figure 2.5: Slices along the x-axis of plasma β in A-rad-hr (left) and T-rad-hr (right) at 2 $t_{\rm cc}$ (top) and 4 $t_{\rm cc}$ (bottom). All lengths are given in kpc.

field lines as the wind pulls the lines to be more aligned with the flow. This is similar to what has been observed in previous studies (Orlando *et al.*, 2008; Banda-Barragán *et al.*, 2016; Grønnow *et al.*, 2017, 2018). In the right panels of Figure 2.5, slices of β are shown for T-rad-hr. Most of the cloud material is surrounded by an envelope of gas with $\beta \approx 1$. Here the thermal pressure and magnetic pressure are approximately equal, with the magnetic pressure providing resistance against the shock completely passing through the cloud.

This process of reorienting the field lines is known as magnetic 'draping', and it is an effective mechanism to shield dense gas from the erosive effects of dynamical instabilities as shown in Dursi and Pfrommer (2008) and Banda-Barragán *et al.* (2016). These authors highlighted the potential of this effect to protect the cloud, increasing its stability and lifetime. While we also see evidence that magnetic draping suppresses instabilities, we find that it does not ultimately increase the longevity of the cloud. In fact, the re-orientation of the field lines leads to another effect that causes cloud mass to be lost more quickly than the disruption from instabilities seen in the aligned and hydrodynamic cases.

In the draping case, the magnetic field lines are pulled up sharply with the wind, causing an increase in magnetic pressure which pushes cloud material in the only free direction, the z-direction. In Figure 2.6, the velocity of the cloud perpendicular to the wind is shown for T-rad-hr and A-rad-hr. In A-rad-hr, there is symmetry between the x- and z-velocities with material primarily flowing only far enough to get around the leading edge of the cloud. For T-rad-hr, the cloud preferentially flows in the z-direction; much further than the original leading edge of the cloud, and at higher speeds than the A-rad-hr material. This asymmetry is similar to that observed in previous studies (i.e. Gregori *et al.*, 1999; McCourt *et al.*, 2015; Grønnow *et al.*, 2017).

In particular, our results are in agreement with Gregori *et al.* (1999), which shows the asymmetry produced by the expansion in the direction orthogonal to both the wind and field orientation in transverse field scenarios. Gregori *et al.* (1999, 2000) also describe the role of Rayleigh-Taylor (RT) instabilities in forming a C-like structure at later times. The effects of these instabilities are amplified as the field lines become trapped and tangled at the front of the cloud (Banda-Barragán *et al.*, 2016; Grønnow *et al.*, 2017). With trapped field lines, the timescale of the growth of the RT instabilities is shortened, causing the front of the cloud in the simulations with transverse fields to be torn apart faster than in the aligned field or non-magnetized simulations. These amplified instabilities are responsible for the finger-like filaments seen in Figure 2.2.

The squeezing of the cloud by the field lines produces a cloud with a more flattened appearance along the direction perpendicular to the wind and magnetic field lines (see the right-hand side panels of Figures 2.3 and 2.4. This shape is also shown in the volume rendering in Figure 2.7. Compared to the cloud within the aligned field, the cloud within the transverse field maintains the smooth flow of mass downwind. At early times T-rad-hr is flattened and flowing around the core in the z-direction while A-rad-hr appears symmetric with a more bullet-like shape. At later times T-rad-hr maintains this flattened shape as more material flows off of the core. A-rad-hr is more turbulent as cloud material is being torn away by dampened, but present, hydrodynamic instabilities. This flattening of the cloud is in agreement with Shin *et al.* (2008) in which similar simulations produced sheet-like clouds parallel to the post-shock magnetic fields. Again, the apparent asymmetry at late times is likely caused by the amplification of tiny numerical differences (floating-point differences), due to the growth of linear instabilities.

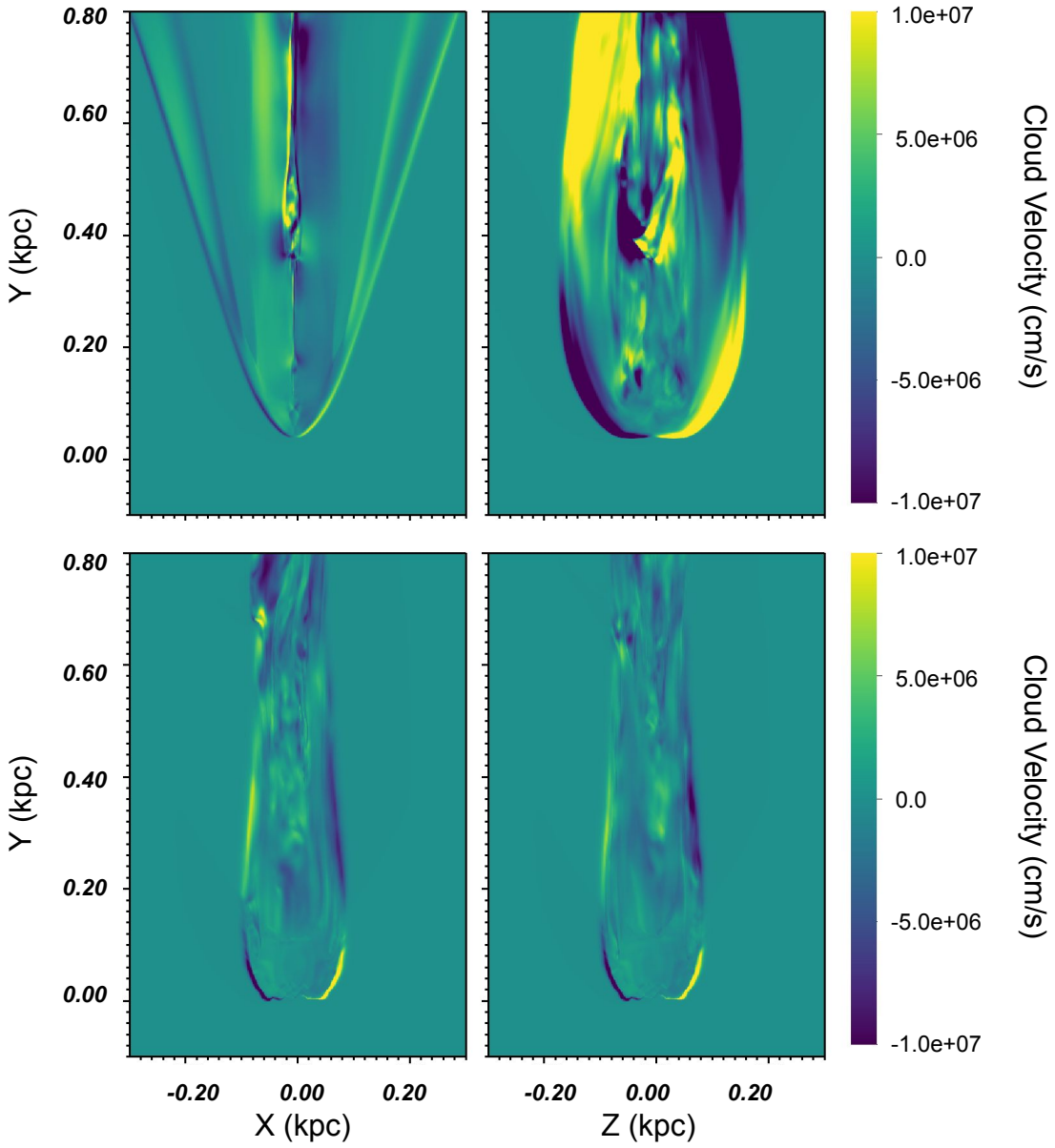

Figure 2.6: Slices of the cloud velocity perpendicular to the wind [x left; z right] comparing T-rad-hr (top), and A-rad-hr (bottom) at 1.4 t_{cc}. While the flow in A-rad-hr is symmetric, T-rad-hr preferentially flows in the z direction around the core of the cloud.

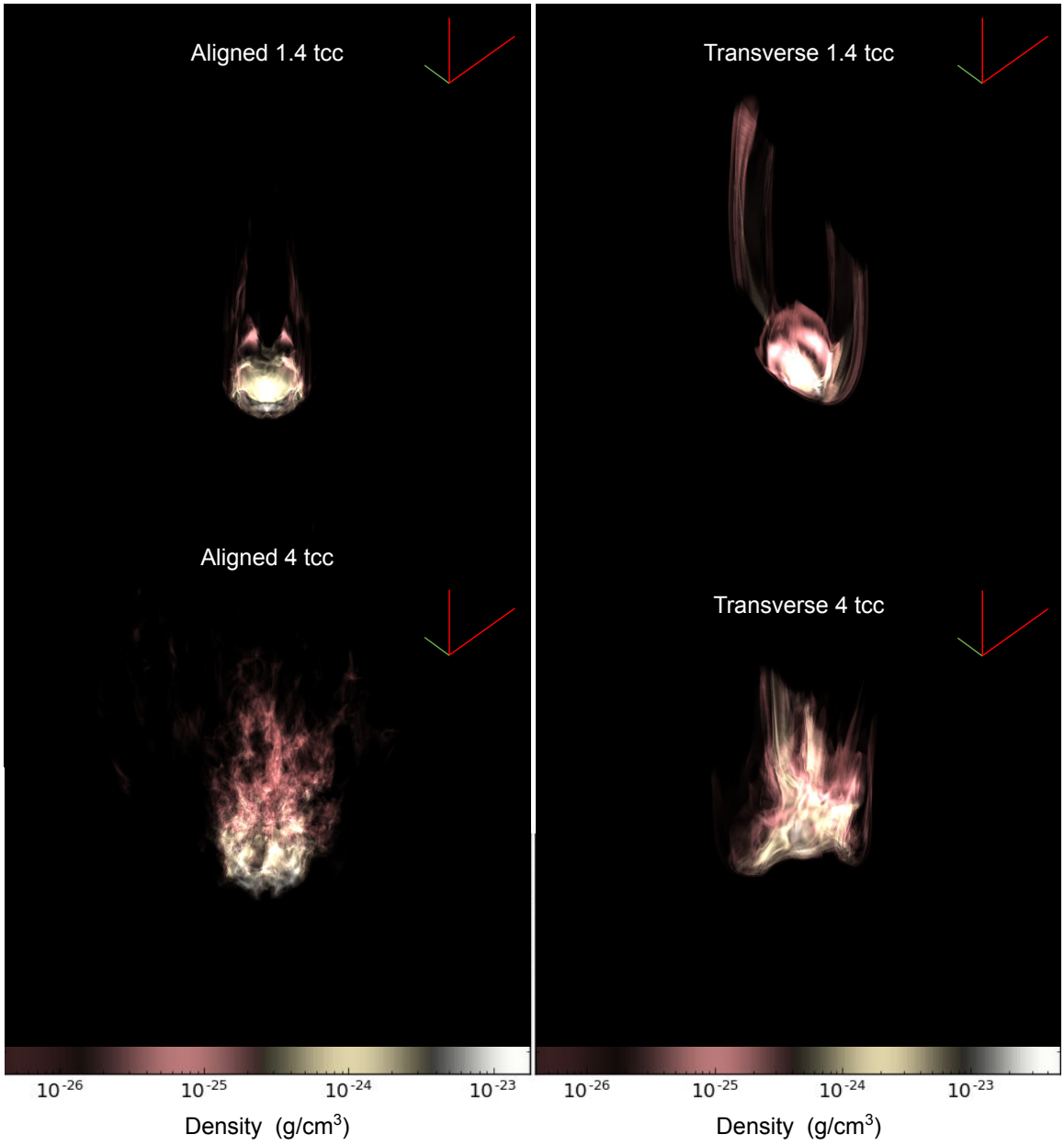

Figure 2.7: Volume renderings of density for A-rad-hr and T-rad-hr at 1.4 t_{cc} and 4 t_{cc}. There is clear asymmetry in T-rad-hr, which is flattened in the direction perpendicular to both the flow and magnetic fields.

2.3.4 Strong Fields

In addition to studying the effect of field orientation, we have investigated the effects of a stronger field. We consider each orientation, aligned and transverse, with an initial $\beta = 1$, this results in a field ~ 3 times stronger than the $\beta = 10$ cases. Slices and projections of the cloud density in these two strong field runs are shown in Figures 2.8 and 2.9.

In A-B1-rad-hr, the aligned strong fields lead to a significantly denser core than in A-rad-hr. However, as noted in previous studies (Fragile *et al.*, 2005), the strong field suppresses low-temperature cooling, keeping the cloud from forming cloudlets. The main body of the cloud remains smooth as the KH instabilities are suppressed, leaving RT instabilities as the primary cause of destruction. The small 'flux ropes' formed in the tail of the cloud are no longer present, as the tail behind the cloud is made up of cold, low-density gas causing the entire tail of the cloud to have $\beta \sim 1$. At late times the cloud remains confined to a single core.

The squeezing effect seen in T-rad-hr is also apparent in T-B1-rad-hr. However, the destructive effects of the RT instabilities are further amplified with the stronger field causing the cloud to be torn apart from the front much faster. The cloudlets formed in this destruction phase are denser in T-B1-rad-hr than in T-rad-hr, but only up to an order of magnitude, consistent with results in Johansson and Ziegler (2013). As the main cloud is separated into smaller cloudlets, the rapid mass loss is exaggerated. Rather than stabilizing the cloud to allow a longer lifetime, the strong field results in destruction on time scales similar to the non-radiative clouds.

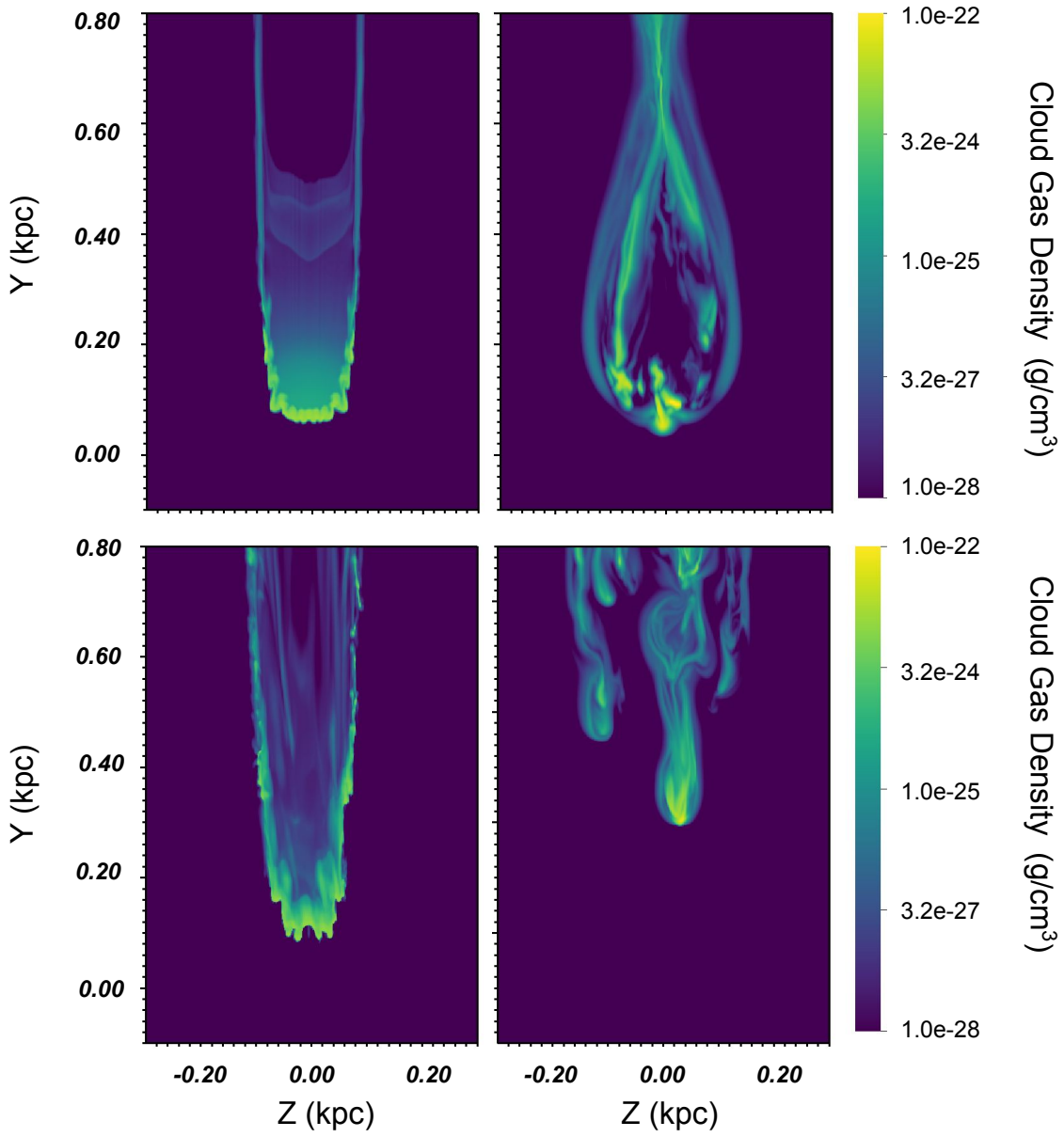

Figure 2.8: Slices along the x-axis of cloud density comparing the strong field runs, A-B1-rad-hr (left) and T-B1-rad-hr (right) at 2 t_{cc} (top) and 4 t_{cc} (bottom). All densities are given in g/cm^{-3} and all lengths are given in kpc. These are zoomed-in images of the more extended computational domains.

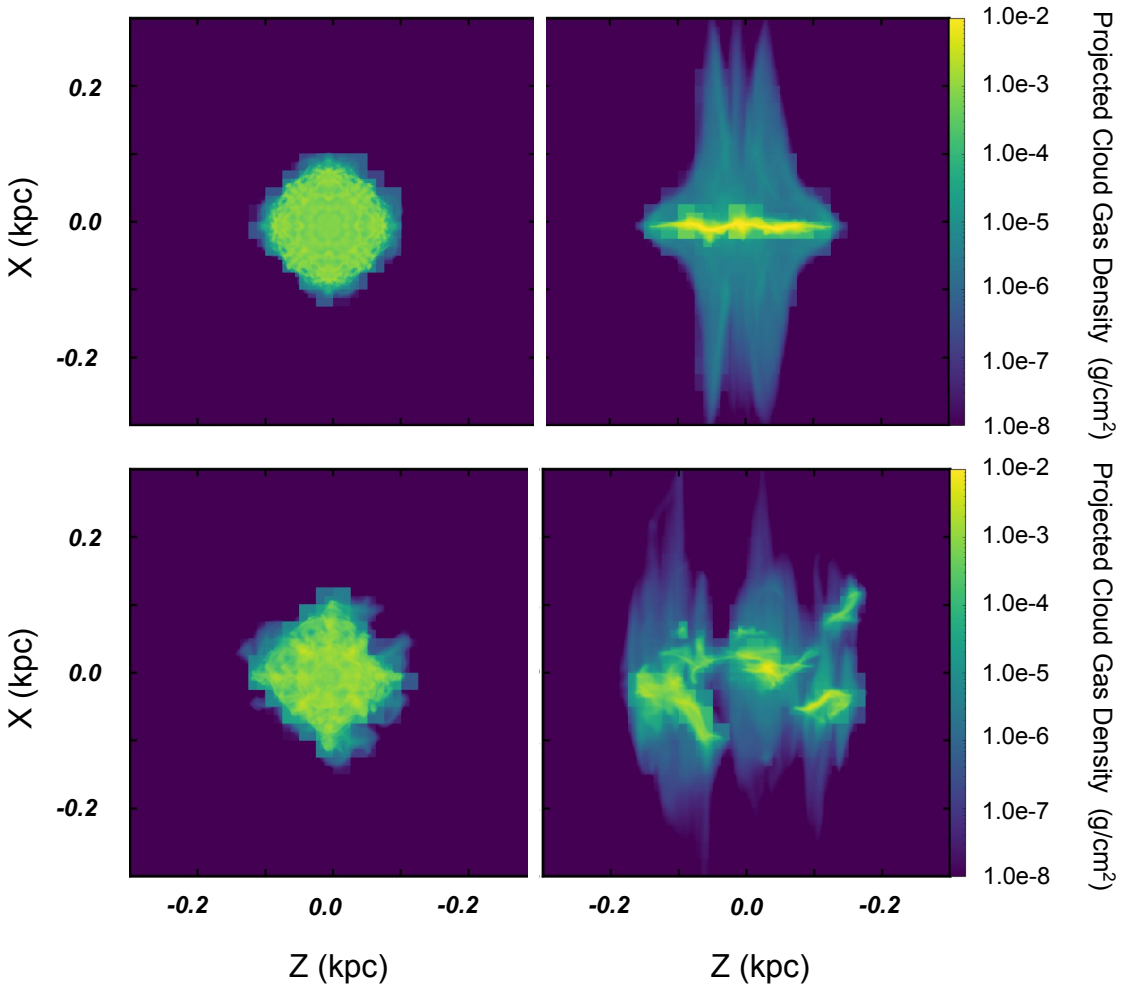

Figure 2.9: Projections through the y-axis of cloud density comparing the strong field runs, A-B1-rad-hr (left) and T-B1-rad-hr (right) at 2 t_{cc} (top) and 4 t_{cc} (bottom). All column densities are given in g/cm^{-2} and all lengths are given in kpc. These are zoomed-in images of the more extended computational domains. The low-resolution boundaries are due to the projection maintaining the resolution along the line of sight, which is dependent on the structure of the adaptive grid.

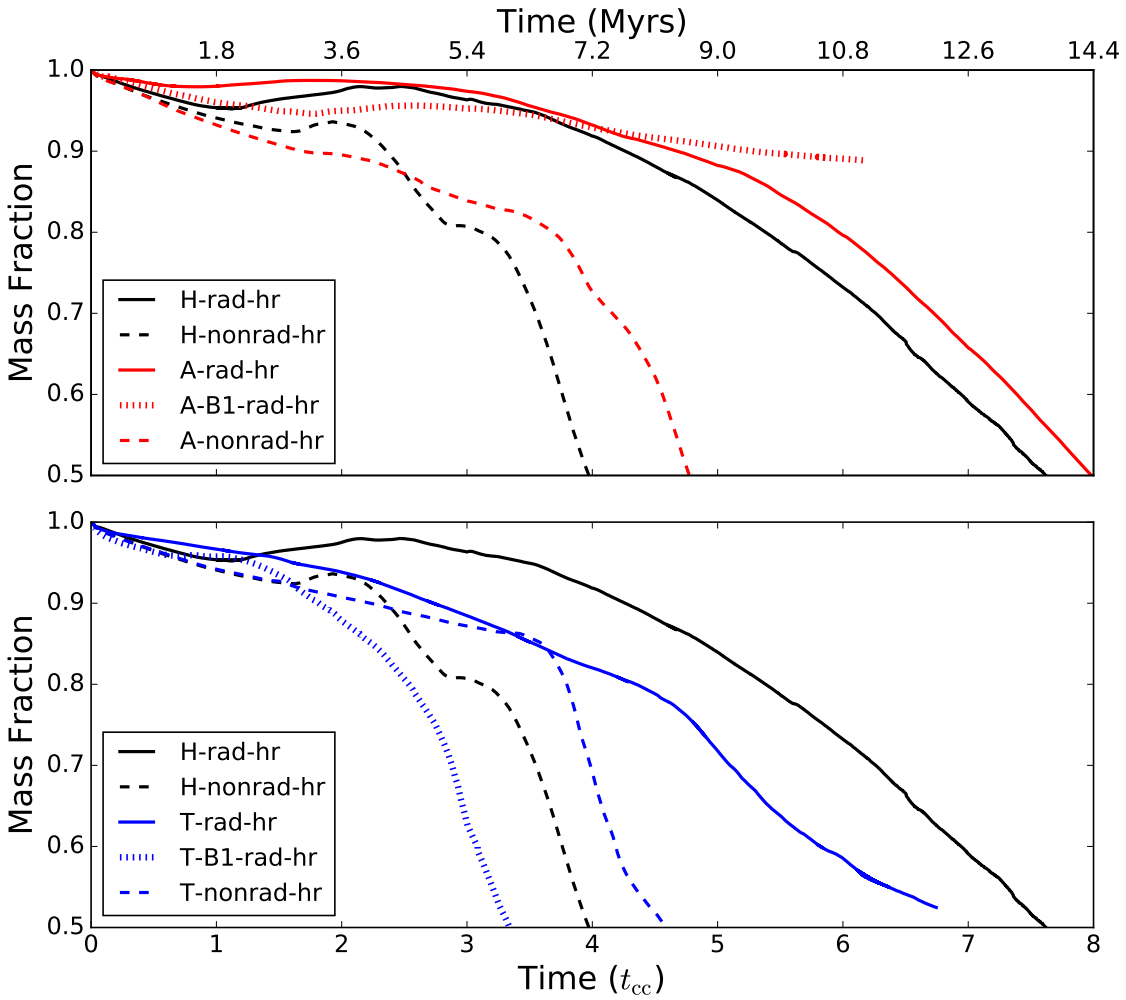

Figure 2.10: Mass fraction of cloud material greater than $\rho_{i,c}/3$ as a function of time in units of cloud crushing times of all high resolution runs. The hydro only simulations are shown in black; the cloud without cooling in a dashed line and the radiative cloud in a solid line. The aligned and transverse fields follow the same pattern in red and blue, respectively. Strong field runs are shown with dotted lines.

2.3.5 Evolution

The morphology of these clouds has a significant impact on their overall evolution. In this section, we consider the evolution of the clouds in three global quantities; cloud mass loss, mixing fraction, and cloud velocity.

In Figure 2.10, the fraction of cloud mass with density $> \rho_{c,i}/3$ is shown as a

function of time for the hydrodynamic and MHD runs. Shown with the solid black line, the radiative hydrodynamic run follows the same mass loss rate as discussed in Paper I, with the fraction of remaining cloud mass staying above 90% throughout the initial stages of the interaction before dropping as the cloud is destroyed by the wind at later stages.

Most notably, the transverse fields (solid blue line) do not appear to prolong the lifetime of the cloud. Rather than retaining a higher mass fraction for the majority of the simulation, T-rad-hr does the opposite. The mass fraction for the cloud with transverse fields decreases almost linearly for the first few cloud crushing times. While magnetic draping does somewhat protect the core of the cloud from shear instabilities, the bent field lines create inward magnetic forces that squeeze the cloud along the field direction and expand it in the perpendicular direction. This produces continuous mass loss as cloud material is carried with the wind. In the protective region that surrounds the cloud, the magnetic field has been amplified to 10 times the strength of the thermal pressure; 100 times greater than the initial magnetic pressure. At later times, the mass loss begins to increase as this region becomes thinner and the cloud material has been reduced to a long thin filament more vulnerable to instabilities. T-B1-rad-hr follows a similar evolution as the squeezing effect causes drastic mass loss at early times. However, the cloud T-B1-rad-hr is quickly torn apart by RT instabilities as the field is tangled in front of the cloud. This leads to the very steady mass loss past 2.5 t_{cc}.

For the aligned fields in A-rad-hr (solid red line), the fields make little impact on the overall evolution, but they do lead to the abrupt break up of the cloud shortly after 5 t_{cc}. Even though the KH short-wavelength instabilities are suppressed, the aligned fields only slightly improve the stability over H-rad-hr throughout the whole simulation. Since A-rad-hr does not form the same dense cloudlets as H-rad-hr, the

extra mass comes from the 'puffy' intermediate gas which breaks up from the main cloud to form filaments and wisps. This material, protected in high magnetic pressure bubbles, remains in the domain longer than material torn off the cloud in H-rad-hr. The mass loss for A-B1-rad-hr is similarly slow. The cloud remains in a single core as the suppressed instabilities are unable to pull it apart and cause mass loss through ablation.

The evolution of the clouds without radiative cooling is distinctly different than those with radiative cooling. Curves for the mass loss for the runs without cooling are also shown in Figure 2.10. At early times, the mass loss for the magnetized runs is either on par with (transverse) or more significant (aligned) than the hydrodynamic run. From this perspective, it may seem that fields do not increase cloud survival. However, at later times the ultimate destruction of the cloud occurs slightly sooner for H-nonrad-hr than either of the MHD runs without cooling. This indicates that while magnetic fields can impact cloud evolution in both the non-cooling and radiative cases, it is the combination of the fields and cooling that must be considered to predict the ultimate fate of the cloud.

As discussed in Section 2.3.3, the steep mass loss rate for the transverse field runs is due to mass being squeezed around the cloud as the magnetic pressure increases. The core of the cloud is embedded in a region of amplified fields with high magnetic pressure. In this region, there is little mixed material resulting in inefficient cooling rates. Due to this, the contribution to stability that radiative cooling provides in the other cases does not influence the primary mechanism for mass loss. It is not until the point that the cloud has become a filament ($\approx 4\ t_{\rm cc}$), with material breaking off through the draping layer does cooling begin to impact the mass loss. In T-nonrad-hr, the more exposed filament is unable to condense and begins to be torn apart causing a sharp decrease in mass. In T-rad-hr the filament is able to achieve a denser structure

leading to the mass falling off at a slower rate, as seen in Figure 2.10.

Given that the A-rad-hr follows H-rad-hr much more closely than A-nonrad-hr, we conclude that the inclusion of cooling in the aligned MHD run has the same effect as it does in the hydrodynamic case. In both cases, it aids in the compression of the cloud, leading to higher core densities and longer lifetimes as well as aiding the condensation of warm gas. The aligned magnetic fields provide resistance to compression in the tail of the cloud which leads to expansion and break up, however they do not inhibit the effect of cooling to stabilize the cloud.

In Figure 2.11 we show the mixing fraction as described in Xu and Stone (1995) and Orlando *et al.* (2005),

$$f_{\rm mix} = \frac{1}{m_{\rm cloud,0}} \int_{(0.1<{\rm C_{cloud}}<0.9)} dV \rho C_{\rm cloud}, \tag{2.10}$$

where $m_{\rm cloud,0}$ is the initial cloud mass, and the integral is computed over the volume in which the tracer $C_{\rm cloud}$ is between 0.1 and 0.9. It is clear that the magnetic fields impact the mixing of material. As discussed in the previous section, the magnetic pressure in A-rad-hr keeps cloud material within the tail of the cloud, which allows the cloud material the opportunity to become mixed with the wind. This is reflected in very high mixing fractions as compared to the other two simulations, especially at later times where larger amounts of cloud material exist in a puffy intermediate phase after the clouds break up. However, A-B1-rad-hr does not have this same sharp increase in mixed material. As hydrodynamical instabilities are the mechanism for mixing, the stronger field case results in decreased mixing in relation to the decrease in disruption by the instabilities. This trend has been observed in previous studies (Orlando *et al.*, 2008). In contrast, the transverse fields lead to very little mixing between the wind and cloud phases, resulting in mixing fractions even lower than H-rad-hr. The protection from the $\beta = 1$ envelope in both T-rad-hr and T-B1-rad-hr

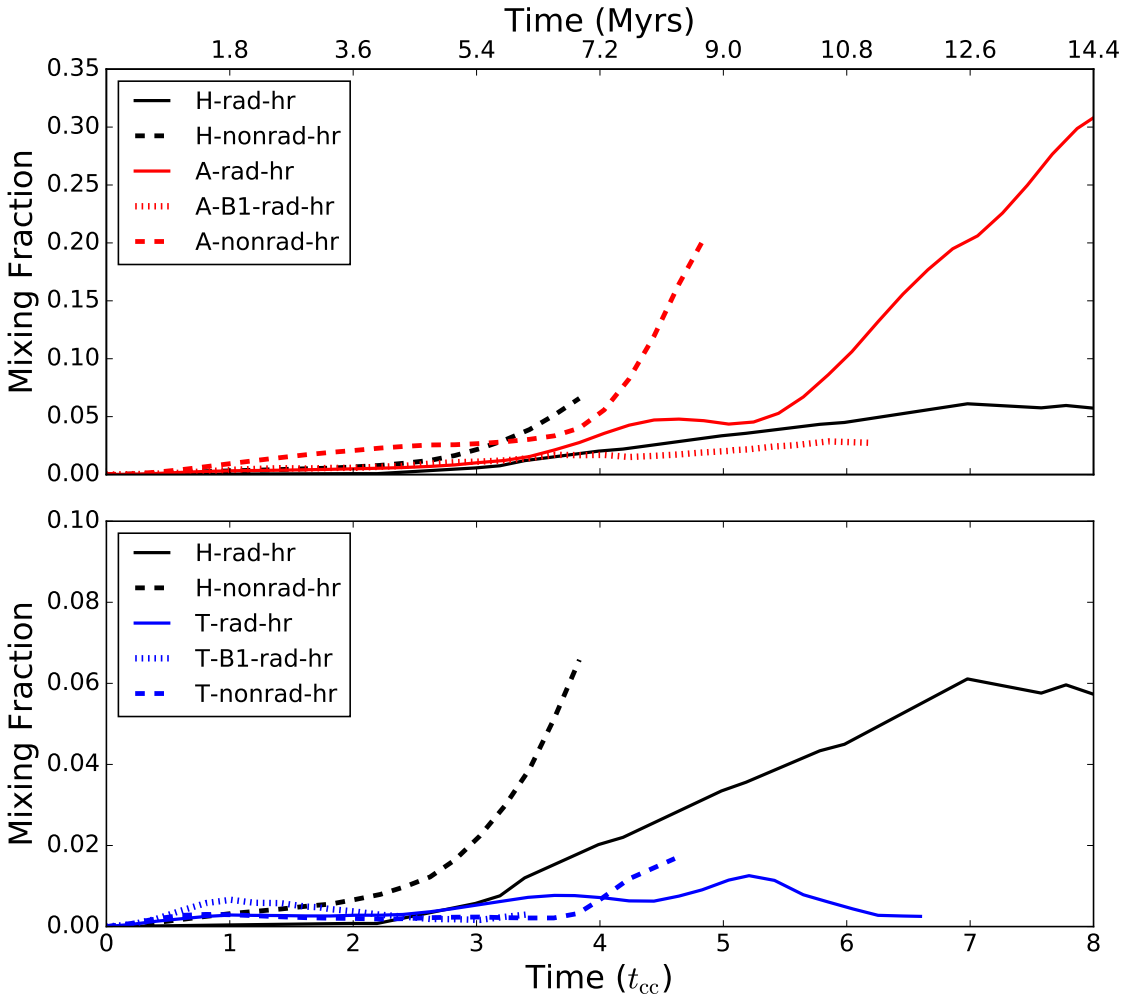

Figure 2.11: Fraction of mixed material over time for both the no-cooling and radiative high resolution runs. The hydrodynamic simulations are shown in black; H-rad-hr as the solid line, H-nonrad-hr as the dashed line. The aligned and transverse fields follow the same pattern in red and blue, respectively. Strong field runs are shown with dotted lines.

effectively confines the cloud material, restricting the possibility of mixing.

For the cases without cooling, the clouds are not able to condense and they become well mixed with the wind in H-nonrad-hr and A-nonrad-hr. The mixing in these clouds increases at later times as the cloud begins to be torn apart by instabilities. Were the simulation to continue well past the point where 50% of the cloud mass was left, the fraction of mixed material would continue to increase as the cloud ablates and drifts downwind. In contrast, for the transverse run without cooling, the $\beta = 1$ envelope is still an effective form of protection, keeping the mixing fraction well below 0.01.

Finally, we consider the impact of magnetic fields on the acceleration of the cloud. In Figure 2.12, the average down-wind velocity of the cloud is shown with time. In the absence of magnetic fields, the cloud is accelerated consistently. For the aligned fields, due to the fact that the magnetic pressure is not in the direction of the acceleration, there is little difference between A-rad-hr and H-rad-hr (in agreement with Jones *et al.*, 1996; Mac Low *et al.*, 1994). The acceleration of the cloud within the transverse fields is much higher than either of the other two runs. From the same magnetic pressure argument, as the transverse field lines are compacted by the flow at the front of the cloud, this leads to an amplification in the magnetic field corresponding to an increase in magnetic pressure. At the leading edge of the cloud, just inside the $\beta = 1$ envelope, the magnetic pressure has been amplified to 100 times the initial pressure. This pressure is at the leading edge of the cloud, pushing in the same direction as the ram pressure acceleration. Due to this additional pressure, the cloud has a larger acceleration in the T-rad-hr run than in the other two runs. This effect is even more apparent in T-B1-rad-hr, where the stronger field leads to an even higher magnetic pressure at the front of the cloud which accelerates the cloud three times faster than in T-rad-hr, in agreement with the increase in initial magnetic field strength from an initial $\beta = 10$ (1.86 μG) to an initial $\beta = 1$ (5.88 μG). In the runs without cooling,

the velocity of the cloud increases similarly to the radiative cases at early times. At later times, without the ability to cool and condense, these clouds are torn apart and accelerated to higher velocities.

The evolutionary trends for these runs can easily be summarized as follows. As most destruction is through forces perpendicular to the wind flow, aligned fields have little to no impact on the mass loss and cloud velocity. However, the additional pressure the magnetic fields provide leads to expansion, break up and higher amounts of cloud mass intermixed with wind material. Conversely, transverse fields lead to increased acceleration and larger amounts of poorly-mixed cloud material being lost from the domain. These effects are both due to the amplification and draping of field lines as they are dragged with the flow of the wind, which also leads to reduced mixing between the cloud and wind materials.

2.3.6 Resolution Effects and Limitations

In Paper I, we discussed the resolution effects on these hydrodynamic simulations with radiative cooling. Considering the same low and fiducial resolutions as in the current paper, $\Delta x = R_{\rm cloud}/32$ and $\Delta x = R_{\rm cloud}/64$, as well as a high resolution run with $\Delta x = R_{\rm cloud}/128$, we highlighted that the under-resolved instabilities in the $\Delta x = R_{\rm cloud}/32$ significantly impact the resulting mass loss estimates. The high-resolution, $\Delta x = R_{\rm cloud}/128$ run, on the other hand, converged to the same solution for mass loss as the fiducial run, but it also captured more diffuse material, leading to higher mixing fractions.

Taking the same approach, we compare the mass loss, mixing fractions and cloud velocity between the high-resolution, $\Delta x = R_{\rm cloud}/64$ and low-resolution $\Delta x = R_{\rm cloud}/32$ runs with and without magnetic fields. In the top panel of Figure 2.13 the mass loss of H-rad-lr is much lower than all other runs, deviating significantly by 4 $t_{\rm cc}$, the

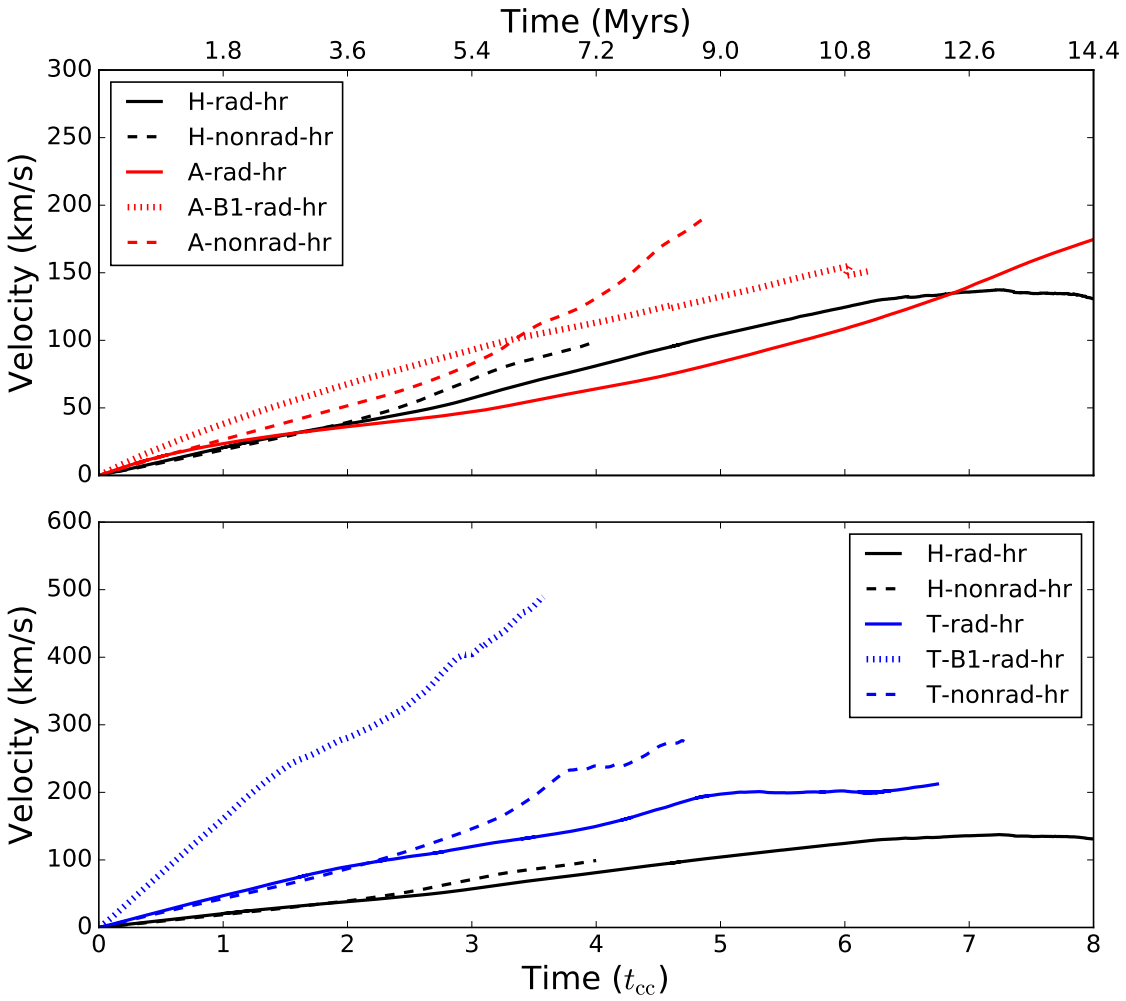

Figure 2.12: Cloud velocity along the flow of the wind as a function of time in units of cloud crushing times of all high resolution runs. The hydrodynamic simulations are shown in black; H-rad-hr as the solid line, H-nonrad-hr as the dashed line. The aligned and transverse fields shown with the same pattern in red and blue respectively. Strong field runs are shown with dotted lines.

same point at which A-rad-hr and A-rad-lr begin to depart from H-rad-hr. This time corresponds to the transition between a single shocked cloud core to several smaller cloud cores as the cloud begins to break up. Unlike the hydro cases, runs A-rad-hr and A-rad-lr are similar to each other and lie between the two estimates from the hydro simulations. Thus it is clear that convergence properties of the aligned cases are better than the hydro cases, and that the $\Delta x = R_{\rm cloud}/64$ resolution of H-rad-hr is sufficient to conclude that aligned magnetic fields slightly decrease the cloud mass-loss rate. Finally, in the transverse field runs, the coarse resolution in T-rad-lr leads to more mass loss than T-rad-hr, but the resolution effects are again smaller than in the hydro runs.

In the top panel of Figure 2.14 we show the effect of resolution on the mixing fraction. As discussed in the previous section, the magnetic pressure in A-rad-hr keeps cloud material within the tail of the cloud. While A-rad-hr follows H-rad-hr at early times, past 5 $t_{\rm cc}$ the mixing fraction for the magnetized case increases to over three times that of the hydro case for both resolutions. The cloud material is kept within dense cloudlets in H-rad-hr and H-rad-lr while in A-rad-hr and A-rad-lr it becomes well mixed with the wind material. While it is clear that an increase in resolution leads to an increase in mixing fraction in both the hydrodynamic and aligned MHD cases, we can qualitatively conclude that the presence of aligned magnetic fields leads to more mixing overall. In contrast, the difference in the mixing fraction between the two transverse field runs is small. This confirms that there is limited mixing in these runs and higher levels of refinement do not reveal more intermediate material.

Finally, the velocity evolution of the radiative clouds across resolutions is shown in the lower panel of Figure 2.14. The two resolutions are consistent with each other over the duration of the simulations for both the hydrodynamic and MHD runs. This further enforces the argument that our resolution of $\Delta x = R_{\rm cloud}/64$ is sufficient.

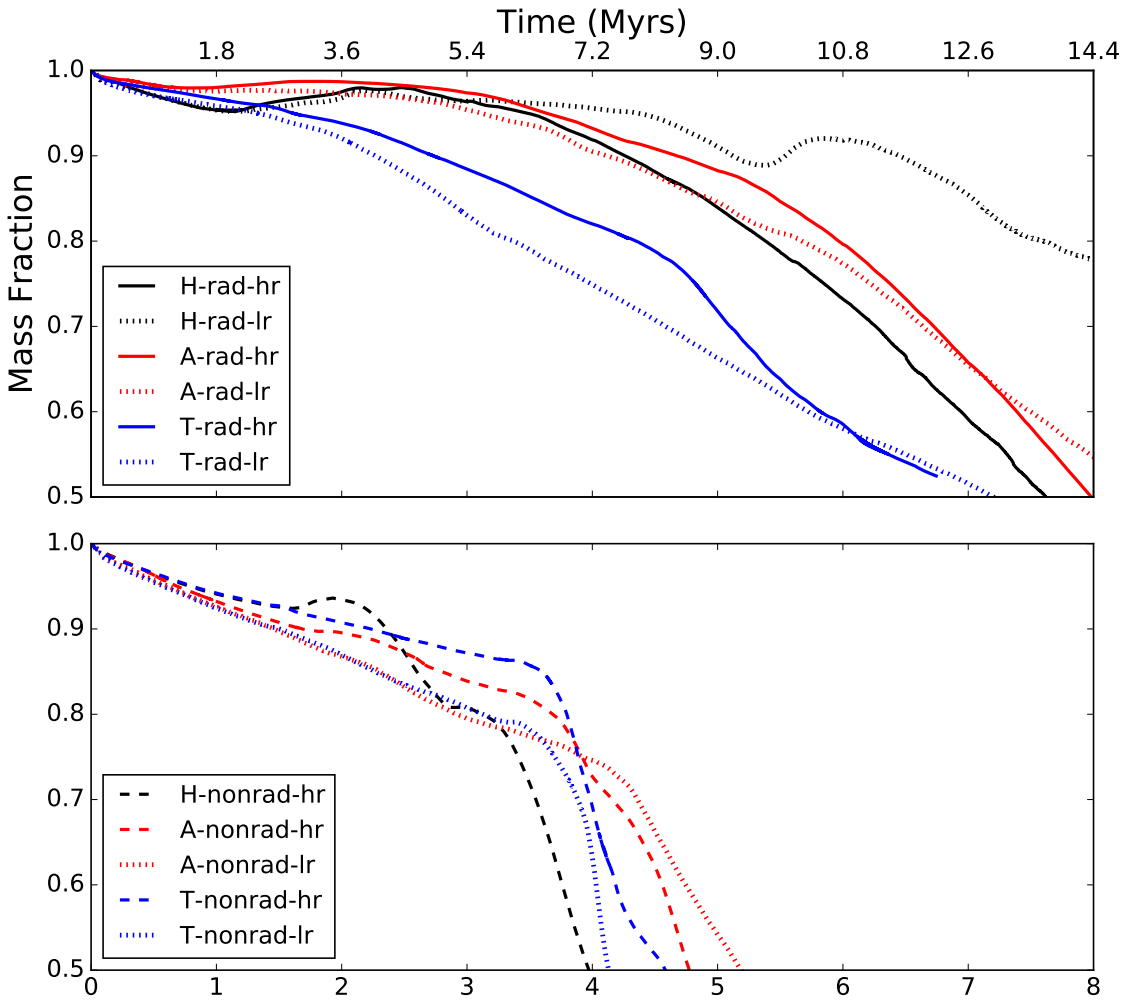

Figure 2.13: Top Panel: Mass fraction of cloud material greater than $\rho_{\rm i,c}/3$ as a function of time in units of cloud crushing times of all runs. The hydrodynamic simulations are shown in black; H-rad-hr as the solid line, H-rad-lr as the dotted line. The aligned and transverse fields follow the same pattern in red and blue, respectively. Bottom Panel: Same as the top panel comparing the high and low resolution runs without radiative cooling, dashed lines are high resolution while dotted lines are low resolution.

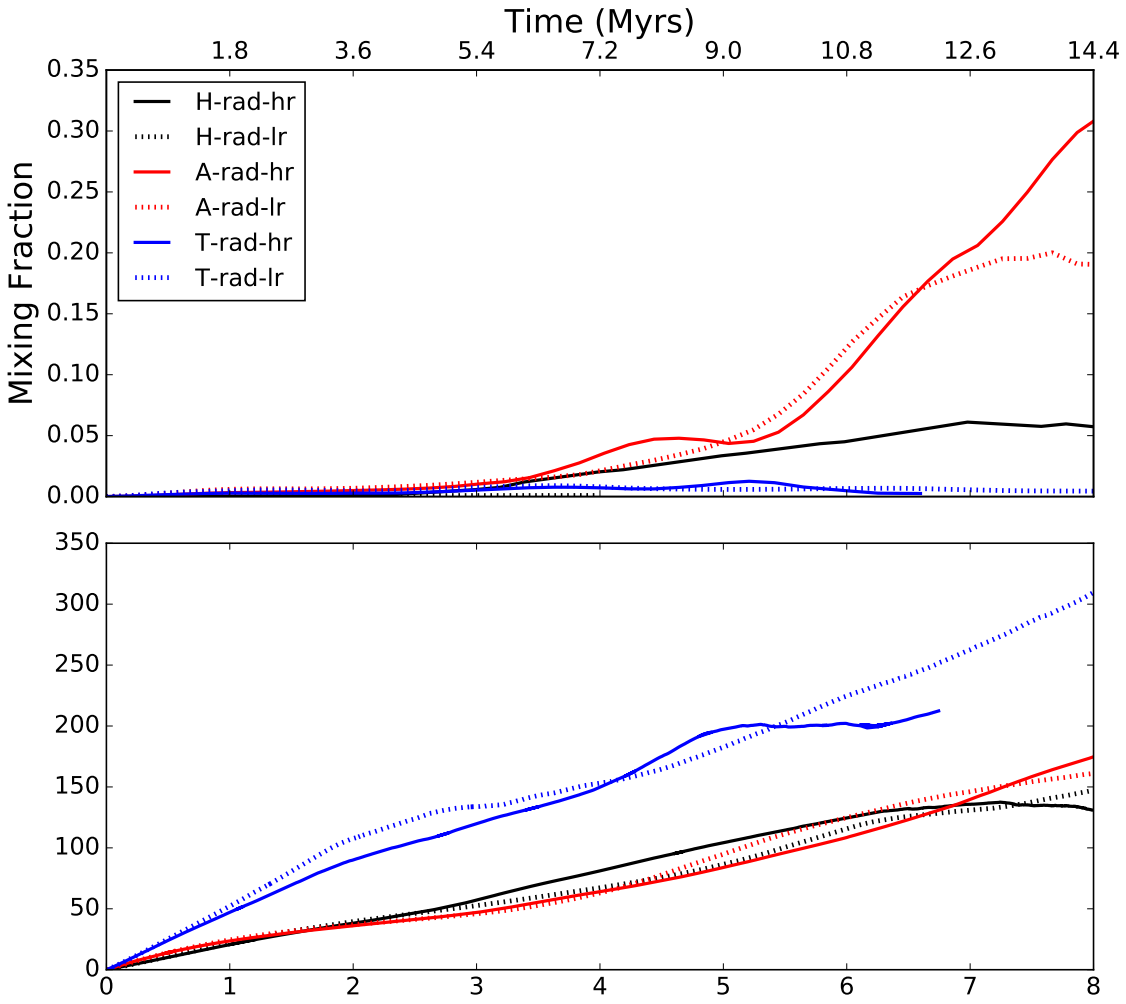

Figure 2.14: Top panel: Fraction of mixed material over time comparing resolutions. Bottom panel: Cloud velocity along the flow of the wind as a function of time in units of cloud crushing times of all runs. The hydrodynamic simulations are shown in black; H-rad-hr as the solid line, H-rad-lr as the dotted line. The aligned and transverse fields follow the same pattern in red and blue, respectively.

In Paper I, we were able to show explicitly that going to a resolution of $\Delta x = R_{\rm cloud}/128$ gives similar results as the $\Delta x = R_{\rm cloud}/64$ simulations for the hydro-only cases, but it is computationally prohibitive to conduct similar simulations for the MHD case, as a single $R_{\rm c}/128$ MHD simulation would require over 100k node-hours on Stampede2 with 68 cores per node. With only two resolutions, it is not possible to conclude that these values converge monotonically. However, the evolution of mass, mixing fraction, and velocity, are much more consistent with each other between $R_{\rm c}/32$ and $R_{\rm c}/64$ than the hydrodynamic runs. This is true for both the non-cooling and radiative simulations, giving us confidence that our results have captured the overall evolution of radiative, magnetized clouds.

On the other hand, the choices for the magnetic field orientations in this work are idealized and do not fully reflect the more complex topologies of astrophysical fields. In reality, magnetic fields in the IGM are random and tangled. These components would likely create an additional stabilizing pressure (see Banda-Barragán *et al.*, 2018) which may ultimately affect the cooling efficiency of the clouds. However, the two choices for field orientations here capture the general cases that will influence realistic configurations. Grønnow *et al.* (2018) and Gronke and Oh (2018, 2019) have shown that condensation can impact the cold gas within the interaction by creating more of the dense gas downwind. With a domain large enough to capture this condensed gas, we may find that the mass flowing around and behind the cloud in the transverse cases is not completely lost sustaining the colder cloud phase in the interaction for longer times.

In addition to the limitations imposed by domain size, our results are subject to numerical effects. While we have chosen our orientations to mitigate the effects, numerical resistivity can result in unphysical magnetic reconnection, particularly where field lines have been bent around the cloud by the wind. As this is a resolution-

dependent effect, the choice of AMR refinement criteria can impact the location and scale of these effects.

Finally, we note that our results are also dependent on the choice of cooling regimes and cooling floor which limit the extent to which gas can cool and condense downwind. Our results are also limited by the exclusion of heating from UV radiation and cosmic rays. These factors may reduce the cloud's ability to cool and form dense cloudlets. Self-contained and turbulent fields as well as a smooth cloud density profile may also lead to different quantitative results. Banda-Barragán *et al.* (2018) have started to explore the effects of turbulence in wind-cloud problems but without radiative cooling. Thus, combining cooling and turbulence should be subject to a follow-up study.

2.4 Summary and Conclusions

We have presented a suite of three-dimensional AMR MHD wind-cloud simulations including radiative cooling and investigated the effect of magnetic fields in two orientations on the disruption and evolution of the wind-cloud interaction. Our conclusions can be summarized as follows:

1. Radiative cooling extends the lifetime of all clouds, regardless of whether or not magnetic fields are present and regardless of their particular orientation.

2. Magnetic fields aligned with the wind protect the cloud from hydrodynamic instabilities, creating a smoother cloud morphology, but they do not provide a substantial increase to the cloud's lifetime or stability over the non-magnetized case. The magnetic pressure resists compression in the tail of the cloud resulting in slightly more diffuse structures with higher mixing fractions after the clouds break up.

3. Clouds embedded in magnetic fields transverse to the wind experience a draping

effect, which does not aid cloud survival if the flow is radiative and can cool. Instead, the amplified and re-oriented magnetic field in the wind pushes the cloud material in the direction perpendicular to the field, leading to higher rates of mass loss.

4. The magnetic draping that occurs with transverse magnetic fields allows magnetic and thermal pressures to reach equipartition. Thus, magnetic draping is an effective acceleration mechanism, as its effect becomes more significant in models with stronger transverse fields.

5. The protection of a $\beta = 1$ envelope prevents the cloud material draped by transverse fields from mixing with the wind, as it is contained in a region of high magnetic pressure that opposes ram pressure. Cooling is ineffective in this envelope and condensation is reduced.

6. An increase in field strength amplifies the effects of transverse fields, pulling the cloud apart at a faster rate. For aligned fields, a stronger field strength results in an increase in cloud lifetime.

7. Magnetic fields inhibit small-scale hydrodynamic instabilities, so the two resolutions of the radiative MHD runs are in better agreement with each other than their hydrodynamic counterparts.

Together these results demonstrate that the influence of magnetic fields has a significant impact on the evolution of wind-cloud interactions. These conclusions are applicable to the hot phase of galactic winds and the general study of the interaction of magnetized clouds and hot winds. It is clear that radiative cooling always contributes to an extension cloud lifetime, however, the combined effects of cooling and magnetic fields do not compound to produce more stable clouds. Instead, magnetic fields can

be prohibitive to the stabilizing effects of radiative cooling. The distinction between these two effects is highly dependent on the orientation of the field with respect to the wind. Our results emphasize the need for studies to account for multiple physical effects simultaneously. Investigating the role of magnetic fields in combination with effects such as turbulence, self-gravity, and anisotropic conduction will improve our understanding of the multiphase nature of outflowing winds.

Chapter 3

COLUMN DENSITY PROFILES OF COLD CLOUDS DRIVEN BY GALACTIC OUTFLOWS

This chapter is reproduced from the version published in 2018 in The Astrophysical Journal, Volume 864, Page 96, with permission from the co-authors.

3.1 Introduction

It has been quite some time since galaxies have been studied as though they were island universes, growing in isolation by accreting material from their surroundings. Instead, it is now clear that the interactions between galaxies and their surrounding media are much more complex, depending on a network of feedback processes that are powered by stars (e.g. Dekel and Silk, 1986; Mac Low and Ferrara, 1999; Scannapieco and Broadhurst, 2001b; Scannapieco *et al.*, 2001; Mori *et al.*, 2002; Scannapieco *et al.*, 2002; Springel and Hernquist, 2003; Dalla Vecchia and Schaye, 2008; Murray *et al.*, 2011; Hopkins *et al.*, 2012; Creasey *et al.*, 2013; Muratov *et al.*, 2015) and active galactic nuclei (e.g. Scannapieco and Oh, 2004; Sijacki *et al.*, 2007; Schaye *et al.*, 2015; Kaviraj *et al.*, 2017). One of the most important of these processes is the exchange of energy and material caused by galactic outflows. These outflows are thought to be driven by star formation and supernovae, (e.g. Heckman *et al.*, 1990; Martin, 1999; Shapley *et al.*, 2003; Martin, 2005; Veilleux *et al.*, 2005) and can have a significant impact on the evolution of the galaxy, star formation rate and metallicities (e.g. Tremonti *et al.*, 2004; Oppenheimer *et al.*, 2010; Davé *et al.*, 2011; Lu *et al.*, 2015; Agertz and Kravtsov, 2015). Observations provide direct information on the multiphase nature of these outflows (e.g. Sturm *et al.*, 2011; Arav *et al.*, 2013; Meiring

et al., 2013; Bolatto *et al.*, 2013; Kacprzak *et al.*, 2014) as well as the composition and dynamics of the circumgalactic medium (CGM) into which they propagate (Keeney *et al.*, 2013; Rubin *et al.*, 2014; Arribas *et al.*, 2014; Werk *et al.*, 2014; Wiseman *et al.*, 2017). However, disentangling the phases of the outflows and understanding their interactions with the environment has proven to be a challenge.

From an analytic perspective, Chevalier and Clegg (1985) derived a solution for a wind being driven from a region of uniform mass and continuous energy input. This model wind accurately describes the hot regions of galactic outflows observed in X-ray emission (McCarthy *et al.*, 1987). However, these types of observations can only be made for nearby galaxies. For more distant objects, observations are limited to absorption measurements of colder gas, seen either in down-the-barrel observations of the host galaxy's background stellar continuum (Chisholm *et al.*, 2018b) or along sightlines through the CGM of starburst galaxies with the background continuum provided by distant quasars (QSOs), (Heckman *et al.*, 2017b; Borthakur *et al.*, 2013). While the two observations can provide information of the ionization and extent of the CGM, both are significantly limited in their ability to understand the dynamics of the outflowing material. One particular anomaly in observations is the detection of absorption from both high ionization energy ions such as O VI at 138 eV and lower energies like Mg II at 15 eV, with a distinct lack of absorption from N V (e.g. Chisholm *et al.*, 2018b). With an ionization energy around 97 eV, it is to be expected that the conditions which produce both O VI and Mg II can also produce N V. This discrepancy has been investigated for non-starbursting galaxies (Werk *et al.*, 2016), but a cause in relation to starbursting galaxies, in particular, is yet to be determined. The number of direct observational predictions has been limited, making it unclear to what extent detailed models of the observational properties of cold clouds driven by galactic outflows can explain these trends.

Specifically, numerical simulations have focused on the nature of the outflowing material and the physics dominating the interaction between winds and cooler clouds. Klein *et al.* (1994) have shown results for hydrodynamical simulations in which clouds within these winds were found to be accelerated and elongated over timescales longer than the time required for the shock to cross the cloud - demonstrating the need for longer simulations to fully understand the cloud evolution. Since then numerical simulations have expanded to investigate cloud-wind interactions from many angles, from studies including thermal conduction and radiative cooling (e.g. Orlando *et al.*, 2005; Schneider and Robertson, 2017), to accounting for non-equilibrium chemistry effects (e.g. Kwak *et al.*, 2011), and to incorporating magnetic fields (e.g. Mac Low *et al.*, 1994; Fragile *et al.*, 2005; McCourt *et al.*, 2015). Even so, these simulations have not covered the full parameter space relevant to galactic outflows and have not yet been directly connected to likely observations.

There have been several attempts to derive absorption line properties from cosmological simulations that include outflows (e.g. Oppenheimer and Davé, 2006; Oppenheimer *et al.*, 2009; Ford *et al.*, 2013; Turner *et al.*, 2016). However, these studies did not look at cold cloud properties within isolated outflows. At the same time, simulations of isolated cloud-wind systems have focused on the hydrodynamic interactions with less attention to the possible connections to observations. In addition, attempts to explain possible models for the spectra and absorption profiles observed fall short of having reliable ways to connect to simulations already performed.

New analytic tools, such as TRIDENT (Hummels *et al.*, 2017), can help bridge the gap between simulations and observations. This can be done by generating synthetic spectra and calculating ion number densities within simulations without the extra computational cost of including a chemistry solver. For this work, we explore the possibility of generating column densities of commonly observed ions from existing

simulations with TRIDENT in order to make comparisons between simulation results and actual outflow observations.

In this paper, we present synthetic column density calculations and velocity profiles of clouds simulated with both radiative cooling and thermal conduction at various evolutionary stages. In Section 3.2 we discuss the simulations used within this study including the parameters and relevant physics. Within Section 3.3 we outline the methods of calculating the column density and velocity profiles as well as the procedure for fitting profiles for each cloud. Section 3.4 includes comparisons across simulation parameters and ion species, with an application of these results to observations in Section 3.5. We conclude with a discussion and motivation for future work in Section 3.6.

3.2 Simulations

We performed a full analysis of the ion densities on the outflow simulations in Scannapieco and Brüggen (2015) and Brüggen and Scannapieco (2016), SB15 and BS16 respectively hereafter. This suite of simulations was carried out with FLASH (version 4.2, Fryxell *et al.*, 2000), a multidimensional hydrodynamics code that solves the fluid equations on a Cartesian grid with a directionally split Piecewise-Parabolic Method (Colella and Woodward, 1984). The simulations were done in three dimensions, as limiting the degrees of freedom can influence the development of shear instabilities. They assumed an initial cloud radius of 100 parsecs, a temperature of 10^4 K, a mass density of $\rho = 10^{-24}$ g cm^{-3}, and a mean atomic mass of $\mu = 0.6$. These parameters result in a total column density of 3.1×10^{21} cm^{-2}. As shown below, this column density determines cloud evolution, rather than the radius and density.

Initially, the cloud was positioned at (0, 0, 0) within the domain covering a physical volume of -800×800 parsec in the x and y directions and -400×800 parsec in the z

direction, which was the direction of the hot outflowing material. The interaction at the z boundary was defined by a condition where the incoming material is added to the grid and given the same values of density, $v_{\rm hot}$, and $c_{\rm s,hot}$ as the initial conditions. For all other boundaries, the FLASH "diode" condition was used, which assumes the gradient normal to the edge of the domain of all variables except pressure to be zero and only lets material flow out of the grid.

3.2.1 Physics of Cloud Evolution

Two important timescales that influence the evolution of a cold cloud embedded within a hot wind are the cloud crushing time, $t_{\rm cc}$, and the cooling time, $t_{\rm cool}$. The cloud crushing time describes the amount of time it would take the initial shock to travel halfway through the cloud and is given by

$$t_{\rm cc} = \frac{R_c}{v_{\rm hot}\chi_0^{1/2}}, \tag{3.1}$$

which, for a constant cloud radius, is dependent only on the velocity of the wind, $v_{\rm hot}$, and the density ratio, χ_0 (e.g. Klein *et al.*, 1994). The cooling time, which determines the time for the cloud to radiate away its thermal energy is given by

$$t_{\rm cool} = \frac{(3/2)n_c k\mathbf{T}}{\Lambda(T)n_{e,c}n_{i,c}}, \tag{3.2}$$

where T is the temperature and $\Lambda(T)$ is the equilibrium cooling function at T with n_c, $n_{e,c}$ and $n_{i,c}$ are the total, electron and ion number densities within the cloud. If the ratio of $t_{\rm cool}/t_{\rm cc} = N_{\rm cool}/(n_{i,c}r_c)$ with $N_{\rm cool} \equiv 3kTvn_v(2\Lambda\chi^{1/2}n_{e,c})^{-1}$ is below one, then cooling will have a significant influence of the evolution of the cloud. Table 1 in SB15 gives values for $N_{\rm cool}$ as calculated using equilibrium cooling cures from Wiersma *et al.*

(2009) assuming solar metallicity and a mean molecular mass of 0.6. With column densities between 10^{17} and 10^{19} cm^{-2}, the resulting ratio between cooling time to cloud crushing time is small. For the range of parameters used, the clouds are able to cool on a timescale much shorter than the timescale for the evolution of the cloud allowing for cooling to influence the cloud before it is disrupted by the shock.

Within the simulations, cooling was computed in the optically thin limit assuming local thermodynamic equilibrium

$$\dot{E}_{\rm cool} = (1 - Y)\left(1 - \frac{Y}{2}\right)\frac{\rho\Lambda(T, Z)}{(\mu m_p)^2}, \tag{3.3}$$

where $\dot{E}_{\rm cool}$ is the radiated energy per unit mass, ρ is the density in the cell, m_p is the proton mass, $Y = 0.24$ is the helium mass fraction, $\mu = 0.6$ the mean atomic mass, and $\Lambda(T, Z)$ is the cooling rate as a function of temperature and metallicity. With the assumption that the abundance ratios of the metals are always solar, the tables compiled by Wiersma *et al.* (2009) were used. Heating by a photoionizing background was not included in the calculations, however, sub-cycling was implemented (Gray and Scannapieco, 2010) along with a cooling floor at $T = 10^4$K.

The fluid equations including thermal conduction and radiative cooling as solved by FLASH are

$$\partial_t \rho + \nabla \cdot (\rho \boldsymbol{u}) = 0, \tag{3.4}$$

$$\rho[\partial_t \boldsymbol{u} + (\boldsymbol{u} \cdot \nabla)\boldsymbol{u}] = -\nabla p, \tag{3.5}$$

$$\partial_t E + \nabla \cdot [E\boldsymbol{u}] = -\nabla \cdot (p\boldsymbol{u}) - n^2\Lambda(T) + \nabla \cdot \boldsymbol{q}, \tag{3.6}$$

with ρ the density, $\boldsymbol{u}$ the velocity, $p = k_B T\rho/(\mu m_p)$ the pressure and $E = p/(\gamma - 1) + \frac{1}{2}\rho|\boldsymbol{u}|^2$ the total energy density, $\Lambda(T)$ is the radiative cooling function and $\boldsymbol{q}$ describes the heat flux due to conduction. We adopt a saturated thermal conduction limit when the mean free path of electrons is much larger than the length scale of the

temperature gradient. This leads to the definition

$$\boldsymbol{q} = \min(\kappa(T)\nabla T, \quad 0.34 n_e k_B T c_{s,e} \nabla T |\nabla T|), \tag{3.7}$$

(Cowie and McKee, 1977), where $\kappa(T) = 5.6 \times 10^{-6} T^{5/2}$ erg s^{-1} K^{-1} cm^{-1} and $c_{s,e} = (k_B T/m_e)^{1/2}$ is the isothermal sound speed of the electrons in the wind with m_e the mass of the electron. It is assumed that electrons and ions have the same temperature. The diffusion equation describing conduction is then solved with the general implicit diffusion solver in FLASH. Saturated thermal conduction was also implemented with the use of a flux limiter that modifies the diffusion coefficient to vary until some maximum flux as determined by the Larsen flux limiter (Morel 2000). In units of cloud crushing times, these equations are invariant under the transformation

$$\mathbf{x} \rightarrow \alpha \mathbf{x}, \qquad \mathbf{t} \rightarrow \alpha \mathbf{t}, \qquad \text{and} \qquad \rho \rightarrow \alpha \rho \tag{3.8}$$

resulting in the evolution of the cloud only depending on the product of the size and density.

3.2.2 Selection of Evolutionary Stages

While the cloud crushing time is a good description of the disruption time for a single cloud, this study compares evolutionary stages across many types of clouds. To compare to $t_{\rm cc}$, another timescale is defined over the course of the cloud's evolution based on the mass fraction of the cloud that is at or above 1/3 of the cloud's original density. The first time, t_{95}, corresponds to the time at which 95% of the cloud is at or above this density. The following three times, t_{75}, t_{50} and t_{25} follow a similar pattern with 75%, 50% and 25% of the cloud. These four stages correspond to the four evolutionary stages we consider while estimating column densities.

3.2.3 Frame Changing and Refinement/Derefinement

In order to follow the disruption of the clouds, it was necessary for the simulations to shift frames as the cloud is accelerated by the wind. To do this SB15 and BS16 implemented an automated frame change routine (see SB15 and BS16 for details). In addition, they used FLASH's default AMR variables of temperature and density with a refinement criterion of 0.8. A secondary refinement condition was enforced to ensure the simulation maintained high resolution in areas important to cloud evolution and to reduce the computational cost of higher refinement in areas of the simulation that have less influence on the cloud evolution. This additional condition imposed derefinement on cells that satisfied one of the following (1) the cell was outside a cylinder along the z axis with a radius equal to three times the initial cloud raids or nine times the current x extent of the cloud or (2) the cell was outside a cylinder centered on the z axis with radius equal to the initial cloud radius or three times the current x extent of the cloud *and* both the distance to the $x - y$ plane and the z center of the cloud were greater than three times the current radius of the cloud.

3.2.4 Parameters

The parameter space for these simulations can be reduced to the wind parameters; $T_{\rm hot}$, $v_{\rm hot}$, and column density of the cloud. According to Chevalier and Clegg (1985), the Mach number depends only on $r/R_\star$ where r is the distance from the outflowing region and $R_\star$ is the driving radius of the flow. This radius reflects the size of the region in which the energy input from sources such as supernovae accelerates the gas. At the edge of this region, the gas becomes supersonic and tends to a constant velocity at further radii. For M82, $R_\star \approx 300$ pc. (McKeith *et al.*, 1995) It follows that the energy and mass input from the wind can be fully described with the velocity

of the hot medium while the Mach number corresponds to sampling the wind as a function of radius. For the Mach numbers considered, assuming $R_\star = 300$ pc, the physical scale of these radii range from 0.3 to 2.9 kpc from the central starburst. For the cloud with a temperature corresponding to the minimum temperature attainable with atomic cooling ($\approx 10^4$ K), the Jeans length for this gas is $\lambda_J \approx 2$ kpc, much larger than the size of the clouds considered, indicating that the clouds must be confined by pressure to keep from expanding. Pressure equilibrium then requires the ratio of the cloud density to the wind density, χ_0, to be equal to the ratio of the temperature of the wind to the temperature of the cloud.

The choices for $T_{\rm hot}$ and $v_{\rm hot}$, as well as the corresponding density contrast and cloud crushing times, for a cloud radius of 100 parsecs, are given Table 3.1 for both the cooling and conduction runs. The Mach number of the hot wind, $M_{\rm hot}$ is also given. The naming scheme of the runs describes Mach number, wind velocity, and wind temperature in order, with suffixes denoting other unique traits of the run. The parameters were chosen to focus on regions outside of the driving radius, $r > R_\star$, with Mach numbers ≥ 1 and provide multiple runs with the same temperatures and velocities to study the impact of changing the Mach number within the hot wind. Also included are runs with both wind and cloud densities 10 times greater than their original counterparts (named with the -hc suffix) and one low conduction run with one-third of the Spitzer value used in all other conduction runs (named with a -lc suffix).

Table 3.1: Simulation parameters - conduction runs end in -c; high column in -hc; low conduction in -lc

Name	$M_{\rm hot}$	$v_{\rm hot}$ (km s^{-1})	$T_{\rm hot}$ (10^6 K)	$T_{\rm hot}$ (keV)	χ_0	$t_{\rm cc}$ (Myr/100pc)
M0.5-v430-T3	0.5	430	30	2.7	3000	12.5
M1-v480-T1	1	480	10	0.86	1000	6.4
M1-v860-T3	1	860	30	3.7	3000	6.2
M1-v1500-T10	1	1500	100	8.6	10000	6.5
M3.8-v1000-T0.3	3.8	1000	3	0.27	300	1.7
M3.5-v1700-T1	3.5	1700	10	0.86	1000	1.8
M3.6-v3000-T3	3.6	3000	30	2.7	3000	1.8
M6.5-v1700-T0.3	6.5	1700	3	0.27	300	1.0
M6.2-v3000-T1	6.2	3000	10	0.86	1000	1.0
M11.4-v3000-T0.3	11.4	3000	3	0.27	300	0.56
M1-v480-T1-c	1	480	10	0.86	1000	6.4
M1-v860-T3-c	1	860	30	3.7	3000	6.2
M1-v1500-T10-c	1	1500	100	8.6	10000	6.5
M3.8-v1000-T0.3-c	3.8	1000	3	0.27	300	1.7
M3.5-v1700-T1-c	3.5	1700	10	0.86	1000	1.8
M3.6-v3000-T3-c	3.6	3000	30	2.7	3000	1.8
M6.5-v1700-T0.3-c	6.5	1700	3	0.27	300	1.0
M11.4-v3000-T0.3-c	11.4	3000	3	0.27	300	0.56
M3.8-v1000-T0.3-hc	3.8	1000	3	0.27	300	1.7
M3.5-v1700-T1-hc	3.5	1700	10	0.86	1000	1.8
M3.6-v3000-T3-hc	3.6	3000	30	2.7	3000	1.8
M6.5-v1700-T0.3-lc	6.5	1700	3	0.27	300	1.0

3.3 Estimation of Observables

3.3.1 Trident Analysis

Our analysis makes use of the TRIDENT analysis tool (Hummels *et al.*, 2017), an extension of the yt analysis code (Turk *et al.*, 2011). TRIDENT is a multifunctional tool created to enable simulated observations of astronomical hydrodynamic simulations. It can be used to create absorption line spectra through simulated datasets as well as column density maps for ion species not originally within the simulation outputs. The full description of the code can be found in Hummels *et al.* (2017). However, a short description of the relevant details is given here.

In order to generate density maps and spectra, TRIDENT first calculates the density of a given ion within the simulated dataset. This is done through the module `ion balance`. The module first determines if the dataset contains a density element for each cell within the domain considered, this may be the entire dataset or a subset representing a sightline as defined by TRIDENT's `LightRay`. If the simulation explicitly tracks the ion's density through a chemistry solver, this density is used. However, for this paper, each ion number density is derived from the gas density and metallicity fields within the dataset and an ionization fraction assuming ionization equilibrium. The final estimation for the number density of the i-th ion of element X becomes

$$n_{X,i} = \boldsymbol{f_H} \frac{\rho}{m_H} Z \left(\frac{n_X}{n_H} \right)_\odot f_{X,i}, \tag{3.9}$$

where ρ and Z are the gas density and metallicity fields, respectively, from the dataset, $\boldsymbol{f_H}$ is the primordial H mass fraction with an adopted value of 0.76, and $Z(\frac{n_X}{n_H})_\odot$ is the solar abundance.

3.3.2 UV Background

The equilibrium ionization fraction, $f_{X,i}$, is a function of temperature, density, and incident radiation, most typically a UV metagalactic background. For use within the `ion balance` module, the ionization fraction is linearly interpolated over a grid of pre-calculated ionization fractions through temperature, density, and redshift. The default UV background for TRIDENT is the Haardt and Madau (2012) metagalactic background. While this is appropriate for approximating the ions within the intergalactic medium, it is not an accurate estimation of the environment around starburst galaxies.

In order to create a new ionization fraction lookup table to integrate with TRIDENT, the shape and intensity of the incident radiation were based on a STARBURST99 model (Leitherer *et al.*, 1999). Here we used the best-fit theoretical model found within Chisholm *et al.* (2018b) from 'down-the-barrel' observations of the outflow in galaxy J1226+2152. Such an orientation allowed for the absorption lines of the CGM to be embedded within the stellar continuum. The best-fit model was found by fitting both the continuum and extinction using a Calzetti extinction law (Calzetti *et al.*, 2000). The STARBURST99 models make use of the Geneva stellar evolution model and varied interstellar continuum metallicities. The best-fit model had a stellar metallicity of 0.2 $Z_{\odot}$ and a light-weighted age of 11 Myr. With the shape of the incident radiation given by the best-fit STARBURST99 model, the strength of the radiation is dependent on the distance from the source, which we infer from the measured ionization parameter in Chisholm *et al.* (2018b), $\log(U) = -2$.

The construction of the table then followed the same procedure as outlined in Smith *et al.* (2008, 2017). Ionization fractions were computed within a grid over temperature, hydrogen number density, and redshift. While redshift was not explicitly

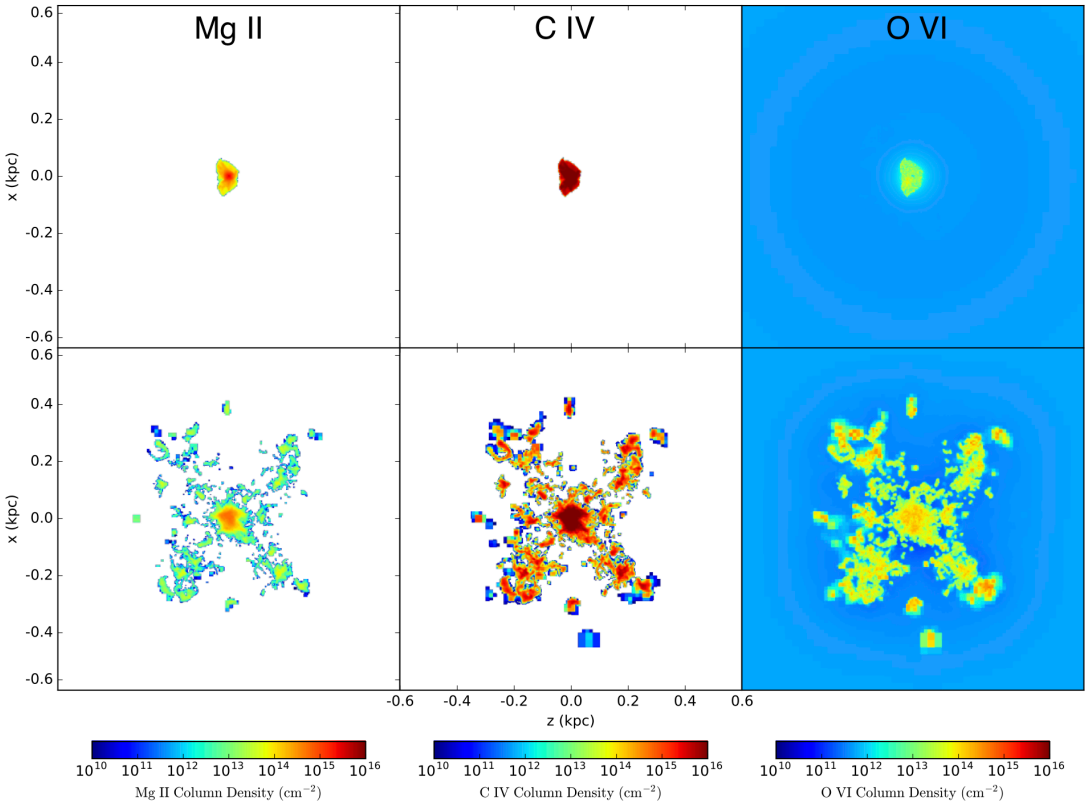

Figure 3.1: Density projections down-the-barrel (through the wind), for Mg II (left), C IV (middle), and O VI(right) at t_{50} for the M3.8-v1000-T0.3 runs. The efficient conduction run is shown in the top panels and inefficient conduction is shown in the bottom panels.

taken into account, these results are applicable to observations with $z \geq 0$ due to the fact this analysis focused on the influence of the dominant starburst background which is redshift independent. The grid was populated with calculations using the photoionization software, CLOUDY (Ferland *et al.*, 2013), which takes the best fit STARBURST99 model as the shape of incident radiation and an ionization parameter of $\log(U) = -2$ (see Chisholm *et al.*, 2018b). These simulations spanned a range of temperatures from 10 to 10^9 K, in step sizes of 0.025 dex, and hydrogen number densities 10^{-9} to 10^4 cm^{-3}, in step sizes of 0.125 dex, to mimic the default table within TRIDENT, and allow for integration with the existing TRIDENT procedure with

little modification. The newly generated table was then loaded in place of the default ionization table and ion number densities were calculated as described above.

With the use of the new table, column density maps can be created as shown in Figure 3.1. These projections are for the M3.8-v1000-T0.3-c and M3.8-v1000-T0.3 runs highlighting the difference in structure between the conduction and cooling runs. While conduction creates dense clouds, runs without conduction are much more diffuse with more coverage. With the inclusion of conduction, higher column densities are possible than those that can result from shock-induced ionization. For these runs, compression by the evaporative flow is most significant at low Mach numbers and low-density contrasts. However, as BS16 notes, evaporative compression influences all runs producing small dense clouds at late times in parallel with the streamwise pressure gradient stretching the clouds into filaments. While the filaments are created in the runs with radiative cooling and inefficient conduction, it is this evaporation that leads to such different morphologies between the two sets of simulations. If conduction is suppressed by factors such as magnetic fields, the radiative cooling runs may lead to clouds more descriptive of the accelerated material in outflows.

The multiphase nature of these outflows can be seen by looking at the average temperature for each ion. In Figure 3.2 the distribution of average temperature across all runs and times for ions of various ionization potentials is shown. Despite the wide range of wind parameters, there is a distinct distribution of temperatures for each ion. It is particularly interesting that the average temperature for O VI and N V are substantially higher than the temperature of the cloud, indicating that these ions are produced in a separate phase than the low and intermediate ionization potential ions such as Mg II and Si IV. These high temperatures imply that the higher ionization potential ions are primarily collisionally ionized within these simulations.

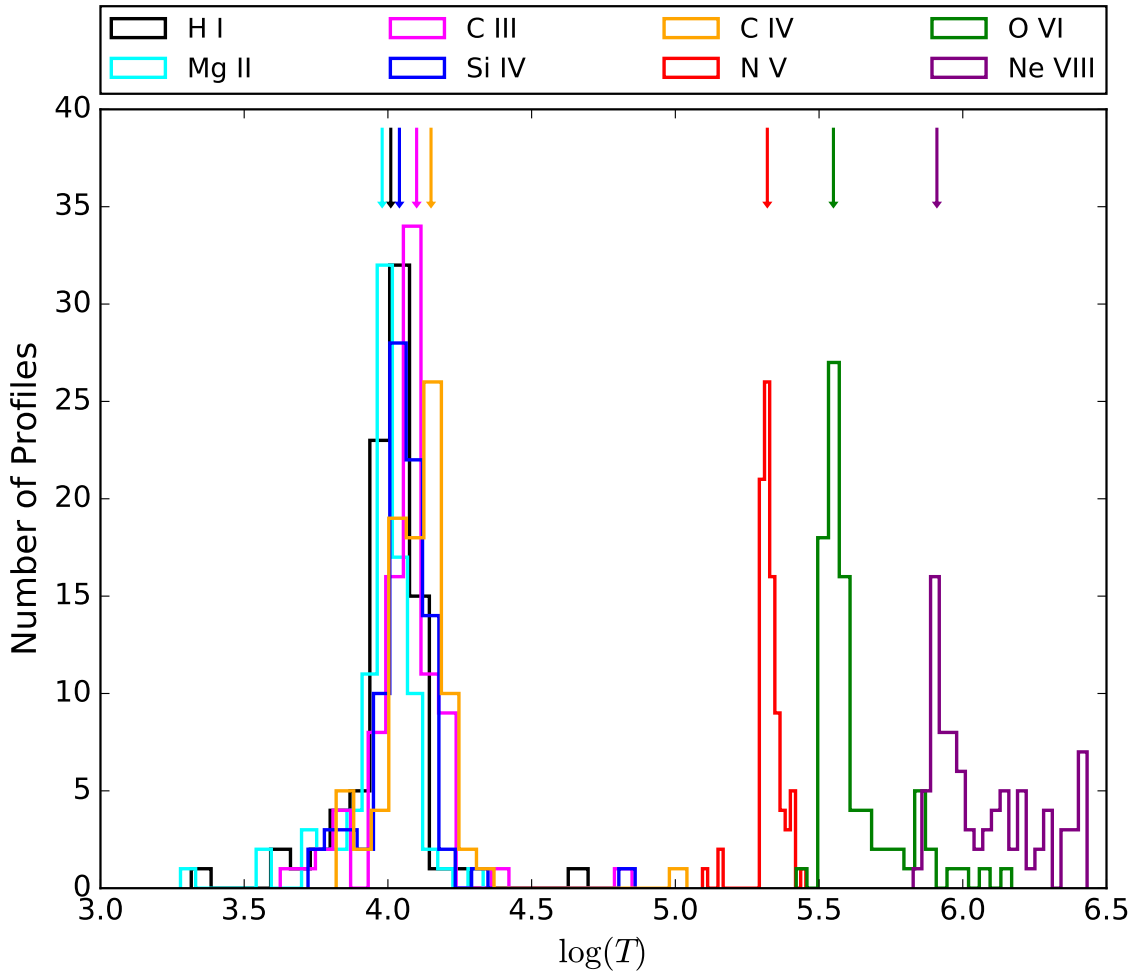

Figure 3.2: The distribution of average temperatures for 8 ions; H I, Mg II, C III, C IV, Si IV, N V, O VI and Ne VIII over all times and runs. An approximate average temperature for each ion is highlighted with an arrow above the distribution.

3.3.3 Column Density Profiles

The column density for each projection along the sightline for each ion at any stage was computed as

$$N = \int_{\text{los}} n_i(z) dz, \tag{3.10}$$

where $n_i(z)$ is the number density of ion, i, and z is the direction of the projection.

We considered a down-the-barrel projection representative of outflows for all runs. Each projection was taken at a fixed resolution of 800 $\times$ 800 cells for the domain

covering 1.6 kpc $\times$ 1.6 kpc, resulting in one pixel per 4 pc^2. At this resolution, the initial cloud area within the simulation covered 0.0314 kpc^2, or 7880 cells. For each cell, we ranked the column densities from lowest to highest and took the top 7880 to give a profile of the column densities that cover a simulation area equal to the initial cloud area. An example of this profile can be seen in Figure 3.3. We determine the profiles can be described by the functional form

$$N(x) = N_0 \frac{0.01}{1.01 - x^q}, \tag{3.11}$$

where x is the fractional rank of each cell expressed as a fraction of the total pixels and N_0 translates to an upper limit on column density for the cloud and q expresses the degree to which the cloud has been compacted. A high q relates to a very compact cloud along the line of sight, while a low q is more descriptive of a diffuse cloud along the line of sight or a consistent column density throughout the entire simulation area considered. This parameter can also be thought of as an analog for coverage, with high q translating to a small amount of coverage with nearly maximum column density and low q describing greater coverage of the sightline containing high column density.

We found the posterior probability distributions of the parameters N_0 and q with an Affine Invariant Markov Chain Monte Carlo Ensemble sampler through the use of the Python package `emcee` developed by Foreman-Mackey *et al.* (2013). With the use of priors, N_0 and q were restricted to values between 0 and twice the maximum column density in the domain and 0 and 100, respectively. The 1σ errors were then derived from the 16 and 84th percentile contours of the posterior.

It is also informative to consider a total average column density. However, as the column density profiles have been cast into a space relating to a fraction of the initial cloud area (x), this average is restricted to considering this specified simulation area rather than the entire cloud. An average column density over a simulation area

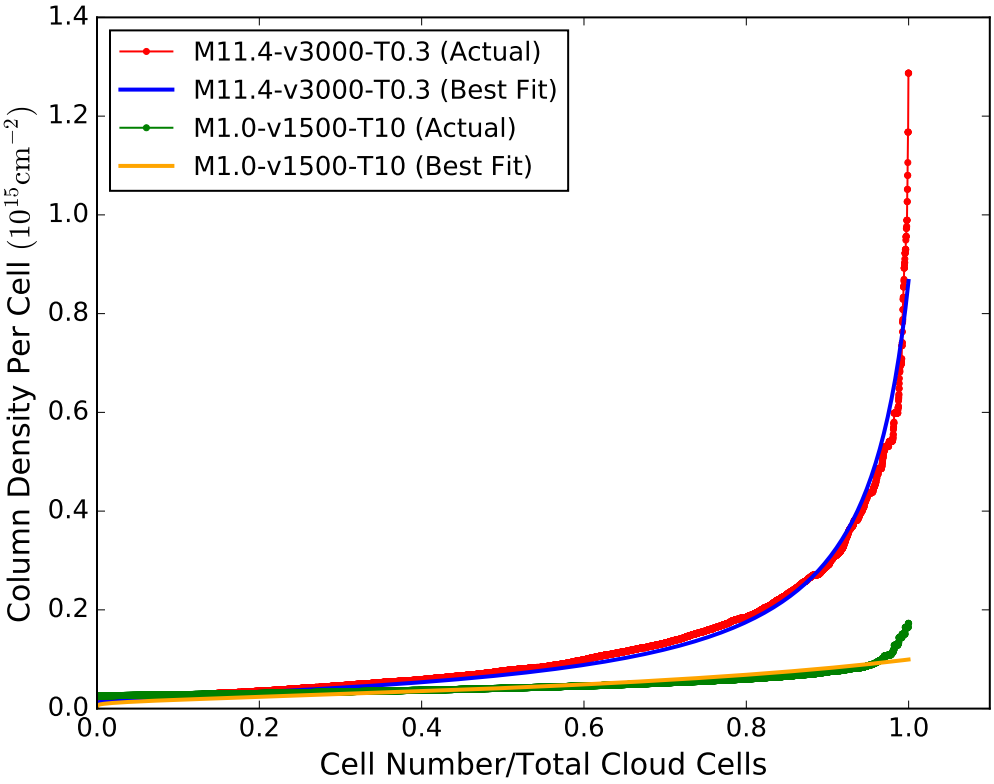

Figure 3.3: Sample of the column density profile with the best-fit line over plotted. Two runs are shown at t_{75} for the ranked column density of O VI; M11.4-v3000-T0.3 (actual in red, best-fit in blue) and M1.0-v1500-T10 (actual in green, best-fit in yellow). The best-fit overplotted is the functional form of equation (3.11) with the best-fit parameters $N_0 = 8.68 \times 10^{14}$ cm^{-2} and $q = 0.18$ for the M11.4-v3000-T0.3 run and $N_0 = 9.94 \times 10^{13}$ cm^{-2} and $q = 0.02$ for the M1.0-v1500-T10 run.

equal to the size of the initial cloud area was therefore calculated as a proxy for total average column density. This was determined numerically from the best-fit model profile as

$$N_{\text{total}} = \int_0^1 N_0 \frac{0.01}{1.01 - x^q} dx. \tag{3.12}$$

The column density of a portion of the cloud can be found in a similar way, changing the limits of integration to reflect the portion of the cloud considered. The column density of the densest half of the cloud corresponds to the value of the integral above with limits from 0.5 to 1. The average column density, along with the best-fit param-

eters and the corresponding errors, was stored in a lookup table.

The average velocity of each ion was also calculated as well as an estimate of the width of an approximate Gaussian profile, or b parameter, including both the thermal velocity spread (b_t) and contribution of Doppler broadening (b_d). The average velocity, weighted by the ion number density was calculated as

$$\bar{v_i} = \frac{\int n_i(x,y,z)v(x)dV}{\int n_i(x,y,z)dV}. \tag{3.13}$$

Again, with x the direction along the line-of-sight. The b parameter was estimated to be the average of the b calculated for all sightlines for the given projection, expressed as $b = \left\langle \sqrt{b_t^2 + b_d^2} \right\rangle$, with

$$b_t^2 = \frac{\int \frac{2k_bT(x,y,z)}{\mu_i m_p} n_i(x,y,z)dx}{\int n_i(x,y,z)dx} \tag{3.14}$$

and

$$b_d^2 = \frac{\int (v(x) - \bar{v_i})^2 n_i(x,y,z)dx}{\int n_i(x,y,z)dx}. \tag{3.15}$$

Here $T(x,y,z)$ is the temperature of the gas and μ_i, the mass number of the ion and m_p, the mass of a proton, with all other constants defined in the usual form. The values for $\bar{v_i}$ and b are stored within the table of best-fit parameters.

This table is created for 10 different ions including low ionization energies prevalent within the cool cloud material such as H I and Mg II through intermediate energies, Si III, Si IV, C II, C III, C IV, and N V to those at the high end, O VI and Ne VIII. These best-fit parameters and the associated errors are quoted in 10 digital tables, one for each ion considered. Table 3.2 represents a sample of these tables. The full tables are available online [1].

[1] www.public.asu.edu/ $\sim$ jcottle1/coldensprofiles.html

Table 3.2: Sample of table of best fit parameters q and τ – C IV

Run	Velocity (km/s)	b (km/s)	N_0 (cm^{-2})	q Fit	Avg N (cm^{-2})	Avg N Err
M3.8-v1000-T0.3-c	22	971	2.81e17	1.925	8.58e15	7.4e6
M3.8-v1000-T0.3-c	36	912	1.14e17	0.725	6.50e15	2.321e7
M3.8-v1000-T0.3-c	61	869	1.09e17	1.099	4.73e15	2.46e7
M3.8-v1000-T0.3-c	110	777	3.72e16	0.517	2.66e15	2.8e6
M3.6-v3000-T3-c	21	62	1.53e16	0.019	7.18e15	3.632e6
M3.6-v3000-T3-c	14	36	7.31e17	6.007	1.25e16	3.82e7
M3.6-v3000-T3-c	43	80	1.61e17	1.155	6.76e15	4.00e7
M3.6-v3000-T3-c	39	73	1.18e18	14.060	1.54e16	1.84e8
M3.5-v1700-T1-c	13	118	2.19e16	0.037	7.62e15	2.74e6
M3.5-v1700-T1-c	21	116	1.18e17	0.613	7.54e15	7.33e7
M3.5-v1700-T1-c	27	143	5.67e17	6.032	9.69e15	3.11e7
M3.5-v1700-T1-c	36	107	3.82e17	6.894	6.21e15	6.473e3
M3.8-v1000-T0.3	108	787	4.29e16	0.220	5.39e15	2.07e7
M3.8-v1000-T0.3	143	679	4.05e+16	0.245	4.75e15	1.46e7
M3.8-v1000-T0.3	158	637	3.31e16	0.205	4.35e15	1.89e7
M3.8-v1000-T0.3	204	613	9.62e15	0.065	2.51e15	2.93e7
⋮	⋮	⋮	⋮	⋮	⋮	⋮

3.4 Results

The distribution of the best-fit parameters, N_0 and q, for the down-the-barrel projections are shown in Figures 3.4 and 3.5. Of the 10 ions, 8 are shown, excluding C II and Si III which are useful for connections to observations but show little to no variation from the distributions seen with C III. Within both figures, the best-fit parameters for all four times of each run are plotted. The colors are indicative of either the Mach number (Figure 3.4) or wind velocity (Figure 3.5). While these two parameters are related, they affect the results somewhat differently and are the most informative of the simulation parameters. There is no trend with wind temperature. Inefficient conduction runs are denoted with circular markers while runs with conduction are denoted with triangular markers. Trends with increasing Mach number (Fig. 3.4) and wind velocity (Fig. 3.5) for these subsets are shown with magenta (cooling) and cyan (conduction) arrows. A limiting observable column density can be estimated with the equivalent width, $W = N\lambda f$, where we assume a SNR of 10 and a velocity width of 100 km/s. For a detection at 3 σ these column densities range between $\log_{10}(N) \approx 12$ for ions such as H I and C IV to $\log_{10}(N) \approx 15$ for Mg II and Si III. They are listed in Table 3.3. The best-fit column densities are well above these limits for most ions. However, for the ions where the fits are in the neighborhood of the observation limits, Mg II, N V, O VI, and Ne VIII, dashed lines have been included in Figures 3.4 and 3.5 for reference.

3.4.1 Conduction vs. Cooling

Most notably, a majority of the conduction runs span a distinctly different portion of parameter space than the low Mach number runs without conduction. In particular, for low ionization ions such as Mg II, C III, C IV, and Si IV the runs with inefficient

Table 3.3: Estimated limiting column densities for a 3σ detection with a SNR of 10

Ion	$\log_{10} N$
H 1	12.38
Mg 2	15.206
C 2	12.88
Si 3	14.66
Si 4	12.59
C 3	12.11
C 4	12.72
N 5	13.107
O 6	12.87
Ne 8	12.99

conduction span a lower range of q values than the conduction runs, as demonstrated by the much shorter lengths of cyan arrows for these ions as opposed to the magenta arrows. As low q corresponds to little compaction or high coverage, it is seen clearly here that the cloud material, where much of these ions originate is sparse and diffuse for the runs with inefficient conduction. Additionally, for the lower ions, the values for N_0 for the inefficient conduction runs tend to be lower than the runs with efficient conduction at low and mid Mach numbers.

For higher ionization ions, O VI and N V, the distinction between cooling and conduction runs is seen in the q parameter. High values of q, corresponding to very compact clouds or little coverage, are dominated by the conduction runs while the runs with inefficient conduction stay within the diffuse cloud regime. If these ions are primarily produced on the boundary of the cloud, as is implied by the fact these ions trace higher temperatures than the core of the cloud (Figure 3.2), the q parameter for

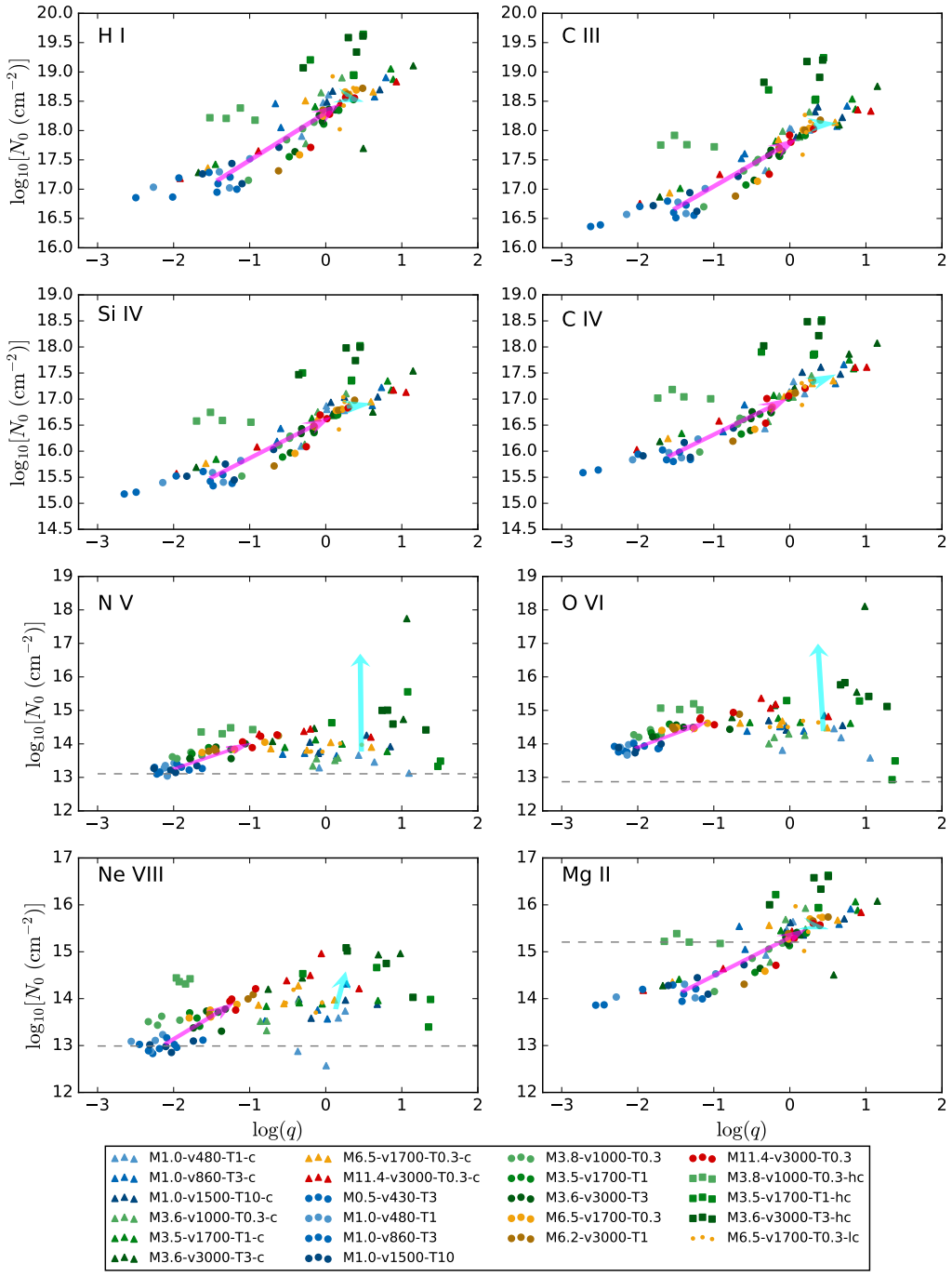

Figure 3.4: Distribution of N_0 and q parameters in log space for all runs and 8 ions. Runs are color-coded by Mach number with the lowest Mach numbers being in shades of blue and the highest Mach numbers in shades of red. Cooling and conduction runs are marked by circle and triangle points, respectively. Also shown are the high column density runs (squares) and the low conduction run (small dots). Arrows (magenta for cooling and cyan for conduction) are overlaid to highlight the trends discussed in Sections 4.1 and 4.2. Dashed lines indicate observational limits on column densities.

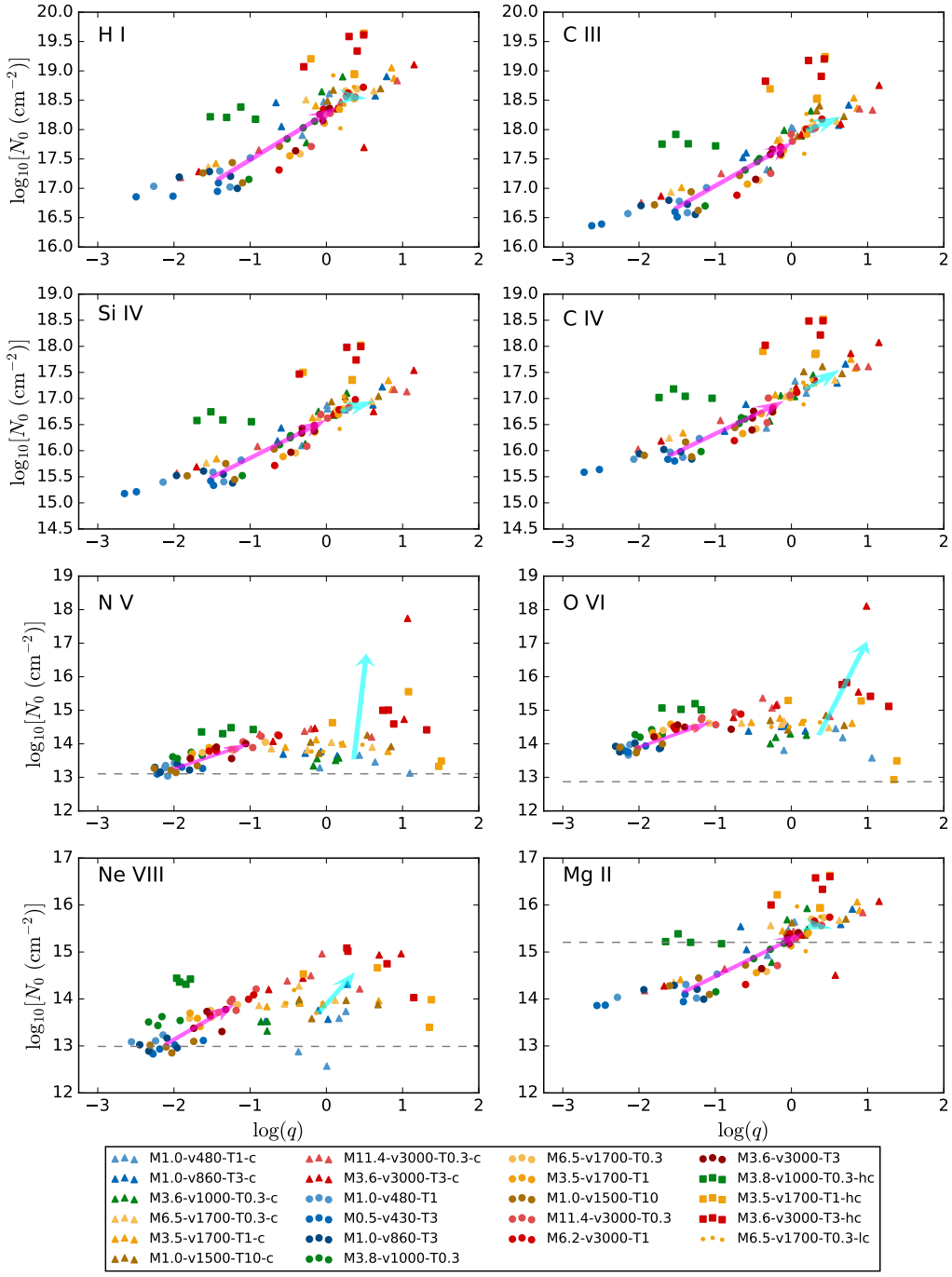

Figure 3.5: Distribution of N_0 and q parameters in log space for all runs and 8 ions. Runs are color-coded by wind velocity with the lowest velocities in shades of blue and the highest velocities in shades of red. Similar to Figure 3.4, cooling and conduction runs are marked by circle and triangle points, respectively. Also shown are the high column density runs (squares) and the low conduction run (small dots). Arrows (magenta for cooling and cyan for conduction) are overlaid to highlight the trends discussed in Sections 4.1 and 4.2. Dashed lines indicate observational limits on column densities.

these ions reflects the thickness of these boundaries where these intermediate ions are produced. The cooling and conduction runs have ranges for the maximum column density that are consistent with each other. Cooling runs with high velocities appear to have comparable maximum column densities to the conduction runs. It appears that conduction does not significantly influence the amount produced of these ions but may in general produce smaller amounts of coverage.

For the highest ionization energy, Ne VIII, there is even more defined clustering between the cooling and conduction runs, primarily dictated by the q parameter. Cooling runs tend toward low q fits while conduction runs exist on the higher end of the q parameter but span a similar range of N_0. For runs with inefficient conduction, the Ne VIII column density is more dependent on the Mach number while for the conduction runs, the larger column densities correlate with higher velocities.

3.4.2 Mach Number and Velocity

As seen most clearly in Figure 3.4, the Mach number of the wind has a strong influence on the column density profile. Consistently for all ions, the lowest Mach numbers result in the least compact and lowest density profiles, and the highest Mach numbers resulting in the most compact clouds. While it is the tendency for high Mach numbers to compress the cloud, which would result in a higher maximum column density, this trend is mostly seen in the runs with inefficient conduction. For the conduction runs, the higher Mach numbers do not influence N_0. This is especially apparent when considering that the Mach number trend arrows for conduction do not follow the data as closely as the cooling trend arrows. This is due to conduction runs producing a dense, thin, filament along the flow of the wind which becomes thinner and more extended as the Mach number increases. This is not seen for the runs with inefficient conduction because high Mach numbers produce similar cloudlets to low

Mach numbers, but with higher densities.

This compression of the cloud due to higher Mach number winds strongly influences the runs with inefficient conduction. It is most evident in the panels for N V and O VI. Here there is little change in the amount of each ion produced, as the N_0 has little variation. However, the best fits for q follow a trend from low to high with increasing Mach number - within the cooling simulations. The compression of the conduction runs is much less dependent on Mach number as the lowest Mach number runs (blue) do not produce notably different best-fit parameters than other Mach numbers. The cooling runs that produce the highest N_0 and lowest q have moderate Mach numbers, between 3 and 4 (shown in green). This degeneracy is likely due to the fact that the compression for the cooling runs is less significant at higher Mach numbers, allowing for clouds to develop a dense outer layer but an interior with a lower density, ultimately reducing the overall column densities.

The dependence of parameters on velocity is shown in Figure 3.5. Here there is a similar trend to the low Mach numbers, where low velocities (those below 1000 km/s) produce the lowest of the fits for N_0 and q. The highest velocities result in the maximum N_0 for both cooling and conduction and the trend arrows for both efficient and inefficient conduction appear to follow the general shape of the data. High velocities also correspond to high q values, reflecting the effects of shocks on both the cloudlets within a cooling run and the filaments in the conduction runs to compress the gas.

3.5 Application: Down-the-Barrel Outflow Observations

As an illustration of the types of studies enabled by our results, we consider an application of our tabulated fits. We consider the observations in Chisholm *et al.* (2018b) in particular as many of our assumptions, including radiation background and ioniza-

tion parameter, are derived from these observations. Chisholm *et al.* (2018b) report absorption profiles from down-the-barrel observations, of a lensed galaxy with $z \approx 2.9$. Observations are made of both low and high ionization profiles that indicate the two phases are co-spatial, much like the wind-cloud interaction considered here. We aim to determine an appropriate scaling of our column density profiles by accounting for two factors that can influence the optical depth of the absorbing clouds.

To approximate an absorption profile for these ions we estimate the observed optical depth for a particular ion as

$$\tau(v) = \frac{c\sigma}{\sqrt{\pi}b} \exp\left[-\frac{(v - v_0)^2}{b^2}\right] \bar{N}, \tag{3.16}$$

where $\bar{N} \equiv \frac{\sum_i^x N_i}{x}$, is the average number density of the ion, where x is the number of points within the column density profile and N_i the column density for the ith point. Here τ is approximated with the center of the absorption profile at the average velocity of the cloud, v_0, with a velocity dispersion determined by the b parameter estimated for each ion and v is the velocity bin within the absorption profile. We consider velocities between -600 km/s to 200 km/s offset from line center. This average optical depth approximates a single cloud.

There are then two ways to parameterize the absorption profile, and we consider the two parameters independently. The first method is the covering fraction which describes the fraction of the area within the sightline that is obscured by the cloud. With this covering fraction parameter, the observed flux from the derived column density profiles can be expressed as

$$F(v) = (1 - f) + fe^{-\tau(v)}, \tag{3.17}$$

where $\tau(v)$ is the average optical depth above and f is the free parameter describing the covering fraction.

The second way to parameterize the absorption profile considers scaling the optical depth either to represent multiple clouds along the sightline or one cloud with scaled density. For this, we assume the intervening cloud has the average optical depth of a single cloud from Equation 3.16, which is then scaled by the parameter α which describes the number of clouds within the sightline or the scaling factor of the density for a single cloud. In this case, the observed flux can be described as

$$F(v) = e^{-\alpha\tau(v)}, \tag{3.18}$$

where $\tau(v)$ is again the average optical depth above and α is the second free parameter we consider, describing the number of clouds.

Best-fit covering fraction and α are found by performing χ^2 minimizations for each of the parameters independently over the five ions shared between our analysis of the Chisholm *et al.* (2018b) observations, C II, C IV, Si IV, O VI and N V. We determine this χ^2 for each of the four evolutionary stages, which here correspond to a central velocity, for all of the 22 runs. As each of these stages could be observed in a single observation when looking down the barrel of an outflow, we consider the average and maximum χ^2 between these stages to determine the goodness of fit for each simulation.

The best fit for both approaches, each with its own free parameter, is shown in Figure 3.6, with the covering fraction fits in red and the multi-cloud fits in blue. Also shown with dashed lines are the $\alpha = 1$ and $f = 1$ cases, highlighting the profiles produced with the base case of one cloud with full coverage over the sightline. The run with the best fit for the covering fraction case is M3.5-v1700-T1-c with a covering fraction of 0.621. The covering fraction approach is able to generate profiles that approximate the nearly saturated lines Si IV and C IV, and maintain the low levels of N V to match observations in Chisholm *et al.* (2018b). However, there is not enough

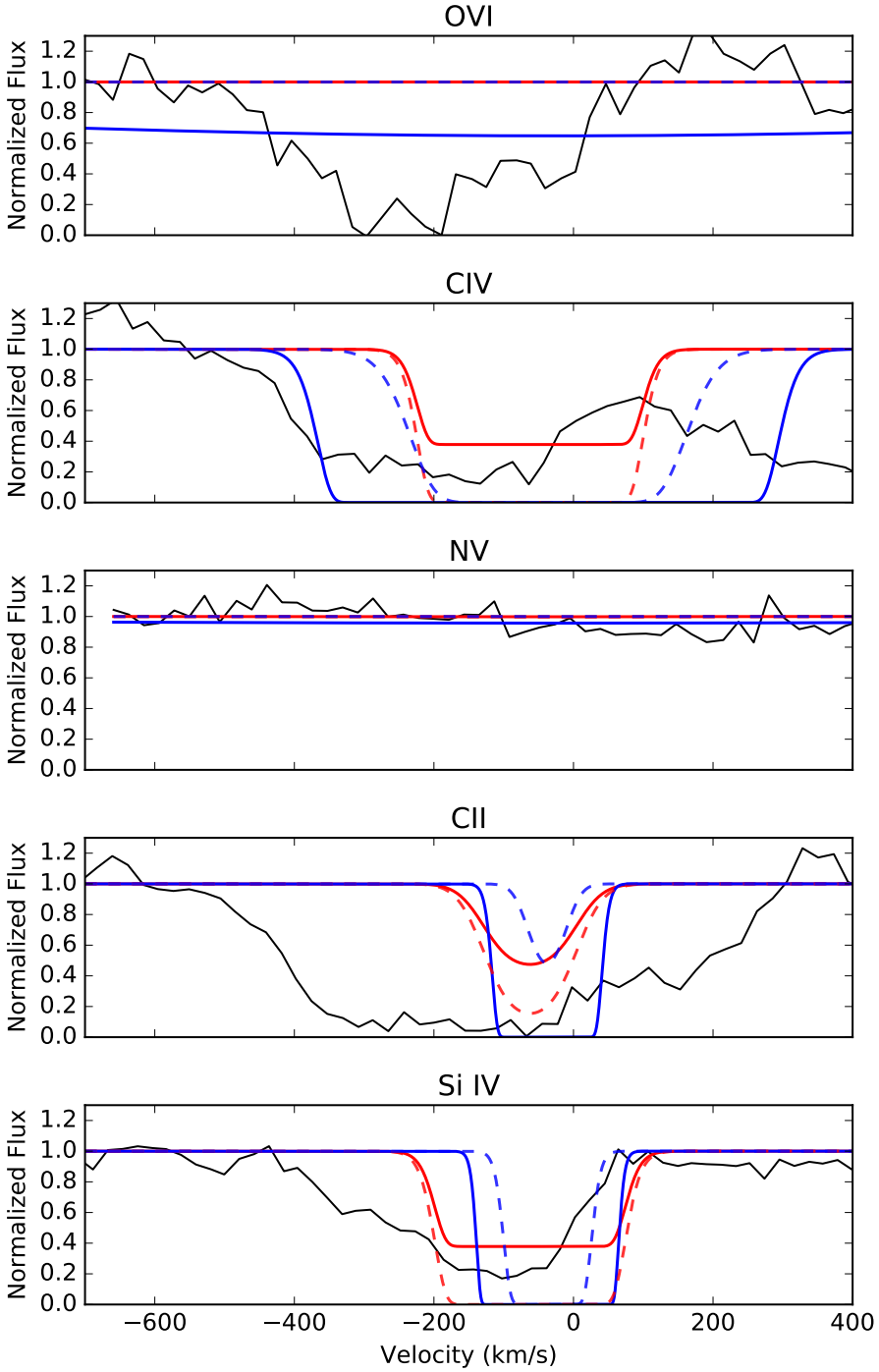

Figure 3.6: The best fit absorption profiles to the Chisholm *et al.* (2018b) observations (shown in black) for the multi-cloud (blue) and covering fraction (red) cases shown for one characteristic time, t_{25}. The covering fraction best-fits correspond to the run M3.5-v1700-T1. The multi-cloud best-fits correspond to the run M3.6-v3000-T3-hc. Also shown in dashed lines are the profiles with $\alpha = 1$ (blue dashed) and $f = 1$ (red dashed) for the same runs.

Table 3.4: Best fit N_0 and q for high resolution run at each stage

	M3.5-v1700-T1	M3.5-v1700-T1-highres
q_1	-1.756	-1.804
q_2	-1.820	-2.097
q_3	-1.583	-1.848
q_4	-1.272	–
$\log(N_{0,1})$	14.208	14.040
$\log(N_{0,2})$	14.328	14.165
$\log(N_{0,3})$	14.588	14.275
$\log(N_{0,4})$	14.490	–

C II or O VI in our simulations to reproduce the observed profiles with a single cloud.

In the case in which the optical depth is increased uniformly, parameterized by the number of clouds, we find a best-fit α of 488 for the best-fit run M3.6-v3000-T3-hc. It is important to acknowledge that it is highly unlikely that 488 clouds would be lined up to each fully cover a particular sightline, though scaling the density of one cloud by this factor is feasible. However, this number, paired with the fact that this best-fit run is one of the high column density runs, demonstrates that there is a significant discrepancy between these simulations and the observations. In particular, our simulations do not produce enough C II. While Si IV and C IV are saturated in the base case and more clouds only widen the profile, the low levels of C II drive up the number of clouds necessary in order to approach the nearly saturated C II observations.

For the intermediate ions, Si IV, C IV and C II it is also clear that the derived line widths are much narrower than those observed in Chisholm *et al.* (2018b). This limits the simulations' potential to produce these wide profiles by simply altering the

optical depth. However, for O VI, there is an opposite effect. While most of the high column density O VI is found on the interface of the cloud, there is a portion of O VI that can be found in the hot wind (see Figures 3.1 and 3.2). This gives O VI velocity dispersions on the order of the wind velocity, 10^3 km/s. This can account for the nearly flat appearance of the best-fit for the multiple cloud approach in O VI. The shallow and wide profile appears flat over the range of velocities relevant to the other ions. Even so, there is not enough O VI within or on the interfaces of the slower moving cloud to reproduce the deep profiles observed. It is possible that this discrepancy could be explained by the effects of low resolution. However, Table 3.4 shows the best-fit parameters for O VI in a higher resolution cooling run which would be most affected by resolution effects due to the fact O VI is produced within mixing layers. The higher resolution run produces comparable maximum column densities and similar coverage parameters, q, to the run with the resolution used throughout the rest of the simulations.

Ultimately, a more realistic view would treat both of these factors together, introducing the influence of a density scaling or multiple clouds each with its own covering fraction. However, even this basic approach supports the need for further investigation. While comparable amounts of Si IV and C IV absorption can be recreated, the lack of C II indicates there is a significant factor not accounted for that enables more cold cloud material to remain within the sightline throughout the interaction with the wind. The wide velocity dispersions of O VI also indicate a need to determine a source of O VI ionization that can introduce noticeable absorption over a smaller velocity range.

3.6 Discussion and Summary

Starburst-driven galactic outflows are a complex, multiphase phenomenon, and understanding their evolution requires close comparisons between observations and numerical studies. While numerical simulations can reproduce the full evolution of cold clouds interacting with hot wind material given a set of assumptions about the underlying physical processes, observations are often limited to absorption line profiles of species with low and intermediate ionization states.

To help in interpreting such observations, we have derived equilibrium column density profiles, average velocities, and b parameters for 22 hydrodynamical simulations of cold, atomic clouds in super-sonic winds including both radiative cooling and thermal conduction. These capture the equilibrium distributions of ten widely-observed ions: H I, Mg II, C II, C III, C IV, Si III, Si IV, N V, O VI, and Ne VIII. With the possible exception of H I, the column density profiles are all well fit by the functional form $N(x) = N_0 \frac{0.01}{1.01 - x^q}$, where x is the fractional rank of each cell expressed as a fraction of the total, N_0 places a upper limit on column density and q expresses the degree to which the cloud has been compacted. For all ions we provide tabulated fits of N_0 and q for each simulation case, at four characteristic times.

As a general trend, the runs including conduction produce much higher column densities and much narrower amounts of coverage, coinciding with the more compact, dense filaments produced in the late stages of the cloud-wind interaction. The runs with inefficient conduction are restricted to lower column densities for most ions except N V and O VI, which are primarily produced at the cloud-wind boundary. These runs also follow more predictable trends with functions of wind velocity and Mach number as higher velocities compact the cloud and result in higher column densities.

Our study is limited by the need to reduce the parameter space with the assumption that the metallicity is solar. While this is an estimate of the maximum metallicity within the CGM, the absorption observed near starbursts is more likely due to high amounts of ion ionization rather than a high metal content. We also assume a radiation model representative of a young starburst galaxy with a high ionization parameter ($\log U = -2$), which can greatly vary between CGM observations and is a necessary component to making connections to CGM observations such as COS-Burst.

However, even in comparison to observations that best match our assumed parameters, we find that we cannot reproduce observed absorption line column density ratios with our equilibrium model. Our results overestimate the amounts of intermediate ions such as Si IV and C IV, as they produce saturated profiles. Due to this, the best fit parameters that produce fits that closely match the profiles for Si IV and C IV also significantly underestimate the absorption from O VI, N V and C II. The discrepancy between O VI and N V absorption is also not explained by the inclusion of thermal conduction. In both cases, inefficient and efficient conduction, the column densities of both ions are comparable and not impacted by resolution effects. Thus it is possible that the lack of N V observed is linked to non-equilibrium processes, (e.g. Grassi *et al.*, 2014; Gray *et al.*, 2015; Gray and Scannapieco, 2016, 2017; Pallottini *et al.*, 2017), which must be accounted for through the use of a full chemical network.

Addressing this issue will require performing a similar analysis on outflow simulations including non-equilibrium chemistry. These can then be compared with the present fits to demonstrate the drawbacks of equilibrium assumption, and they will yield better estimates of the abundances of each ion. Other consideration should be given to the effects of different ionization parameters and metallicities that are more descriptive of the CGM, as well as the balance between cooling and potential photo-

heating. These parameters are likely to have a significant effect on the production of low ions in particular. Similarly, simulations including other effects such as magnetic fields and cosmic rays (e.g. Simpson *et al.*, 2016; Ruszkowski *et al.*, 2017; Fujita and Mac Low, 2018; Samui *et al.*, 2018), as well as addressing the contribution of cold gas created in the expanding wind (e.g. Thompson *et al.*, 2016; Scannapieco, 2017; Schneider *et al.*, 2018) will likely be needed to fully address the parameter space of physical process impacting galactic outflows, their interaction with the CGM, and their influence on galaxy evolution.

Chapter 4

NON-EQUILIBRIUM CHEMISTRY COLUMN DENSITY PROFILES OF COLD CLOUDS DRIVEN BY GALACTIC OUTFLOWS

4.1 Introduction

Wind-swept clouds play a significant role in the interaction between galaxies and their environments, as dense clouds are accelerated past the limits of the galactic plane. Driven by star formation and supernovae, these winds play a significant role in the transportation of material through the circumgalactic medium (CGM) and observations have shown their impact on star formation and galactic evolution. (e.g. Tremonti *et al.*, 2004; Oppenheimer *et al.*, 2010; Davé *et al.*, 2011; Lu *et al.*, 2015; Agertz and Kravtsov, 2015). Though their multiphase nature has been established (e.g. Veilleux *et al.*, 2005; Sturm *et al.*, 2011; Meiring *et al.*, 2013; Bolatto *et al.*, 2013; Kacprzak *et al.*, 2014; Rubin *et al.*, 2014), the processes driving the creation and maintenance of these phases is still unclear.

The hydrodynamics of wind-cloud systems has been studied theoretically for many years. Most notably the analytic solutions derived by Chevalier and Clegg (1985) for a wind being driven by a uniform mass and continuous energy input have been accurate in describing observed sources of X-ray emission (McCarthy *et al.*, 1987) known to come from the regions of hot gas within galactic outflows. These observations are limited to nearby galaxies, causing observations of more distant galaxies to only consist of absorption measurements. Such observations have been made by studying the CGM along the sightline of distant quasars (Keeney *et al.*, 2013; Borthakur *et al.*, 2013; Heckman *et al.*, 2017a; Wilde *et al.*, 2019; Ng *et al.*, 2019) as well as along

the direction of an outflow within the spectra of the host starburst galaxy, known as down-the-barrel observations (Muzahid *et al.*, 2015; Barger *et al.*, 2016; Chisholm *et al.*, 2018a).

Our understanding of the disruption and evolution of the two phases has grown with the use of numerical simulations. Klein *et al.* (1994) first simulated the interaction between a cold cloud and hot wind, establishing a timescale for evolution longer than the time required for the initial shock to pass over the cloud. Though the cloud was not rapidly destroyed, more hydrodynamics-only simulations (e.g. Poludnenko *et al.*, 2002; Pittard *et al.*, 2009; Fragile *et al.*, 2005; Banda-Barragán *et al.*, 2019) demonstrated the need to consider stabilizing effects to produce accelerations and lifetimes of clouds consistent with the observed material within outflows. Numerical simulations of wind-cloud interactions have since been expanded to include the effects of radiative cooling and thermal conduction (Orlando *et al.*, 2005; Schneider and Robertson, 2017; Scannapieco and Brüggen, 2015; Brüggen and Scannapieco, 2016), and magnetic fields (Mac Low *et al.*, 1994; Fragile *et al.*, 2005; McCourt *et al.*, 2015; Banda-Barragán *et al.*, 2016; Cottle *et al.*, 2020).

In order to understand the ionization within these clouds, column densities have been approximated under the assumption of ionization equilibrium. Ion fractions can be estimated with Cloudy (Ferland *et al.*, 2017) and then applied to hydrodynamic and cosmological simulations. The EAGLE cosmological simulations, for example, have been used to predict the distributions of ions such as O VI and Ne VIII (Wijers *et al.*, 2020). Though the study mainly traces hot gas at temperatures above $10^{5.5}$ K, it is noted that as photoionization becomes relevant within the inner, multiphase regions of the CGM, a single-temperature CIE approach to estimating ions is not adequate.

The precursor to this chapter, (Cottle *et al.*, 2018), also considered ion distri-

butions under the assumption of equilibrium. In that work, column density profiles for wind-cloud interactions were estimated with the use of the post-processing tool TRIDENT (Hummels *et al.*, 2017). TRIDENT determines the ion fraction of a given cell within a hydrodynamic simulation based on the temperature and density of the cell. The column density distributions within the wind-cloud simulations were then used to approximate absorption profiles for commonly observed ions such as C IV, O VI and Ne VIII. The equilibrium assumption produced saturated profiles for low ions, while the column densities for the higher ions were barely above observable limits.

Another approach to understanding the ionization within these winds is to include non-equilibrium chemistry in the simulation, but such studies have been limited. Kwak *et al.* (2011) have tracked high ionization absorbers in high-velocity cloud simulations finding levels of ions such as C IV, N V and O VI to be above the detection limit in the turbulent mixing layer between the cloud and wind while the H I column density in the same region drops. However, these results were limited by being restricted to two dimensions and did not include potential photoionization from either galactic or extragalactic UV backgrounds. Cosmological simulations (Oppenheimer *et al.*, 2018) have also considered non-equilibrium ionization states of the CGM, reproducing levels of low ions such as C II, C III, and Mg II within a factor of two of COS-Halos observations. These simulations have been informative to the global distribution of these ions but are limited in connecting column densities to particular phases created within the interaction between outflow and cold clouds.

In this chapter, we consider wind-cloud simulations with the non-equilibrium chemistry package MAIHEM (Gray *et al.*, 2015). We investigate how the distribution of ions within these simulations differs from the distributions derived with the assumption of ionization equilibrium. The structure of this work is as follows. In Section 4.2, we describe the simulations, relevant physics, and parameter space. In

Section 4.3, we directly compare the column density distributions from these simulations to estimations with TRIDENT, and in Section 4.4, we connect the non-equilibrium distributions to observations of the CGM. We conclude with a discussion in Section 4.5.

4.2 Simulations

We performed a suite of hydrodynamic simulations of wind-cloud interactions including radiative cooling using the code FLASH (version 4.5 Fryxell *et al.*, 2000; Dubey *et al.*, 2008). These simulations were done in three dimensions using the Parabolic Piecewise Method (PPM). Non-equilibrium chemistry and cooling were implemented with MAIHEM (Gray *et al.*, 2015; Gray and Scannapieco, 2016, 2017; Gray *et al.*, 2019), which tracks the evolution of 84 species over 13 elements accounting for collisional ionization by electrons, radiative and dielectronic recombinations, charge transfer reactions, and photoionizations due to a UV background.

As tracking and calculating the reactions across the 84 ions results in very costly simulations, it was not practical to cover an identical parameter space as Scannapieco and Brüggen (2015) (Paper 1). Instead, this collection of simulations covers three Mach numbers spanning the same range as Paper 1 to capture the broad effects of differing wind parameters.

The simulations were initialized with a stationary cloud embedded in a hot wind. The cloud had an initial radius of 100 parsecs, a cloud temperature of 10^4 K, a mass density of $\rho = 10^{-24}$ g cm^{-3} and a mean particle mass of $\mu = 0.6$ and was positioned at (0, 0, 0). The simulation domain extended between -800×800 parsec in x and z and -400×800 parsec in y, which was the direction of the hot, outflowing material. The interaction at the lower y-boundary was defined by a condition where the incoming material is added to the grid and given the same values of density,

temperature, velocity ($v_{\rm hot}$), and sound speed ($c_{\rm s,hot}$) initial wind conditions. For all other boundaries, the FLASH "diode" condition was used, which assumes the gradient normal to the edge of the domain to be zero for all variables except pressure and only allows material to flow out of the grid.

Both the cloud and the wind were assumed to have solar metallicity and were initialized to be in ionization equilibrium at their respective densities and temperatures in the presence of an ultraviolet background derived from the starburst galaxy J1226+2152 (Chisholm *et al.*, 2018a). The initial ionization states were determined from a Cloudy (Ferland *et al.*, 2017) simulation with the spectrum shape determined by the best fit STARBURST99 model to J1226+2152 and the strength determined by an ionization parameter of $\log(U) = -2$ at the cloud density. This spectrum shape and strength was also used to determine the incident radiation within MAIHEM.

In order to resolve instabilities along the boundary of the cloud without drastically increasing the computation time, the simulations made use of FLASH's adaptive mesh refinement (AMR) capabilities (Berger and Colella, 1989). Refinement was determined by the magnitude of the second derivative of density and temperature of the gas, however, we also adopted a set of additional refinement and de-refinement criteria to maintain high refinement within and near the cloud but reduce the computational cost of resolving the wind (see Paper 1 for details). At the highest resolution, five levels of refinement were used. The lowest level of refinement resulted in 4 cells per initial cloud radius while the highest level of refinement resulted in 64 cells per cloud radius.

The cloud material was also tracked as it was disrupted by the wind with the use of a scalar. At the initial setup, this scalar was set to 0 in the ambient material and 1 inside the cloud. As the gases mix, this scalar reflects the fraction of material within each cell that originated within the cloud. Finally, these simulations also followed

the cloud as it travels downwind with the use of the frame-change routine originally discussed in Paper 1.

4.2.1 Atomic Chemistry

Collisional ionization and photoionization are implemented with MAIHEM's ionizational network tracking 84 species over 13 atoms; hydrogren (H I - H II), helium (He I - He III), carbon (C I - C VII), nitrogen (N I - N VIII), oxygen (O I- O IX), neon (Ne I - Ne XI), sodium (Na I - Na VI), magnesium (Mg I - Mg VI), silicon (Si I - Si VI), sulfur (S I- S VI), argon (Ar I - Ar VI), calcium (Ca I - Ca VI), iron (Fe I - Fe VI) and electrons (e^-). Collisional ionization rates are taken from Voronov (1997).

Photoionization rates are dependent on the UV background supplied. For this work, we use the spectral shape of J1226+2152 and the rates are computed as

$$\Gamma_i = \int d\nu \frac{4\pi \mathcal{J}_\nu}{h\nu} \sigma_i(\nu), \tag{4.1}$$

where $(J)_\nu$ is the background intensity in in units of ergs s^{-1} cm^{-2} Hz^{-1} sr^{-1} and $\sigma_i(\nu)$ is the photoionization cross section from Verner *et al.* (1996). The background level is determined by the ionization parameter, defined as

$$U \equiv \frac{\Phi(\mathrm{H})}{\mathrm{n(H)c}} = \frac{4\pi}{\mathrm{n(H)c}} \int \frac{\mathcal{J}_\nu}{h\nu} d\nu, \tag{4.2}$$

where Φ(H) is the surface density of the ionizing photons and n(H) is the total hydrogen number density. The background level for these simulations is set to ensure $\log(U) = -2$ in the cold dense material. This reflects the measured ionization parameter for the feature observed within the spectra of J1226+2152.

Cooling is implemented within MAIHEM by determining the cooling rate associated with each ion in the chemical network. Ionization states that are not tracked explicitly in the network form a composite cooling curve where the cooling rate is

defined as

$$\Lambda(T) = \frac{\sum_i n_i(T)\Lambda_i(T)}{\sum_i n_i(T)}, \tag{4.3}$$

where $\Lambda_i(T)$ is the cooling rate of ion i and $n_i(T)$ is the relative abundance of ion i in equilibrium at a temperature T. The details of the cooling curve are discussed further in (Gray *et al.*, 2015).

While including a UV background and photoionization, it is important to also consider photoheating. The implementation of photoheating was added to MAIHEM along with the framework of including a UV background. The photoheating rate for each ion is computed as

$$\mathcal{H}_i = \int d\nu \frac{4\pi\mathcal{J}_\nu}{h\nu}\sigma_i(\nu)h(\nu - nu_i), \tag{4.4}$$

where $h\nu_i$ is the ionization potential of ion i.

4.2.2 Parameters

Simulation parameters are chosen to reflect wind conditions at varying radii from the outflowing region and various energy and mass input from the wind. The Mach number of the incoming material $M_{\rm hot}$ meets the first goal while the velocity of the wind material, $v_{\rm hot}$, spans the parameter space for the second (Chevalier and Clegg, 1985). The temperature of the wind is denoted by $T_{\rm hot}$ while the cloud is always at an initial temperature of 10^4 K, the minimum temperature attainable with atomic cooling.

The Jeans length for a cloud at this temperature is $\lambda_J \approx 2$ kpc. With an initial radius of 100 pc, the clouds are small enough for the simulations to not include self-gravity. Instead, the clouds are confined by pressure in order to be in equilibrium in the initial setup. Due to this, the ratio of the cloud density to the wind density, χ_0, is equal to the ratio of the temperatures of the wind and cloud. While they are

Table 4.1: Simulation parameters

Name	$M_{\rm hot}$	$v_{\rm hot}$	$T_{\rm hot}$	χ_0	$t_{\rm cc}$
		km/s	10^{-6} K		Myr/100pc
M1-v480-T1	1	480	10	1000	6.4
M3.6-v3000-T3	3.6	3000	30	3000	1.8
M6.2-v3000-T1	6.2	3000	10	1000	1.0

not quite in equilibrium due to the pressure differences created when accounting for photoheating, the difference in pressure is under 2% .

Run parameters are shown in Table 4.1 including the simulation name, wind parameters such as $M_{\rm hot}$, $v_{\rm hot}$, $T_{\rm hot}$, and the density contrast between wind and cloud, χ_0. Runs span a low, mid, and high Mach number with temperatures and density contrasts to allow for comparison between parameters.

When considering clouds embedded in hot winds, it is important to consider the evolution in terms of a timescale that normalizes the evolution across wind parameters. Here we will discuss the simulations in terms of cloud crushing time. This timescale was first introduced in Klein *et al.* (1994) and describes the time it takes the initial shock to pass halfway through the cloud and is defined as,

$$t_{\rm cc} = \frac{R_c \chi_0^{1/2}}{v_{\rm hot}}, \tag{4.5}$$

which, for a consistent cloud radius, is dependent only on the velocity of the wind, $v_{\rm hot}$, and the density ratio between the cloud and the wind, χ_0. The cloud crushing time for each wind setup is also listed in Table 4.1.

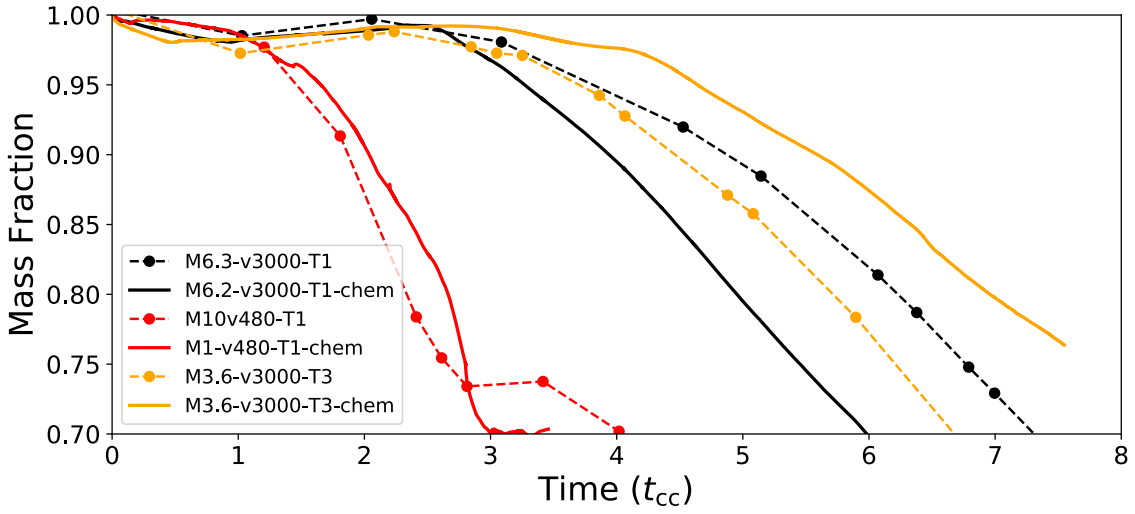

Figure 4.1: Fraction of cloud mass above $\rho_c/3$ with respect to cloud crushing time. Runs without chemistry are shown in dashed lines, and runs with chemistry are shown in solid lines. Red, yellow and black represent M1-v480-T1, M3.6-v3000-T3, and M6.2-v3000-T1 respectively.

4.3 Deviation from Equilibrium

In Figure 4.1 the fraction of cloud mass above $\rho_c/3$ is shown as a function of time both for the original equilibrium cooling runs presented in Scannapieco and Brüggen (2015) and the new nonequilibrium simulations presented in this work. In the higher Mach number cases, there is a clear difference in the evolution between the hydrodynamic simulations and those including non-equilibrium chemistry. Furthermore, the sign of this difference is dependent on the Mach number. With the inclusion of non-equilibrium chemistry, the cloud in the M6.2-v3000-T1 run is torn apart faster than the original radiative cooling run, but in the M3.6-v3000-T1 run, the inclusion of non-equilibrium chemistry extends the lifetime of the cloud.

To better understand the origin of these differences, in Figure 4.2 we plot the CIE cooling efficiency for oxygen, carbon, neon, and nitrogen as compiled by Wiersma *et al.* (2009). At approximately 10^4 K, the dominant coolants are carbon and oxygen,

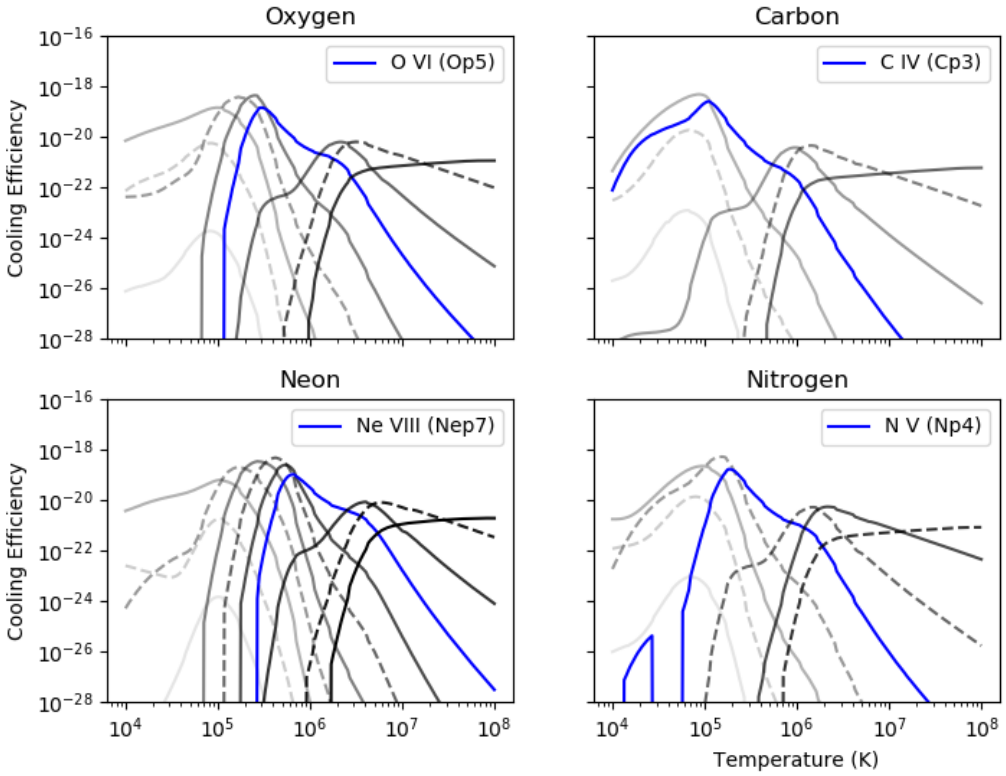

Figure 4.2: Cooling efficiencies for oxygen, carbon, neon and nitrogen from Gnat and Ferland (2012). The contribution at the initial CIE from individual ions are shown in gray, increasing in saturation with increasing ionization energy. O VI, C IV, Ne VIII, and N V highlighted in blue.

specifically C II and O II, and for the initial stages of the cloud evolution, cooling is primarily driven by these low ionization energy ions.

The equilibrium and non-equilibrium distributions of the intermediate states of carbon are shown in Figure 4.3 for M3.6-v3000-T3 and M6.2-v3000-T3. There is a clear excess in C II in M3.6-v3000-T3 while there is a clear lack of this ion in M6.2-v3000-T3. Without the efficient cooling by C II, M6.2-v3000-T1 evolves differently than a cloud assumed to be in equilibrium. Additionally, it is worth noting there is an excess of C IV in the higher Mach number run, while the level of C IV M3.6-v3000-T3 is roughly equivalent to the equilibrium distribution. Though, at core cloud

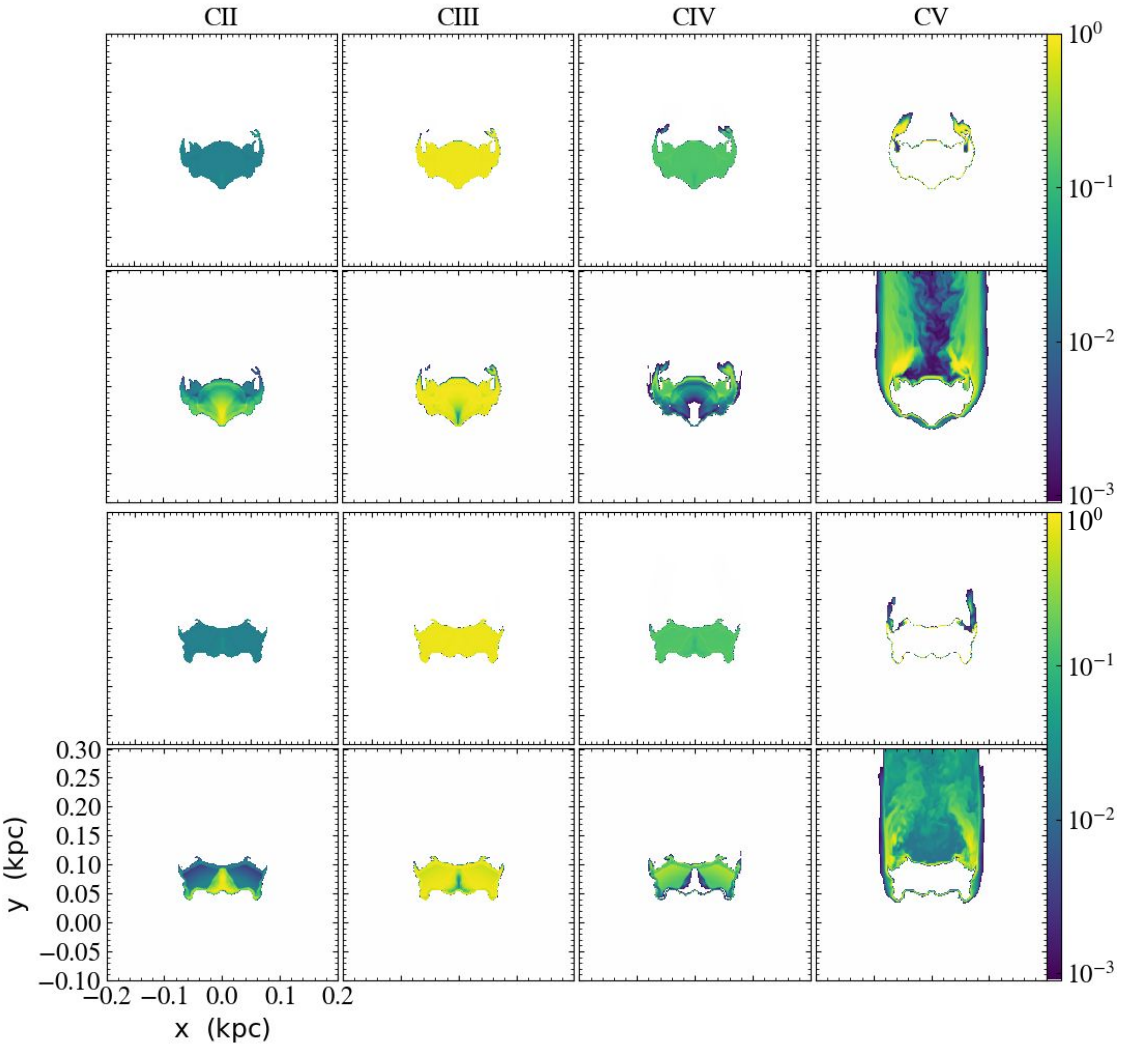

Figure 4.3: Slices of M3.6-v3000-T3 (top two rows) and M6.2-v3000-T1 (bottom two rows), with the equilbrium mass fractions (top) and non-equilibrium fractions (bottom) at 2 t_{cc} showing the mass fractions of C II, C III, C IV and C V

temperatures, C IV has low cooling efficiency.

This deficit in efficient coolants is due to two effects; the photoheating of the cloud by the background and the increased temperature of the post-shock cloud material, and the impact of these effects on the phase distribution of the material can be seen in Figure 4.4. Quantitatively, we can determine the temperature of the pre-shock cloud material after photoheating from the equilibrium temperature of the heating and

cooling rates of a characteristic background. For the background used in these runs, a distance of 300 pc away from a starburst with an SFR of 10 $M_\odot\ y^{-1}$, the heating and cooling rates are in equilibrium at 2×10^4 K (Scannapieco, 2017). However, the increase in cloud temperature alone is not enough to shift the distribution of ionization. We must also consider the effects of the shock.

The ratio of densities and pressures between the initial and post-shock materials within the cloud is

$$\frac{\rho_1}{\rho_3} = \frac{(\gamma-1)M_t^2+2}{(\gamma+1)M_t^2}, \tag{4.6}$$

and

$$\frac{P_3}{P_1} = \frac{2\gamma M_t^2}{\gamma+1} - \frac{\gamma-1}{\gamma+1}, \tag{4.7}$$

where the initial cloud material is material 1, the post-shock material is material 3 and M_t is the Mach number of the transmitted shock. Similar relations hold for the initial wind material (2) and the post-shock wind material (4). Taking advantage of the initial pressure equilibrium between the wind and the cloud and $\rho_3/\rho_4 = \chi_0$, we can solve for M_t

$$M_t = M_{\rm ps}\frac{1+(1+4M_{ps}^{-2})^{1/2}}{2}, \tag{4.8}$$

where $M_{\rm ps} = M_2\frac{\gamma+1}{2(1+\chi_0^{-1/2})}$. Treating the cloud material as an ideal gas and using Equations 4.3 and 4.7 together, the post-shock temperature for the cloud material is

$$T_{ps} = \left[\frac{2\gamma M_t^2}{\gamma+1} - \frac{\gamma-1}{\gamma+1}\right]\left[\frac{(\gamma-1)M_t^2+2}{(\gamma+1)M_t^2}\right]T_1. \tag{4.9}$$

Using this relation, and assuming a cloud with an initial temperature of 10^4K, the post-shock temperature for M3.6-v3000-T3 is 8.4×10^4 K, or about 10.8 eV. For M6.2-v3000-T1, the post-shock temperature is 2.16×10^5 K, approximately 27.8 eV. This can be compared to the 24.38 eV required to ionize C II to C III to illustrate shock-heating alone is not enough to ionize carbon well past C II and on to C IV.

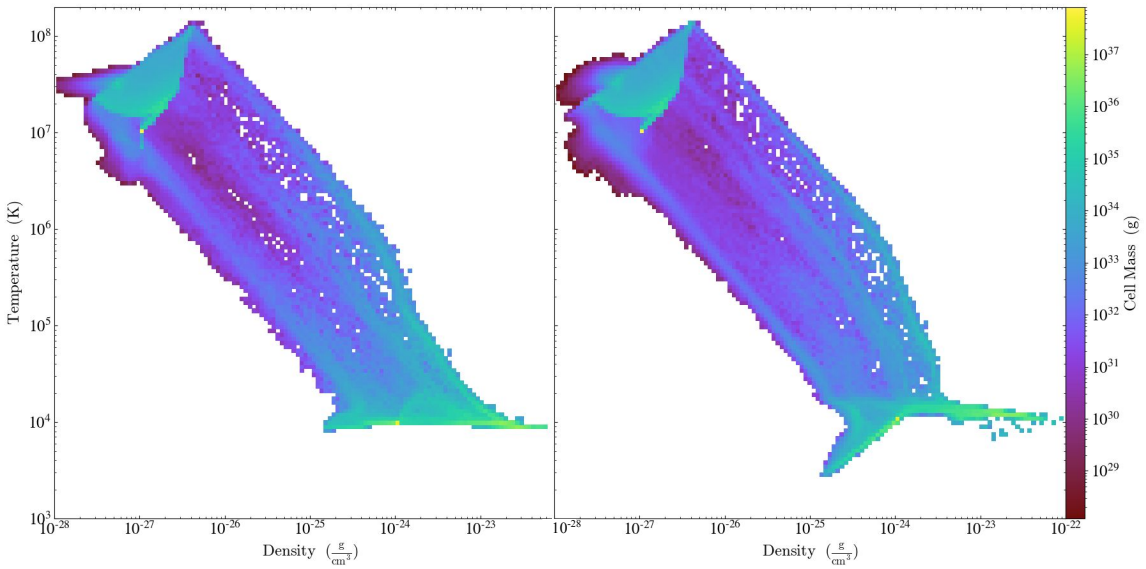

Figure 4.4: Phase plots for M6.2-v3000-T3 and the counterpart equilibrium run from Scannapieco and Brüggen (2015), at 1 t_{cc}.

However, if we consider the temperature of the cloud after heating by the background, 2×10^4 K, the post-shock temperature for the cloud for M3.6-v3000-T3 is 1.68×10^5 K, or about 21.6 eV. For M6.2-v3000-T1, the post-shock temperature is 4.31×10^5 K, or approximately 55.8 eV. This is well above 47.88 eV, the energy to ionize C III to C IV. This energy is also high enough to ionize a significant fraction of oxygen to intermediate ions such as O IV. As carbon and oxygen are the dominant coolants for temperatures between 10^4 and 10^5, the lack of these coolants suppresses cooling in M6.2-v3000-T3 such that the cloud is destroyed faster than the cloud without chemistry.

This lack of efficient coolants in the heart of the cloud is most important to the early evolution. Later in the cloud lifetime, as Rayleigh-Taylor instabilities grow, the majority of carbon can be found in C II and C III near the front of the cloud, causing it to become denser. This increase in density also leads to an increase in cooling efficiency. The beginning of this effect can be seen in Figure 4.3. For later

times, such as t_{90} and t_{75}, when 90% and 75% of the cloud remain above $\rho_c/3$, the distribution of ionization in the cloud tends towards these lower states. We discuss the implication of this for observations in Section 4.4.

4.3.1 Low Mach Numbers

In the Mach 1 and Mach 3 runs, the time it takes the cloud to lose 10% of its mass is longer for the simulations including MAIHEM. The clouds are slightly more stable and the lifetimes of the clouds are longer than the radiative clouds without chemistry. In Figures 4.5 and 4.6, we show the distribution of mass fraction distributions for Mg II, C IV, O VI and Ne VIII for M1-v480-T1 at 2 t_{cc} and M3-v3000-T3 at 4.2 t_{cc}; the times the non-chemistry reached 90% of cloud mass within the domain. The top two rows of both figures show the distribution of each ion estimated by TRIDENT under the assumption of CIE for the given density and temperature of each cell, with the top reflecting the original radiative simulations and the middle reflecting the runs presented in this work. The bottom row shows the distribution of each ion from MAIHEM. Figure 4.7 shows the same for M6.2-v3000-T1 at 4.4 t_{cc}, the time when the corresponding run without chemistry reached 90% of cloud mass in the domain.

Considering M3.6-v3000-T3, the low energy ions have more structure within the cloud caused by the passing of the initial shock. However, the largest difference appears within the tail of the cloud for the intermediate and high-energy ions. It is clear that the non-equilibrium distributions show more production of both O VI and Ne VIII along the boundary and in the tail of the cloud, showing a significant deviation from the expectation at PIE and CIE. These ions are the most effective states for cooling for these atoms at temperatures around 10^6K, which is very near the average temperature along the cloud boundary and within the tail, shown in Figure 4.8. The high production of O VI and Ne VIII enhances the cooling efficiency

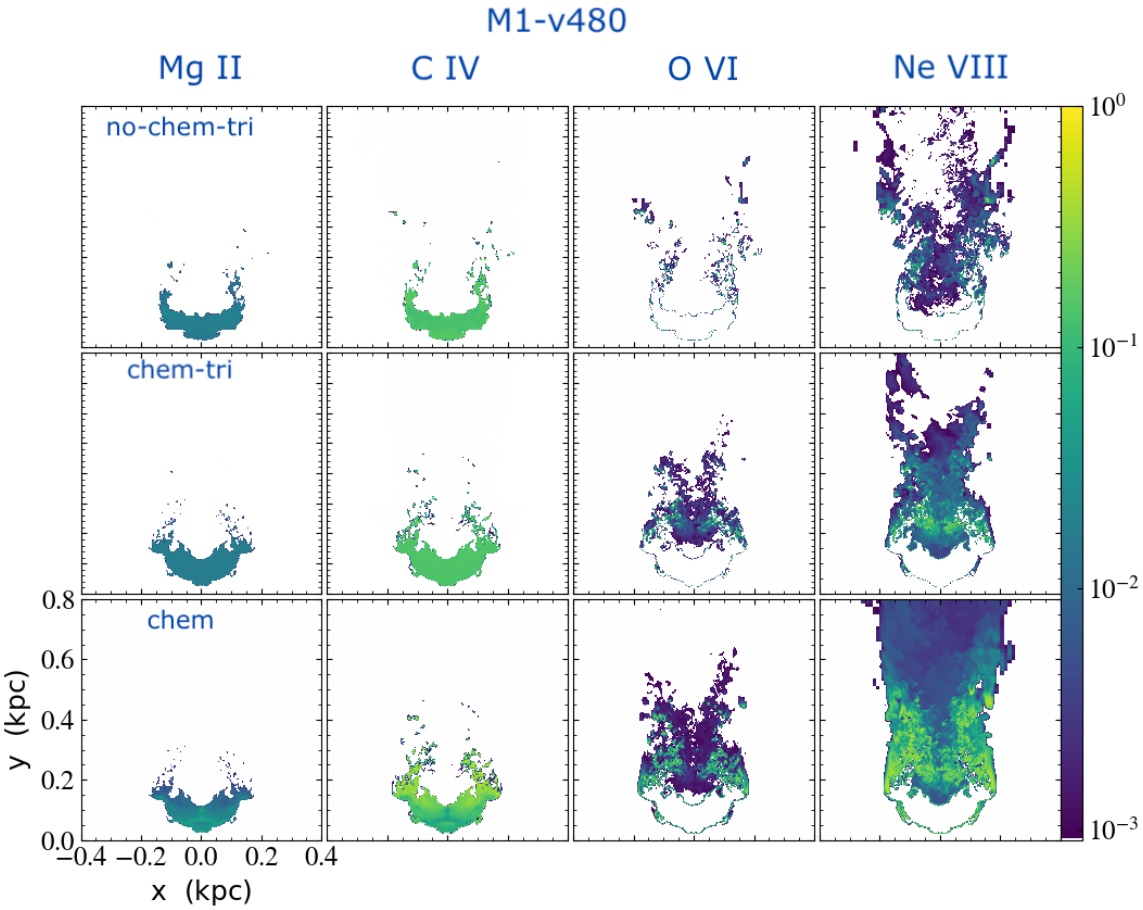

Figure 4.5: Slices of M1-v48-T1 at 2 t_{cc} showing the mass fractions of Mg II, C IV, O VI and Ne VIII. The estimations with TRIDENT of the non-chem runs are shown on the top, TRIDENT estimations of the runs with MAIHEM are shown in the middle, and the distributions from MAIHEM shown on the bottom.

along the boundary of the cloud enabling the cloud to stay a dense, compact core for longer. This effect is also apparent in M1-v480-T1 albeit to a lesser extent.

4.4 Connection to Observations

Under the assumption of photo and collisional ionization equilibrium, the observational attributes of these clouds fall short of capturing the behavior of galactic outflows that have been observed. Cottle *et al.* (2018) demonstrated that absorption profiles created with the equilibrium distributions of commonly observed ions were

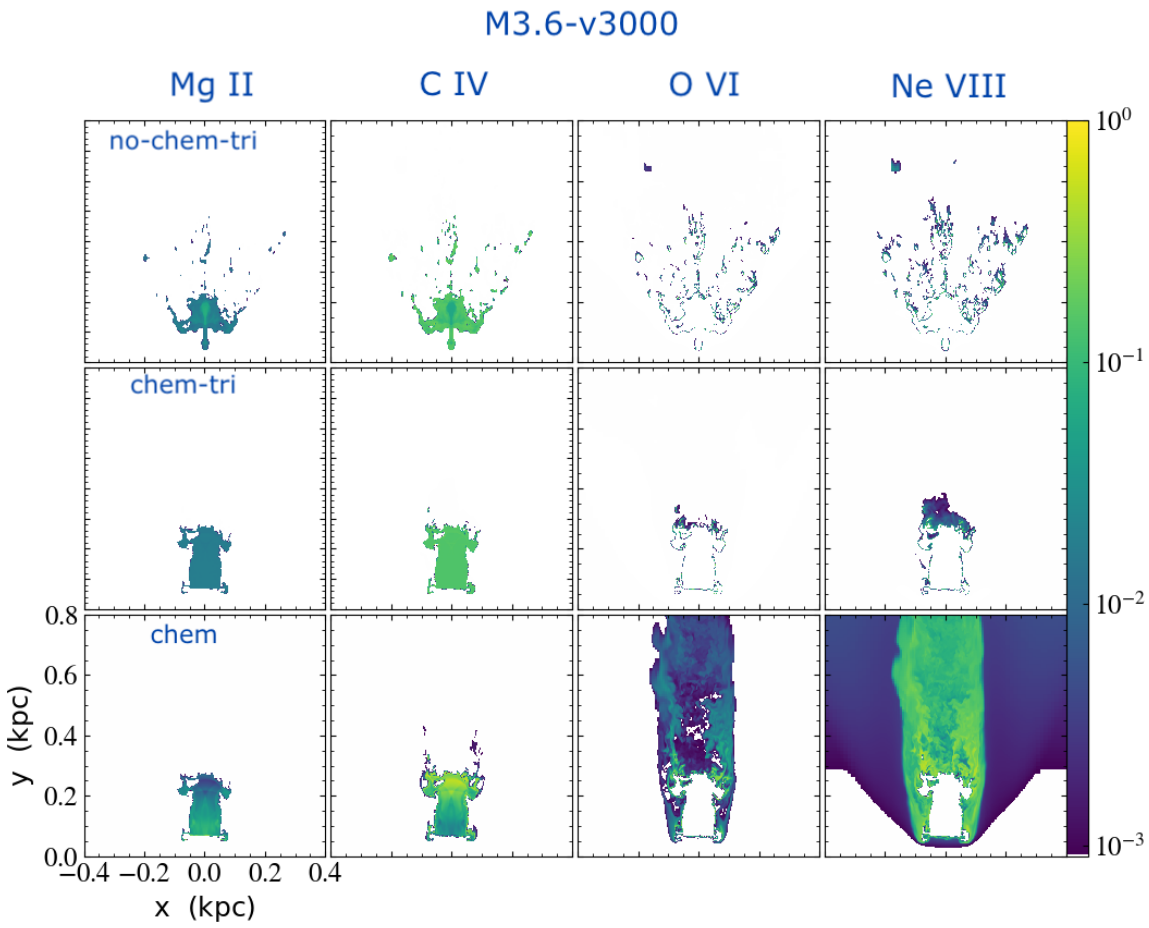

Figure 4.6: Slices of M3.6-v43000 at 4.2 t_{cc} showing the mass fractions of Mg II, C IV, O VI and Ne VIII. The estimations with TRIDENT of the non-chem runs are shown on the top, TRIDENT estimations of the runs with MAIHEM are shown in the middle, and the distributions from MAIHEM shown on the bottom.

not a good fit to the down-the-barrel observations of S1226 discussed in Chisholm *et al.* (2018a). In this section, we discuss the effect non-equilibrium chemistry has on these observables.

Column density profiles can be estimated from the ionization fractions calculated within the MAIHEM simulations. While the cloud can be observed from any angle, we focus on one of the most distinct angles; down-the-barrel of the wind or projections along the y axis. To best represent the distribution of column densities along the line

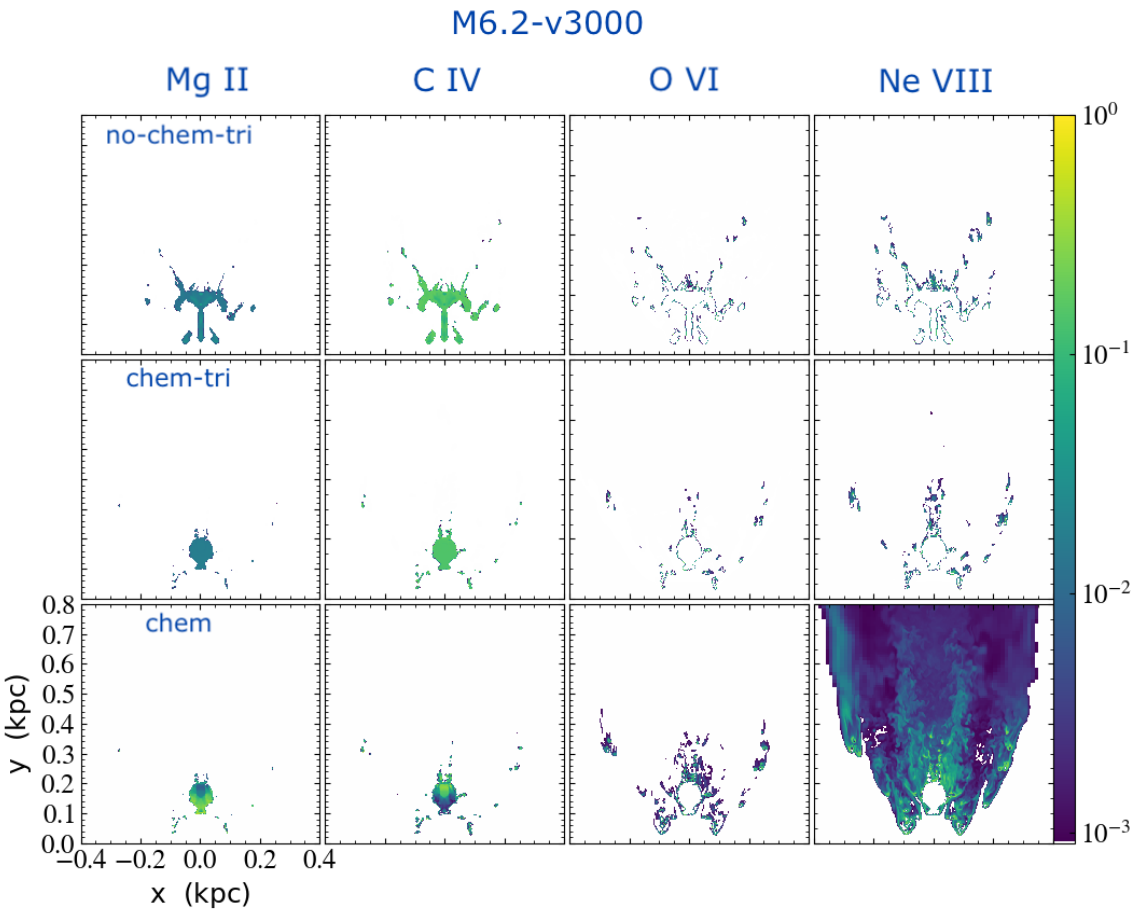

Figure 4.7: Slices of M6.2-v43000 at 4.4 t_{cc} showing the mass fractions of Mg II, C IV, O VI and Ne VIII. The estimations with TRIDENT of the non-chem runs are shown on the top, TRIDENT estimations of the runs with MAIHEM are shown in the middle, and the distributions from MAIHEM shown on the bottom.

of sight of an observation such as COS-Halos, we assume that the entire domain is contained within the line of sight. We project the simulation along the y axis and sample a 1.6 kpc × 1.6 kpc box around the cloud at a resolution of 800 × 800. This results in a single cell covering 4 pc^2.

In Figure 4.9, we plot these column densities as a function of the area covered within the line of sight, sorted from highest to lowest, in units of the initial cloud area. This can be interpreted as at a given area, x, the densest pixels that cover area x are all at or above $f(x)$. The steeper this distribution is the fewer high-density

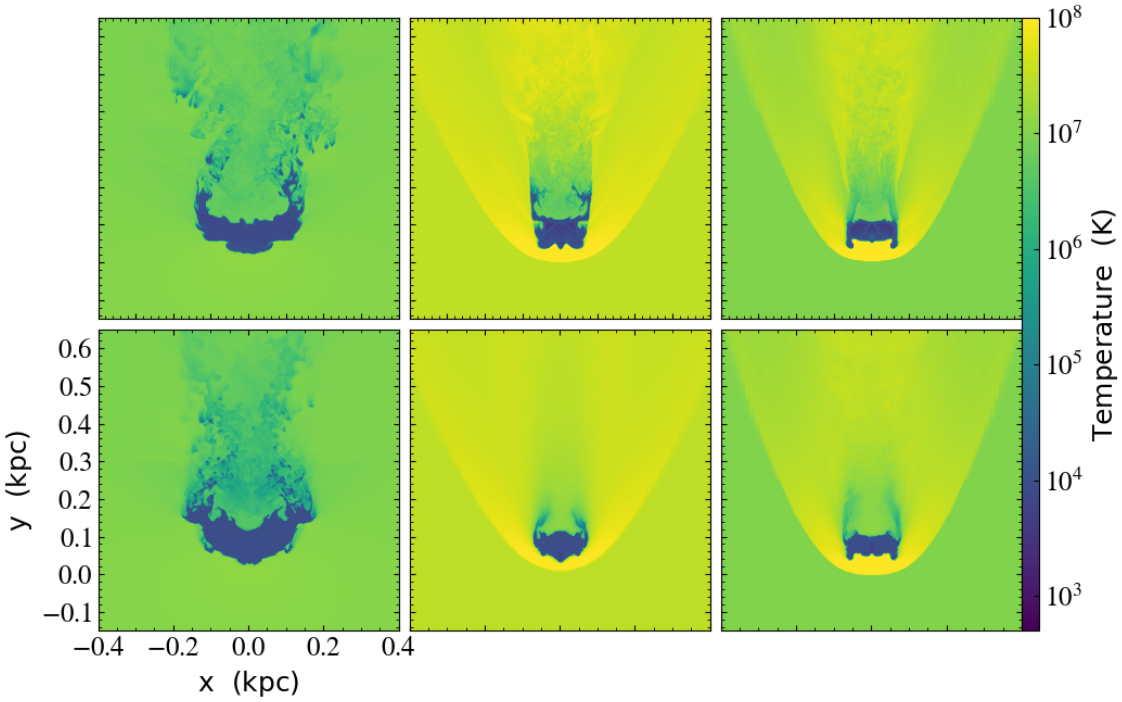

Figure 4.8: Slices of temperature at 2 t_{cc}. Top (left to right): M1-v480-T1, M3.6-v3000-T3 and M6.2-v3000-T1 runs without chemistry. Bottom: the same as the top row for the runs with non-equilibrium chemistry.

pixels there are. These distributions highlight whether the excess of a given ion in the non-equilibrium simulations is due to a small very dense portion of the cloud or a wider area of more diffuse gas.

With the assumption of equilibrium, the column density profiles generally clearly map the visible surface area of the cloud. This remains true for low energy ions that are only found within the cold cloud material such as Mg II and C II. However, for ions produced within the interactions on the boundary and in the tail of the cloud, the distribution of column densities becomes broader. In Figure 4.9 the distributions for Mg II, N V and O IV in M3.6-v3000-T3 at t_{75} are shown. The non-equilibrium distributions predict higher amounts of all three ions. However, for Mg II there is only a verticle shift in these profiles. The shape remains the same as the equilibrium

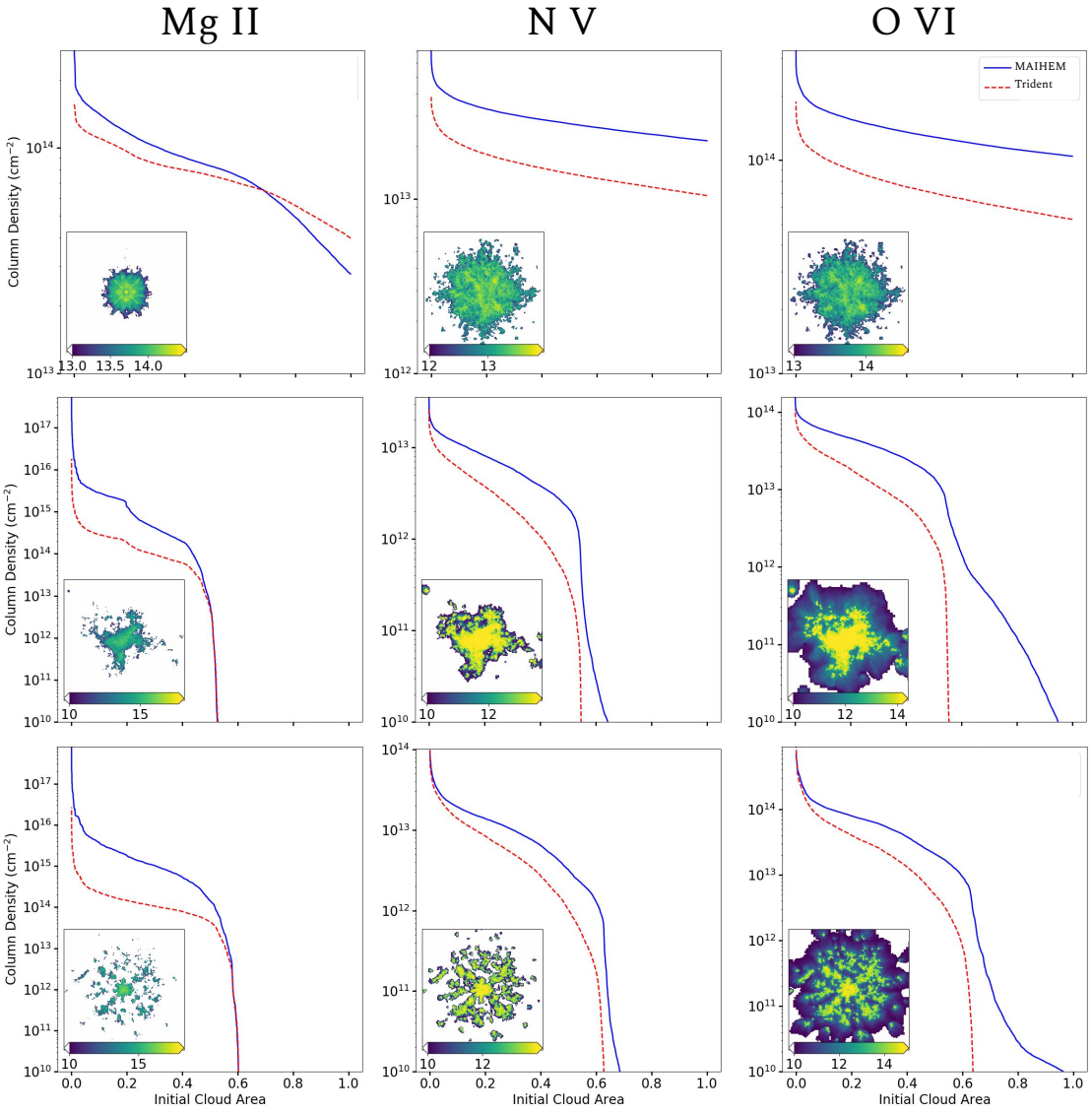

Figure 4.9: Column density profiles for Mg II (left), N V (center) and O VI (right) at t_{75} for M1-v480-T1 (top row), M3.6-v3000-T3 (middle row) and M6.2-v3000-T3 (bottom row). The equilbirium assumption from TRIDENT is shown as red dashed lines, the non-equilibrium distribution from MAIHEM is shown as the blue solid lines. The inset shows the log of the non-equilibrium projected ion densities for each ion.

profile but all column densities are higher. For N V and O VI, the non-equilibrium profiles take a different shape than the equilibrium profiles. Even for these higher energy ions, the profiles in equilibrium fall off as they approach the visible surface area of the cloud, much like the low energy ions. This is not the case for the non-equilibrium profiles. N V and O VI are produced along the boundary and within the tail of the cloud as the cloud material interacts with the wind. This is reflected in the broader profiles extending over a larger visible area than the cold cloud material alone. This effect increases with ionization energy, as O VI is broader than N V. This is due to the hotter, highly ionized tail material being more diffuse than the material at the interface of the cloud.

These trends are also evident in the profiles for M6.3-v3000-T1, shown in the bottom row of Figure 4.9, though the extent of the broadening is lessened due to the high Mach number wind more quickly destroying the cloud into small fragments. The ionizing shocks are not strong enough in M1-v480-T1 to produce a significant difference between the equilibrium and non-equilibrium profiles, resulting in only a shift vertically for all ions.

We then use these distributions to estimate the average column density observable along the line of sight. The average column density is equal to

$$N_{i,\mathrm{tot}} = \int N_i(x)dx, \tag{4.10}$$

for ion i. We integrate over 2 initial cloud areas as beyond that limit most ions are not dense enough to be observed. In Figure 4.10 the difference between the average column density in the non-equilibrium distributions and average column density in the equilibrium assumption is shown for observable ions over all three runs at t_{75}. Notably, as the Mach number of the wind increases the amount of ions produced in dense, efficiently cooling material such as Mg II and C II is underestimated in the assumption

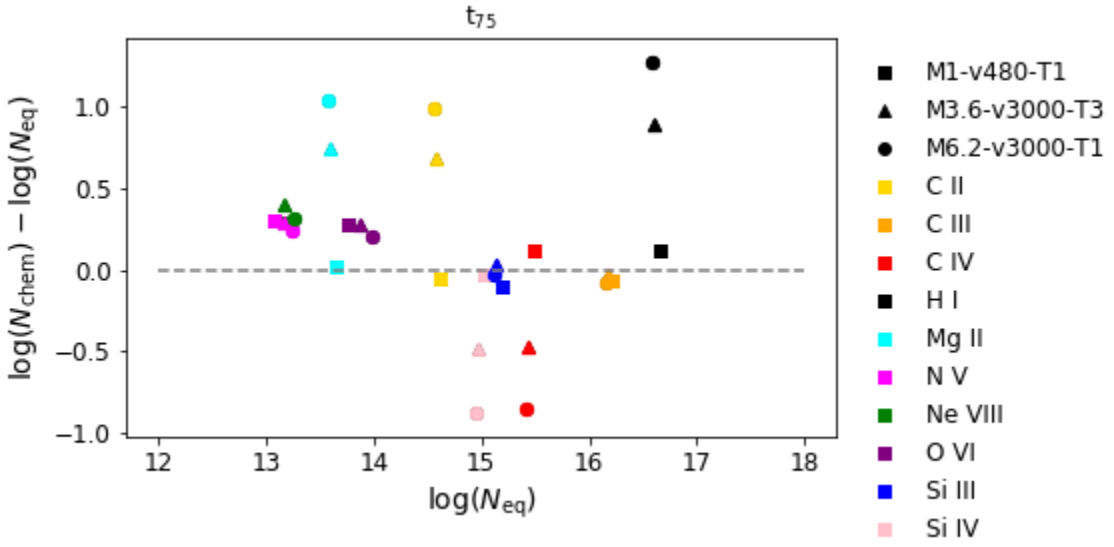

Figure 4.10: The difference between the average column densities in the non-equilibrium simulations and the average column density from the assumption of equilibrium at t_{75}. The runs are differentiated by marker; M1-v480-T1 is shown by squares, M3.6-v3000-T3 by triangles and M6.2-v3000-T1 by circles.

of equilibrium leading to larger differences in column density, up to 1 dex. However, the collisionally ionized ions such as C IV and Si IV are consistently overestimated by the equilibrium assumption. While equilibrium assumes that most carbon and silicon within the cloud are at these intermediate states due to the temperature of the cloud, the non-equilibrium simulations capture the cooling effect of the higher density material that results in the majority of these atoms populating lower energy states. The initial increase in these lower ions can be shown in Figure 4.3.

Ions that are typically found on the boundary and within the tail of the cloud such as N V, O IV, and Ne VIII are underestimated in equilibrium, though by a smaller margin than the intermediate ions. For these ions, there is also little dependence on the Mach number in the wind as they are not influenced by the shock or cooling of the core of the cloud. Instead, the interaction between the wind and cloud through hydrodynamic instabilities leads to higher production of these ions than if the material

Table 4.2: The average column densities estimated from the column density profiles for both the equilibrium assumption (N_{eq}) and the non-equilibrium distributions (N_{chem}) for M1-v480-T1

Ion	M1-v480-T1		M3.6-v3000-T3		M6.2-v3000-T1	
	N_{eq}	N_{chem}	N_{eq}	N_{chem}	N_{eq}	N_{chem}
H I	16.66	16.77	16.59	17.48	16.58	17.86
Mg II	13.65	13.67	13.58	14.33	13.58	14.62
C III	16.22	16.15	16.16	16.13	16.15	16.07
C IV	15.48	15.59	15.42	14.95	15.41	14.56
N V	13.06	13.36	13.15	13.45	13.23	13.47
O IV	13.76	14.04	13.87	14.15	13.99	14.19
Ne VIII	13.20	13.49	13.17	13.56	13.26	13.57
C II	14.62	14.56	14.57	15.26	14.56	15.55
Si III	15.18	15.07	15.13	15.16	15.11	15.08
Si IV	15.03	15.00	14.96	14.48	14.95	14.07

is assumed to be in ionization equilibrium from its temperature alone. Ions that are primarily photoionized by the UV background such as C III and Si III have little difference between equilibrium and non-equilibrium. Since equilibrium distributions account for the influence of a UV background, this implies that these ions are primarily photoionized rather than collisionally ionized through thermal and hydrodynamic motions. The average column density estimates for all runs can be found in Table 4.2.

The higher column densities estimated from the non-equilibrium distributions are in agreement with column density observations of the CGM. Anshul *et al.* (2021) considered pairs of sightlines to map O VI around a starburst galaxy finding both a central component and a blue-shifted component at 70 km/s. They estimated the

column densities of O VI for these two components to be 14.06 and 13.89, respectively. Our results are in agreement with these observations with $\log(N_{\rm OVI}) = 14.04$ to 14.19. Burchett *et al.* (2019) surveyed the Ne VIII absorption within the CGM of starburst galaxies finding $\log(N_{\rm OVI}) \approx 13.5 - 15.0$. They also theorize that the neon is collisionally ionized near the virial temperature of these galaxies because the cool, low-density gas required for photoionization to produce a similar amount of Ne VIII is unlikely. Our estimation for the column density of Ne VIII of shocked, wind-swept clouds is consistent with the idea that Ne VIII is primarily collisionally ionized within the CGM.

The statistics of the COS IGM survey presented in Danforth *et al.* (2016) show the distribution of column densities of O VI, N V, C IV, C III along between 70 to 280 sightlines. Our estimations of the column densities of O VI and N V are consistent with these distributions. For the column densities not near the center of these distributions, such as C IV, the differences between the non-equilbirium and equilbirium column densities bring our estimations of these column densities towards the center of the COS distributions. In the case of C IV, in equilibrium $\log(N_{\rm CIV}) \approx 15.4$ whereas the non-equilbrium estimation is $\log(N_{\rm CIV}) \approx 14.9$, closer to the median of the COS survey distribution of $\log(N_{\rm CIV}) \approx 13.8$. In the case of C III, our estimation of the column density falls outside of the distribution of the COS sightlines. However, as discussed earlier in this section, the ionization of C III is likely primarily due to photoionization, making the column density of C III very sensitive to the UV background.

4.5 Summary and Conclusions

We have presented a suite of three-dimensional AMR wind-cloud simulations with both radiative cooling and non-equilibrium chemistry and have investigated the effects

of non-equilibrium chemistry on the evolution and disruption of these cold clouds. In addition, we have discussed the influence of non-equilibrium chemistry on the column density profiles of commonly observed ions. These simulations have modeled the effect of photoheating from a background spectrum as well as thermal and collisional ionization. With the inclusion of a UV background descriptive of a starburst galaxy, the clouds are heated prior to the shock altering their evolution from the equilibrium models presented in Scannapieco and Brüggen (2015). As the cloud is heated and then shocked by high Mach number winds at early times, the distribution of the ionization states shifts towards higher, less effective coolants than assumed in an equilibrium cooling model. Due to this, the high Mach number winds destroy the cloud faster in the non-equilibrium model than the models without chemistry included. In the case of low to middle Mach number winds, there is more production of intermediate ions such as N V and O VI along the boundary of the cloud, enhancing cooling and extending cloud lifetimes. We also describe the column density distribution of commonly observed ions as a profile through a similar method in Cottle *et al.* (2018). The average column densities are estimated as the integrated column density over two cloud areas along the line of sight. These estimations demonstrate that the equilibrium approach to estimating column densities can underestimate ions within the tail of the cloud such as N V, O IV and Ne VIII by ≈ 0.4 dex. This could lead to stronger absorption lines more in line with the multiphase observations of outflows. The non-equilibrium simulations also capture the cooling of dense cloud material at late times leading to more of the cloud material populating low states such as C II and Mg II. We conclude the column densities for these ions are underestimated in the equilibrium assumption by up to 1 dex. In addition, our column densities are consistent with maps of both O VI and Ne VIII (Anshul *et al.*, 2021; Burchett *et al.*, 2019) as well as within the distribution of the COS survey sightlines (Danforth *et al.*,

2016).

While this study has demonstrated the stark contrast between the equilibrium ionization and non-equilibrium approaches, there are limitations to our models. These simulations included the effect of a UV background representative of a young starburst galaxy with a high ionization parameter. However, this ionization parameter can vary greatly between observations of the CGM and limits our ability to thoroughly connect these simulations to observations. In addition, we consider a limited range of wind parameters. As the Mach number of the wind can be a proxy for the distance from the host galaxy, our range of Mach numbers is a small sampling of possible impact parameters. This limitation is primarily due to the large computational cost of modeling the chemical network through each simulation, with a single run costing 120,000 node hours.

Connections between wind-cloud simulations and observations are limited by our ability to model the ionization mechanisms of the CGM. In this work, we have demonstrated the significant effect non-equilibrium chemistry has on the distribution of column densities. While post-processing tools such as TRIDENT can model collisional and photoionization in equilibrium, it is necessary to consider the full chemical network as well as the effects of photoheating to capture the ionization structure of multiphase outflows.

Chapter 5

CONCLUSION

This work presents three main studies focusing on the evolution and disruption of cold clouds embedded in hot winds. These wind-cloud systems have a significant influence on the evolution and star formation histories of starburst galaxies. While observations of cold gas within the hot CGM can provide a snapshot of the galactic environment, numerical simulations have the ability to follow the interaction through time and provide context for observations. Analysis of these simulations shed light on the dominant physical factors that lead to the observed properties. The work presented here contributes to the understanding of these physical factors and the distribution of observable gas within the simulations.

The suite of magnetohydrodynamic simulations demonstrated how the stability of the cloud is dependent on the alignment of the field and the wind. While radiative cooling has been shown to extend cloud lifetimes (Scannapieco and Brüggen, 2015), the inclusion of magnetic fields aligned with the wind did not create any additional cloud stability. The magnetic pressure support within the clouds creates more diffuse tails with higher mixing fractions. Conversely, magnetic fields transverse to the wind are draped within an amplified field that creates a pressure barrier between the cloud and the wind inhibiting mixing. This envelope protects the cloud from hydrodynamic instabilities but the amplified and draped field lines create pressure pushing the cloud rapidly in the direction orthogonal to the wind and field, accelerating mass loss. With such a clear distinction between the effects of each orientation, this study demonstrated the need to consider not only the presence of but also the orientation of magnetic fields when modeling wind-cloud interactions. Transverse fields in par-

ticular are likely to lead to faster destruction of clouds rather than create stability as previously thought (Mac Low *et al.*, 1994).

In efforts to better connect simulations to observations, we estimated the column densities of observable ions within the wind-cloud interactions. These column densities, estimated with the tool Trident, assumed collisional ionization equilibrium (CIE). While this is a reasonable assumption for the ambient CGM, it became clear the shocks and instabilities within the interaction have a great impact on the ionization of the cloud gas. The initial estimations for the column densities were used to generate simulated absorption profiles that were over-saturated for the low energy ions while the high energy ion profiles were much wider than observations. The CIE estimation predicted most of the high energy ions were within the fast-moving wind, while observations indicate they can be found at intermediate velocities, likely on the boundary between the cloud and wind.

The conclusions from the equilibrium estimations provided clear motivation to run a new suite of simulations that accounted for non-equilibrium chemistry. This new set of simulations was able to better capture the production of intermediate and high-energy ions along the cloud boundary. Tracking the individual states of each element also provided a better estimate of the cooling efficiency across cloud and wind temperatures. Coolants such as O VI and C V are much more abundant in the non-equilibrium distributions, leading to more efficient cooling for low and mid Mach number winds. However, the combination of photoheating from the UV background and strong shocks created in the high Mach number winds lead to ionization past the efficient coolants at cloud temperatures. In this case, the cloud is destroyed faster than the cloud assumed to be in ionization equilibrium. The inclusion of non-equilibrium chemistry brings the estimation of observable column densities within these simulations to be in more agreement with the distribution of observed CGM

column densities in the COS survey.

Understanding the evolution and ionization of the CGM sheds light on one of the primary mechanisms by which galaxies interact with their environment. While observations of this multiphase gas can measure the acceleration and density, the interactions between the hot and cold material must be studied in greater detail to fully understand how the two phases coexist. While effects like radiative cooling and magnetic fields can stabilize an existing cloud embedded in a wind, there are other possible explanations for the range of ionization states we observe. One possibility is the cooling and condensation of wind gas as it travels well beyond the galactic disk. Rather than relying on the mechanisms to maintain the low energy states within cool gas, the hot wind gas can cool into dense cloudlets passing through the intermediate states observed. These cloudlets would already be traveling at wind velocities and could easily be accelerated beyond the CGM. It has been suggested that this condensation occurs within the tails of preexisting clouds, extending the lifetime of gas near the initial cloud density (Gronke and Oh, 2018).

The interaction of galaxies with their surroundings plays a significant role in the evolution of the galaxy as a whole. Gas recycling through inflows and outflows can impact the composition and formation rate of new stars. Despite the pivotal role of outflowing gas, there is much to still be learned about the details of the acceleration and ionization of this material. As models expand to include the combination of additional physical factors we begin to layer the effects into a broader picture of the interconnectedness of galaxies and their environments. It is through this incremental process that we hope this work contributes to the broader understanding of the universe.

Adebahr, B., M. Krause, U. Klein, G. Heald and R.-J. Dettmar, "M 82 - A radio continuum and polarisation study. II. Polarisation and rotation measures", A&A **608**, A29 (2017).

Agertz, O. and A. V. Kravtsov, "On the Interplay between Star Formation and Feedback in Galaxy Formation Simulations", ApJ **804**, 18 (2015).

Agol, E., "Sagittarius A* Polarization: No Advection-dominated Accretion Flow, Low Accretion Rate, and Nonthermal Synchrotron Emission", ApJ **538**, 2, L121–L124 (2000).

Anshul, P., A. Narayanan, S. Muzahid, A. Beckett and S. L. Morris, "Pair Lines of Sight Observations of Multiphase Gas Bearing O VI in a Galaxy Environment", MNRAS (2021).

Arav, N., B. Borguet, C. Chamberlain, D. Edmonds and C. Danforth, "Quasar outflows and AGN feedback in the extreme UV: HST/COS observations of HE 0238-1904", MNRAS **436**, 3286–3305 (2013).

Arribas, S., L. Colina, E. Bellocchi, R. Maiolino and M. Villar-Martín, "Ionized gas outflows and global kinematics of low-z luminous star-forming galaxies", A&A **568**, A14 (2014).

Baganoff, F. K., Y. Maeda, M. Morris, M. W. Bautz, W. N. Brandt, W. Cui, J. P. Doty, E. D. Feigelson, G. P. Garmire, S. H. Pravdo, G. R. Ricker and L. K. Townsley, "Chandra X-Ray Spectroscopic Imaging of Sagittarius A* and the Central Parsec of the Galaxy", ApJ **591**, 2, 891–915 (2003).

Banda-Barragán, W. E., C. Federrath, R. M. Crocker and G. V. Bicknell, "Filament formation in wind-cloud interactions- II. Clouds with turbulent density, velocity, and magnetic fields", MNRAS **473**, 3454–3489 (2018).

Banda-Barragán, W. E., E. R. Parkin, C. Federrath, R. M. Crocker and G. V. Bicknell, "Filament formation in wind-cloud interactions - I. Spherical clouds in uniform magnetic fields", MNRAS **455**, 1309–1333 (2016).

Banda-Barragán, W. E., F. J. Zertuche, C. Federrath, J. García Del Valle, M. Brüggen and A. Y. Wagner, "On the dynamics and survival of fractal clouds in galactic winds", MNRAS **486**, 4, 4526–4544 (2019).

Barger, K. A., N. Lehner and J. C. Howk, "Down-the-barrel and Transverse Observations of the Large Magellanic Cloud: Evidence for a Symmetric Galactic Wind on the Near and Far Sides of the Galaxy", ApJ **817**, 2, 91 (2016).

Berger, M. and P. Colella, "Local adaptive mesh refinement for shock hydrodynamics", Journal of Computational Physics **82**, 1, 64–84 (1989).

Bland-Hawthorn, J. and M. Cohen, "The Large-Scale Bipolar Wind in the Galactic Center", ApJ **582**, 1, 246–256 (2003).

Bolatto, A. D., S. R. Warren, A. K. Leroy, F. Walter, S. Veilleux, E. C. Ostriker, J. Ott, M. Zwaan, D. B. Fisher, A. Weiss, E. Rosolowsky and J. Hodge, "Suppression of star formation in the galaxy NGC 253 by a starburst-driven molecular wind", Nature **499**, 450–453 (2013).

Borthakur, S., T. Heckman, D. Strickland, V. Wild and D. Schiminovich, "The Impact of Starbursts on the Circumgalactic Medium", ApJ **768**, 18 (2013).

Brüggen, M. and E. Scannapieco, "The Launching of Cold Clouds by Galaxy Outflows. II. The Role of Thermal Conduction", ApJ **822**, 31 (2016).

Burchett, J. N., T. M. Tripp, J. X. Prochaska, J. K. Werk, J. Tumlinson, J. C. Howk, C. N. A. Willmer, N. Lehner, J. D. Meiring, D. V. Bowen, R. Bordoloi, M. S. Peeples, E. B. Jenkins, J. M. O'Meara, N. Tejos and N. Katz, "The COS Absorption Survey of Baryon Harbors (CASBaH): Warm-Hot Circumgalactic Gas Reservoirs Traced by Ne VIII Absorption", ApJ **877**, 2, L20 (2019).

Calzetti, D., L. Armus, R. C. Bohlin, A. L. Kinney, J. Koornneef and T. Storchi-Bergmann, "The Dust Content and Opacity of Actively Star-forming Galaxies", ApJ **533**, 682–695 (2000).

Carretti, E., R. M. Crocker, L. Staveley-Smith, M. Haverkorn, C. Purcell, B. M. Gaensler, G. Bernardi, M. J. Kesteven and S. Poppi, "Giant magnetized outflows from the centre of the Milky Way", Nature **493**, 7430, 66–69 (2013).

Chandrasekhar, S., *Hydrodynamic and hydromagnetic stability* (1961).

Chandrasekhar, S., *Hydrodynamic and Hydromagnetic Stability*, Dover Books on Physics Series (Dover Publications, 1981), URL `https://books.google.com/books?id=oU_-6ikmidoC`.

Chevalier, R. A. and A. W. Clegg, "Wind from a starburst galaxy nucleus", Nature **317**, 44 (1985).

Chisholm, J., R. Bordoloi, J. R. Rigby and M. Bayliss, "Feeding the fire: tracing the mass-loading of 10^7 K galactic outflows with O VI absorption", MNRAS **474**, 2, 1688–1704 (2018a).

Chisholm, J., R. Bordoloi, J. R. Rigby and M. Bayliss, "Feeding the fire: tracing the mass-loading of 10¡SUP¿7¡/SUP¿ K galactic outflows with O VI absorption", MNRAS **474**, 1688–1704 (2018b).

Colella, P. and P. R. Woodward, "The Piecewise Parabolic Method (PPM) for Gas-Dynamical Simulations", Journal of Computational Physics **54**, 174–201 (1984).

Cooper, J. L., G. V. Bicknell, R. S. Sutherland and J. Bland-Hawthorn, "Starburst-Driven Galactic Winds: Filament Formation and Emission Processes", ApJ **703**, 330–347 (2009).

Cottle, J., E. Scannapieco and M. Brüggen, "Column Density Profiles of Cold Clouds Driven by Galactic Outflows", ApJ **864**, 1, 96 (2018).

Cottle, J., E. Scannapieco, M. Brüggen, W. Banda-Barragán and C. Federrath, "The Launching of Cold Clouds by Galaxy Outflows. III. The Influence of Magnetic Fields", ApJ **892**, 1, 59 (2020).

Cowie, L. L. and C. F. McKee, "The evaporation of spherical clouds in a hot gas. I - Classical and saturated mass loss rates", ApJ **211**, 135–146 (1977).

Creasey, P., T. Theuns and R. G. Bower, "How supernova explosions power galactic winds", MNRAS **429**, 1922–1948 (2013).

Dalla Vecchia, C. and J. Schaye, "Simulating galactic outflows with kinetic supernova feedback", MNRAS **387**, 1431–1444 (2008).

Danforth, C. W., B. A. Keeney, E. M. Tilton, J. M. Shull, J. T. Stocke, M. Stevans, M. M. Pieri, B. D. Savage, K. France, D. Syphers, B. D. Smith, J. C. Green, C. Froning, S. V. Penton and S. N. Osterman, "An HST/COS Survey of the Low-redshift Intergalactic Medium. I. Survey, Methodology, and Overall Results", ApJ **817**, 2, 111 (2016).

Davé, R., K. Finlator and B. D. Oppenheimer, "Galaxy evolution in cosmological simulations with outflows - II. Metallicities and gas fractions", MNRAS **416**, 1354–1376 (2011).

Dekel, A. and J. Silk, "The origin of dwarf galaxies, cold dark matter, and biased galaxy formation", ApJ **303**, 39–55 (1986).

Dubey, A., L. B. Reid and R. Fisher, "Introduction to FLASH 3.0, with application to supersonic turbulence", Physica Scripta Volume T **132**, 014046 (2008).

Dursi, L. J. and C. Pfrommer, "Draping of Cluster Magnetic Fields over Bullets and Bubbles—Morphology and Dynamic Effects", ApJ **677**, 2, 993–1018 (2008).

Ferland, G. J., M. Chatzikos, F. Guzmán, M. L. Lykins, P. A. M. van Hoof, R. J. R. Williams, N. P. Abel, N. R. Badnell, F. P. Keenan, R. L. Porter and P. C. Stancil, "The 2017 Release Cloudy", RMxAA**53**, 385–438 (2017).

Ferland, G. J., R. L. Porter, P. A. M. van Hoof, R. J. R. Williams, N. P. Abel, M. L. Lykins, G. Shaw, W. J. Henney and P. C. Stancil, "The 2013 Release of Cloudy", RMxAA**49**, 137–163 (2013).

Ford, A. B., B. D. Oppenheimer, R. Davé, N. Katz, J. A. Kollmeier and D. H. Weinberg, "Hydrogen and metal line absorption around low-redshift galaxies in cosmological hydrodynamic simulations", MNRAS **432**, 89–112 (2013).

Foreman-Mackey, D., D. W. Hogg, D. Lang and J. Goodman, "emcee: The MCMC Hammer", PASP**125**, 306 (2013).

Fragile, P. C., P. Anninos, K. Gustafson and S. D. Murray, "Magnetohydrodynamic Simulations of Shock Interactions with Radiative Clouds", ApJ **619**, 327–339 (2005).

Fragile, P. C., S. D. Murray, P. Anninos and W. van Breugel, "Radiative Shock-induced Collapse of Intergalactic Clouds", ApJ **604**, 1, 74–87 (2004).

Fryxell, B., K. Olson, P. Ricker, F. X. Timmes, M. Zingale, D. Q. Lamb, P. MacNeice, R. Rosner, J. W. Truran and H. Tufo, "FLASH: An Adaptive Mesh Hydrodynamics Code for Modeling Astrophysical Thermonuclear Flashes", ApJS **131**, 273–334 (2000).

Fujita, A. and M.-M. Mac Low, "Cosmic Ray Driven Outflows in an Ultraluminous Galaxy", MNRAS (2018).

Genel, S., M. Vogelsberger, V. Springel, D. Sijacki, D. Nelson, G. Snyder, V. Rodriguez-Gomez, P. Torrey and L. Hernquist, "Introducing the Illustris project: the evolution of galaxy populations across cosmic time", MNRAS **445**, 1, 175–200 (2014).

Gnat, O. and G. J. Ferland, "Ion-by-ion Cooling Efficiencies", ApJS **199**, 1, 20 (2012).

Grassi, T., S. Bovino, D. R. G. Schleicher, J. Prieto, D. Seifried, E. Simoncini and F. A. Gianturco, "KROME - a package to embed chemistry in astrophysical simulations", MNRAS **439**, 2386–2419 (2014).

Gray, W. J., P. A. Keiter, H. Lefevre, C. R. Patterson, J. S. Davis, K. G. Powell, C. C. Kuranz and R. P. Drake, "Atomic modeling of photoionization fronts in nitrogen gas", Physics of Plasmas **26**, 5, 052901 (2019).

Gray, W. J. and E. Scannapieco, "Formation of Compact Stellar Clusters by High-Redshift Galaxy Outflows. I. Non-Equilibrium Coolant Formation", ApJ **718**, 417–432 (2010).

Gray, W. J. and E. Scannapieco, "Atomic Chemistry in Turbulent Astrophysical Media. II. Effect of the Redshift Zero Metagalactic Background", ApJ **818**, 198 (2016).

Gray, W. J. and E. Scannapieco, "The Effect of Turbulence on Nebular Emission Line Ratios", ApJ **849**, 132 (2017).

Gray, W. J., E. Scannapieco and D. Kasen, "Atomic Chemistry in Turbulent Astrophysical Media. I. Effect of Atomic Cooling", ApJ **801**, 107 (2015).

Gregori, G., F. Miniati, D. Ryu and T. W. Jones, "Enhanced Cloud Disruption by Magnetic Field Interaction", ApJ **527**, 2, L113–L116 (1999).

Gregori, G., F. Miniati, D. Ryu and T. W. Jones, "Three-dimensional Magnetohydrodynamic Numerical Simulations of Cloud-Wind Interactions", ApJ **543**, 775–786 (2000).

Griffiths, R. E., A. Ptak, E. D. Feigelson, G. Garmire, L. Townsley, W. N. Brandt, R. Sambruna and J. N. Bregman, "Hot Plasma and Black Hole Binaries in Starburst Galaxy M82", Science **290**, 5495, 1325–1328 (2000).

Gronke, M. and S. P. Oh, "The growth and entrainment of cold gas in a hot wind", MNRAS **480**, 1, L111–L115 (2018).

Gronke, M. and S. P. Oh, "How cold gas continuously entrains mass and momentum from a hot wind", arXiv e-prints p. arXiv:1907.04771 (2019).

Grønnow, A., T. Tepper-García and J. Bland-Hawthorn, "Magnetic Fields in the Galactic Halo Restrict Fountain-driven Recycling and Accretion", ApJ **865**, 64 (2018).

Grønnow, A., T. Tepper-García, J. Bland-Hawthorn and N. M. McClure-Griffiths, "Magnetized High Velocity Clouds in the Galactic Halo: A New Distance Constraint", ApJ **845**, 69 (2017).

Haardt, F. and P. Madau, "Radiative Transfer in a Clumpy Universe. II. The Ultraviolet Extragalactic Background", ApJ **461**, 20 (1996).

Haardt, T. and P. Madau, "Radiative Transfer in a Clumpy Universe. IV. New Synthesis Models of the Cosmic UV/X-Ray Background", ApJ **746**, 125 (2012).

Heckman, T., S. Borthakur, V. Wild, D. Schiminovich and R. Bordoloi, "COS-burst: Observations of the Impact of Starburst-driven Winds on the Properties of the Circum-galactic Medium", ApJ **846**, 2, 151 (2017a).

Heckman, T., S. Borthakur, V. Wild, D. Schiminovich and R. Bordoloi, "COS-burst: Observations of the Impact of Starburst-driven Winds on the Properties of the Circum-galactic Medium", ApJ **846**, 151 (2017b).

Heckman, T. M., "Starbursts in the Far-Ultraviolet", arXiv e-prints pp. astro–ph/0410383 (2004).

Heckman, T. M., L. Armus and G. K. Miley, "On the nature and implications of starburst-driven galactic superwinds", ApJS **74**, 833–868 (1990).

Heckman, T. M., M. D. Lehnert and L. Armus, *Galactic Superwinds*, vol. 188, p. 455 (1993).

Hopkins, P. F., D. Kereš, J. Oñorbe, C.-A. Faucher-Giguère, E. Quataert, N. Murray and J. S. Bullock, "Galaxies on FIRE (Feedback In Realistic Environments): stellar feedback explains cosmologically inefficient star formation", MNRAS **445**, 1, 581–603 (2014).

Hopkins, P. F., E. Quataert and N. Murray, "Stellar feedback in galaxies and the origin of galaxy-scale winds", MNRAS **421**, 3522–3537 (2012).

Hummels, C. B., B. D. Smith and D. W. Silvia, "Trident: A Universal Tool for Generating Synthetic Absorption Spectra from Astrophysical Simulations", ApJ **847**, 59 (2017).

Johansson, E. P. G. and U. Ziegler, "Radiative Interaction of Shocks with Small Interstellar Clouds as a Pre-stage to Star Formation", ApJ **766**, 1, 45 (2013).

Jones, T. W., D. Ryu and I. L. Tregillis, "The Magnetohydrodynamics of Supersonic Gas Clouds: MHD Cosmic Bullets and Wind-swept Clumps", ApJ **473**, 365 (1996).

Kacprzak, G. G., C. L. Martin, N. Bouché, C. W. Churchill, J. Cooke, A. LeReun, I. Schroetter, S. H. Ho and E. Klimek, "New Perspective on Galaxy Outflows from the First Detection of Both Intrinsic and Traverse Metal-line Absorption", ApJ **792**, L12 (2014).

Kaviraj, S., C. Laigle, T. Kimm, J. E. G. Devriendt, Y. Dubois, C. Pichon, A. Slyz, E. Chisari and S. Peirani, "The Horizon-AGN simulation: evolution of galaxy properties over cosmic time", MNRAS **467**, 4739–4752 (2017).

Keeney, B. A., J. T. Stocke, J. L. Rosenberg, C. W. Danforth, E. V. Ryan-Weber, J. M. Shull, B. D. Savage and J. C. Green, "HST/COS Spectra of Three QSOs That Probe the Circumgalactic Medium of a Single Spiral Galaxy: Evidence for Gas Recycling and Outflow", ApJ **765**, 27 (2013).

Klein, R. I., C. F. McKee and P. Colella, "On the hydrodynamic interaction of shock waves with interstellar clouds. 1: Nonradiative shocks in small clouds", ApJ **420**, 213–236 (1994).

Kwak, K., D. B. Henley and R. L. Shelton, "Simulations of High-velocity Clouds. I. Hydrodynamics and High-velocity High Ions", ApJ **739**, 30 (2011).

Larson, R. B., "Effects of supernovae on the early evolution of galaxies", MNRAS **169**, 229–246 (1974).

Leitherer, C., D. Schaerer, J. D. Goldader, R. M. G. Delgado, C. Robert, D. F. Kune, D. F. de Mello, D. Devost and T. M. Heckman, "Starburst99: Synthesis Models for Galaxies with Active Star Formation", ApJS **123**, 3–40 (1999).

Li, S., A. Frank and E. G. Blackman, "Magnetohydrodynamic Shock-Clump Evolution with Self-contained Magnetic Fields", ApJ **774**, 2, 133 (2013).

Li, Z., P. F. Hopkins, J. Squire and C. Hummels, "On the survival of cool clouds in the circumgalactic medium", MNRAS **492**, 2, 1841–1854 (2020).

Lopez, L. A., S. Mathur, D. D. Nguyen, T. A. Thompson and G. M. Olivier, "Temperature and Metallicity Gradients in the Hot Gas Outflows of M82", ApJ **904**, 2, 152 (2020).

Lu, Y., G. A. Blanc and A. Benson, "An Analytical Model for Galaxy Metallicity: What do Metallicity Relations Tell Us about Star Formation and Outflow?", ApJ **808**, 129 (2015).

Lynds, C. R. and A. R. Sandage, "Evidence for an Explosion in the Center of the Galaxy M82.", AJ**68**, 284 (1963).

Mac Low, M.-M. and A. Ferrara, "Starburst-driven Mass Loss from Dwarf Galaxies: Efficiency and Metal Ejection", ApJ **513**, 1, 142–155 (1999).

Mac Low, M.-M., C. F. McKee, R. I. Klein, J. M. Stone and M. L. Norman, "Shock interactions with magnetized interstellar clouds. 1: Steady shocks hitting nonradiative clouds", ApJ **433**, 757–777 (1994).

Marder, B., "A method for incorporating gauss' law into electromagnetic pic codes", Journal of Computational Physics **68**, 1, 48 – 55, URL `http://www.sciencedirect.com/science/article/pii/002199918790043X` (1987).

Martin, C. L., "Properties of Galactic Outflows: Measurements of the Feedback from Star Formation", ApJ **513**, 156–160 (1999).

Martin, C. L., "Mapping Large-Scale Gaseous Outflows in Ultraluminous Galaxies with Keck II ESI Spectra: Variations in Outflow Velocity with Galactic Mass", ApJ **621**, 227–245 (2005).

McCarthy, P. J., W. van Breugel and T. Heckman, "Evidence for large-scale winds from starburst galaxies. I - The nature of the ionized gas in M82 and NGC 253", AJ**93**, 264–275 (1987).

McClure-Griffiths, N. M., J. A. Green, A. S. Hill, F. J. Lockman, J. M. Dickey, B. M. Gaensler and A. J. Green, "Atomic Hydrogen in a Galactic Center Outflow", ApJ **770**, 1, L4 (2013).

McCourt, M., S. P. Oh, R. O'Leary and A.-M. Madigan, "A characteristic scale for cold gas", MNRAS **473**, 4, 5407–5431 (2018).

McCourt, M., R. M. O'Leary, A.-M. Madigan and E. Quataert, "Magnetized gas clouds can survive acceleration by a hot wind", MNRAS **449**, 2–7 (2015).

McKeith, C. D., A. Greve, D. Downes and F. Prada, "The outflow in the halo of M 82.", A&A **293**, 703–709 (1995).

Meiring, J. D., T. M. Tripp, J. K. Werk, J. C. Howk, E. B. Jenkins, J. X. Prochaska, N. Lehner and K. R. Sembach, "QSO Absorption Systems Detected in Ne VIII: High-metallicity Clouds with a Large Effective Cross Section", ApJ **767**, 49 (2013).

Mellema, G., J. D. Kurk and H. J. A. Röttgering, "Evolution of clouds in radio galaxy cocoons", A&A **395**, L13–L16 (2002).

Miniati, F., D. Ryu, A. Ferrara and T. W. Jones, "Magnetohydrodynamics of Cloud Collisions in a Multiphase Interstellar Medium", ApJ **510**, 726–746 (1999).

Mori, M., A. Ferrara and P. Madau, "Early Metal Enrichment by Pregalactic Outflows. II. Three-dimensional Simulations of Blow-Away", ApJ **571**, 40–55 (2002).

Muratov, A. L., D. Kereš, C.-A. Faucher-Giguère, P. F. Hopkins, E. Quataert and N. Murray, "Gusty, gaseous flows of FIRE: galactic winds in cosmological simulations with explicit stellar feedback", MNRAS **454**, 2691–2713 (2015).

Murray, N., B. Ménard and T. A. Thompson, "Radiation Pressure from Massive Star Clusters as a Launching Mechanism for Super-galactic Winds", ApJ **735**, 66 (2011).

Murray, N., E. Quataert and T. A. Thompson, "On the Maximum Luminosity of Galaxies and Their Central Black Holes: Feedback from Momentum-driven Winds", ApJ **618**, 2, 569–585 (2005).

Muzahid, S., G. G. Kacprzak, C. W. Churchill, J. C. Charlton, N. M. Nielsen, N. L. Mathes and S. Trujillo-Gomez, "An Extreme Metallicity, Large-scale Outflow from a Star-forming Galaxy at z ~0.4", ApJ **811**, 2, 132 (2015).

Ng, M., N. M. Nielsen, G. G. Kacprzak, S. K. Pointon, S. Muzahid, C. W. Churchill and J. C. Charlton, "Kinematics of the O VI Circumgalactic Medium: Halo Mass Dependence and Outflow Signatures", ApJ **886**, 1, 66 (2019).

Oppenheimer, B. D. and R. Davé, "Cosmological simulations of intergalactic medium enrichment from galactic outflows", MNRAS **373**, 1265–1292 (2006).

Oppenheimer, B. D., R. Davé and K. Finlator, "Tracing the re-ionization-epoch intergalactic medium with metal absorption lines", MNRAS **396**, 729–758 (2009).

Oppenheimer, B. D., R. Davé, D. Kereš, M. Fardal, N. Katz, J. A. Kollmeier and D. H. Weinberg, "Feedback and recycled wind accretion: assembling the z = 0 galaxy mass function", MNRAS **406**, 2325–2338 (2010).

Oppenheimer, B. D., J. Schaye, R. A. Crain, J. K. Werk and A. J. Richings, "The multiphase circumgalactic medium traced by low metal ions in EAGLE zoom simulations", MNRAS **481**, 1, 835–859 (2018).

Orlando, S., F. Bocchino, F. Reale, G. Peres and P. Pagano, "The Importance of Magnetic-Field-Oriented Thermal Conduction in the Interaction of SNR Shocks with Interstellar Clouds", ApJ **678**, 274–286 (2008).

Orlando, S., G. Peres, F. Reale, F. Bocchino, R. Rosner, T. Plewa and A. Siegel, "Crushing of interstellar gas clouds in supernova remnants. I. The role of thermal conduction and radiative losses", A&A **444**, 505–519 (2005).

Pallottini, A., A. Ferrara, S. Bovino, L. Vallini, S. Gallerani, R. Maiolino and S. Salvadori, "The impact of chemistry on the structure of high-z galaxies", MNRAS **471**, 4128–4143 (2017).

Pittard, J. M., S. A. E. G. Falle, T. W. Hartquist and J. E. Dyson, "The turbulent destruction of clouds - I. A k-ϵ treatment of turbulence in 2D models of adiabatic shock-cloud interactions", MNRAS **394**, 1351–1378 (2009).

Pittard, J. M., T. W. Hartquist and S. A. E. G. Falle, "The turbulent destruction of clouds - II. Mach number dependence, mass-loss rates and tail formation", MNRAS **405**, 2, 821–838 (2010).

Pittard, J. M. and E. R. Parkin, "The turbulent destruction of clouds - III. Three-dimensional adiabatic shock-cloud simulations", MNRAS **457**, 4, 4470–4498 (2016).

Poludnenko, A. Y., A. Frank and E. G. Blackman, "Hydrodynamic Interaction of Strong Shocks with Inhomogeneous Media. I. Adiabatic Case", ApJ **576**, 832–848 (2002).

Rubin, K. H. R., J. X. Prochaska, D. C. Koo, A. C. Phillips, C. L. Martin and L. O. Winstrom, "Evidence for Ubiquitous Collimated Galactic-scale Outflows along the Star-forming Sequence at z ˜ 0.5", ApJ **794**, 156 (2014).

Ruszkowski, M., H.-Y. K. Yang and E. Zweibel, "Global Simulations of Galactic Winds Including Cosmic-ray Streaming", ApJ **834**, 208 (2017).

Samui, S., K. Subramanian and R. Srianand, "Efficient cold outflows driven by cosmic rays in high-redshift galaxies and their global effects on the IGM", MNRAS **476**, 1680–1695 (2018).

Scannapieco, E., "The Production of Cold Gas Within Galaxy Outflows", ApJ **837**, 1, 28 (2017).

Scannapieco, E. and T. Broadhurst, "The Role of Heating and Enrichment in Galaxy Formation", ApJ **549**, 1, 28–45 (2001a).

Scannapieco, E. and T. Broadhurst, "The Role of Heating and Enrichment in Galaxy Formation", ApJ **549**, 28–45 (2001b).

Scannapieco, E. and M. Brüggen, "Simulating supersonic turbulence in galaxy outflows", MNRAS **405**, 3, 1634–1653 (2010).

Scannapieco, E. and M. Brüggen, "The Launching of Cold Clouds by Galaxy Outflows. I. Hydrodynamic Interactions with Radiative Cooling", ApJ **805**, 158 (2015).

Scannapieco, E., A. Ferrara and P. Madau, "Early Enrichment of the Intergalactic Medium and Its Feedback on Galaxy Formation", ApJ **574**, 590–598 (2002).

Scannapieco, E. and S. P. Oh, "Quasar Feedback: The Missing Link in Structure Formation", ApJ **608**, 62–79 (2004).

Scannapieco, E., R. J. Thacker and M. Davis, "High-Redshift Galaxy Outflows and the Formation of Dwarf Galaxies", ApJ **557**, 605–615 (2001).

Schaye, J., R. A. Crain, R. G. Bower, M. Furlong, M. Schaller, T. Theuns, C. Dalla Vecchia, C. S. Frenk, I. G. McCarthy, J. C. Helly, A. Jenkins, Y. M. Rosas-Guevara, S. D. M. White, M. Baes, C. M. Booth, P. Camps, J. F. Navarro, Y. Qu, A. Rahmati, T. Sawala, P. A. Thomas and J. Trayford, "The EAGLE project: simulating the evolution and assembly of galaxies and their environments", MNRAS **446**, 521–554 (2015).

Schiano, A. V. R., W. A. Christiansen and J. M. Knerr, "Interstellar clouds in high-speed, supersonic flows: Two-dimensional simulations", ApJ **439**, 237–255 (1995).

Schneider, E. E. and B. E. Robertson, "Hydrodynamical Coupling of Mass and Momentum in Multiphase Galactic Winds", ApJ **834**, 144 (2017).

Schneider, E. E., B. E. Robertson and T. A. Thompson, "Production of Cool Gas in Thermally-Driven Outflows", ArXiv e-prints (2018).

Shapley, A. E., C. C. Steidel, M. Pettini and K. L. Adelberger, "Rest-Frame Ultraviolet Spectra of z˜3 Lyman Break Galaxies", ApJ **588**, 65–89 (2003).

Shin, M.-S., J. M. Stone and G. F. Snyder, "The Magnetohydrodynamics of Shock-Cloud Interaction in Three Dimensions", ApJ **680**, 336–348 (2008).

Sijacki, D., V. Springel, T. Di Matteo and L. Hernquist, "A unified model for AGN feedback in cosmological simulations of structure formation", MNRAS **380**, 877–900 (2007).

Simcoe, R. A., W. L. W. Sargent and M. Rauch, "The Distribution of Metallicity in the Intergalactic Medium at z˜2.5: O VI and C IV Absorption in the Spectra of Seven QSOs", ApJ **606**, 1, 92–115 (2004).

Simpson, C. M., R. Pakmor, F. Marinacci, C. Pfrommer, V. Springel, S. C. O. Glover, P. C. Clark and R. J. Smith, "The Role of Cosmic-Ray Pressure in Accelerating Galactic Outflows", ApJ **827**, L29 (2016).

Smith, B., S. Sigurdsson and T. Abel, "Metal cooling in simulations of cosmic structure formation", MNRAS **385**, 1443–1454 (2008).

Smith, B. D., G. L. Bryan, S. C. O. Glover, N. J. Goldbaum, M. J. Turk, J. Regan, J. H. Wise, H.-Y. Schive, T. Abel, A. Emerick, B. W. O'Shea, P. Anninos, C. B. Hummels and S. Khochfar, "GRACKLE: a chemistry and cooling library for astrophysics", MNRAS **466**, 2217–2234 (2017).

Somerville, R. S. and J. R. Primack, "Semi-analytic modelling of galaxy formation: the local Universe", MNRAS **310**, 4, 1087–1110 (1999).

Sparre, M., C. Pfrommer and M. Vogelsberger, "The physics of multiphase gas flows: fragmentation of a radiatively cooling gas cloud in a hot wind", MNRAS **482**, 4, 5401–5421 (2019).

Springel, V. and L. Hernquist, "Cosmological smoothed particle hydrodynamics simulations: a hybrid multiphase model for star formation", MNRAS **339**, 289–311 (2003).

Strickland, D. K. and T. M. Heckman, "Iron Line and Diffuse Hard X-Ray Emission from the Starburst Galaxy M82", ApJ **658**, 1, 258–281 (2007).

Sturm, E., E. González-Alfonso, S. Veilleux, J. Fischer, J. Graciá-Carpio, S. Hailey-Dunsheath, A. Contursi, A. Poglitsch, A. Sternberg, R. Davies, R. Genzel, D. Lutz, L. Tacconi, A. Verma, R. Maiolino and J. A. de Jong, "Massive Molecular Outflows and Negative Feedback in ULIRGs Observed by Herschel-PACS", ApJ **733**, L16 (2011).

Sur, S., E. Scannapieco and E. C. Ostriker, "Galaxy Outflows Without Supernovae", ApJ **818**, 1, 28 (2016).

Thompson, T. A., E. Quataert, D. Zhang and D. H. Weinberg, "An origin for multiphase gas in galactic winds and haloes", MNRAS **455**, 1830–1844 (2016).

Tremonti, C. A., T. M. Heckman, G. Kauffmann, J. Brinchmann, S. Charlot, S. D. M. White, M. Seibert, E. W. Peng, D. J. Schlegel, A. Uomoto, M. Fukugita and J. Brinkmann, "The Origin of the Mass-Metallicity Relation: Insights from 53,000 Star-forming Galaxies in the Sloan Digital Sky Survey", ApJ **613**, 898–913 (2004).

Tumlinson, J., M. S. Peeples and J. K. Werk, "The Circumgalactic Medium", ARA&A **55**, 1, 389–432 (2017).

Turk, M. J., B. D. Smith, J. S. Oishi, S. Skory, S. W. Skillman, T. Abel and M. L. Norman, "yt: A Multi-code Analysis Toolkit for Astrophysical Simulation Data", ApJS **192**, 9 (2011).

Turner, M. L., J. Schaye, R. A. Crain, T. Theuns and M. Wendt, "Observations of metals in the z $\sim$ 3.5 intergalactic medium and comparison to the EAGLE simulations", MNRAS **462**, 2440–2464 (2016).

van Loo, S., S. A. E. G. Falle, T. W. Hartquist and T. J. T. Moore, "Shock-triggered formation of magnetically-dominated clouds", A&A **471**, 213–218 (2007).

Veilleux, S., G. Cecil and J. Bland-Hawthorn, "Galactic Winds", ARA&A **43**, 769–826 (2005).

Verner, D. A., D. G. Yakovlev, I. M. Band and M. B. Trzhaskovskaya, "Comment on a paper by M. A. Bautista "Atomic data from the Iron Project. XVI. Photoionization cross sections and oscillator strengths for Fe V"", arXiv e-prints pp. astro–ph/9610244 (1996).

Voronov, G. S., "A Practical Fit Formula for Ionization Rate Coefficients of Atoms and Ions by Electron Impact: Z = 1-28", Atomic Data and Nuclear Data Tables **65**, 1 (1997).

Waagan, K., C. Federrath and C. Klingenberg, "A robust numerical scheme for highly compressible magnetohydrodynamics: Nonlinear stability, implementation and tests", Journal of Computational Physics **230**, 3331–3351 (2011).

Werk, J. K., J. X. Prochaska, S. Cantalupo, A. J. Fox, B. Oppenheimer, J. Tumlinson, T. M. Tripp, N. Lehner and M. McQuinn, "The COS-Halos Survey: Origins of the Highly Ionized Circumgalactic Medium of Star-Forming Galaxies", ApJ **833**, 54 (2016).

Werk, J. K., J. X. Prochaska, C. Thom, J. Tumlinson, T. M. Tripp, J. M. O'Meara and M. S. Peeples, "The COS-Halos Survey: An Empirical Description of Metal-line Absorption in the Low-redshift Circumgalactic Medium", ApJS **204**, 2, 17 (2013).

Werk, J. K., J. X. Prochaska, J. Tumlinson, M. S. Peeples, T. M. Tripp, A. J. Fox, N. Lehner, C. Thom, J. M. O'Meara, A. B. Ford, R. Bordoloi, N. Katz, N. Tejos, B. D. Oppenheimer, R. Davé and D. H. Weinberg, "The COS-Halos Survey: Physical Conditions and Baryonic Mass in the Low-redshift Circumgalactic Medium", ApJ **792**, 8 (2014).

Wiersma, R. P. C., J. Schaye and B. D. Smith, "The effect of photoionization on the cooling rates of enriched, astrophysical plasmas", MNRAS **393**, 99–107 (2009).

Wijers, N. A., J. Schaye and B. D. Oppenheimer, "The warm-hot circumgalactic medium around EAGLE-simulation galaxies and its detection prospects with X-ray and UV line absorption", MNRAS **498**, 1, 574–598 (2020).

Wilde, M., J. Werk and J. X. Prochaska, "CGM2: COS+Gemini Mapping of the Circumgalatcic Medium", in "American Astronomical Society Meeting Abstracts #233", vol. 233 of *American Astronomical Society Meeting Abstracts*, p. 355.14 (2019).

Wiseman, P., D. A. Perley, P. Schady, J. X. Prochaska, A. de Ugarte Postigo, T. Krühler, R. M. Yates and J. Greiner, "Gas inflow and outflow in an interacting high-redshift galaxy. The remarkable host environment of GRB 080810 at z = 3.35", A&A **607**, A107 (2017).

Xu, J. and J. M. Stone, "The Hydrodynamics of Shock-Cloud Interactions in Three Dimensions", ApJ **454**, 172 (1995).